3D cine DENSE MRI: Ventricular segmentation and myocardial strain analysis

Daniel A. Auger

Department of Human Biology

University of Cape Town

Thesis presented for the degree of

Doctor of Philosophy

February 2013

Declaration

I, Daniel Alejandro Auger, hereby declare that the above thesis is my own unaided work both in concept and execution, and that apart from the normal guidance from my supervisor, I have received no assistance.

The thesis has been presented by me for examination for the degree of Doctor of Philosophy in Medicine in Biomedical Engineering.

_____

Signature

_____

Date

Abstract

3D cine DENSE MRI: Ventricular segmentation and myocardial strain analysis

Daniel Alejandro Auger 11 February 2013

Displacement encoding with stimulated echoes (DENSE) is a quantitative magnetic resonance imaging (MRI) technique which measures myocardial displacement at a pixel resolution. Regional myocardial strain can then be calculated, providing a useful clinical measure of myocardial function. Right ventricular (RV) function is difficult to quantify because of its asymmetrical geometry, thin myocardial wall and eccentric motion. Novel motion and strain analysis techniques using 3D cine DENSE are presented for the RV. Three dimensional tissue tracking methods offer the ability to quantify RV strain at a previously unattainable spatial resolution. The RV is divided into four anatomical segments in order to provide regional measures of strain across the cardiac cycle. Results compare favorably to previous studies, showing variation in strain according to structure. Segmenting the myocardium from 3D cine DENSE data is necessary for regional myocardial strain quantification. This prohibitively time consuming step is a limiting factor for the use of 3D cine DENSE in a clinical environment. A semi-automated left ventricular segmentation algorithm is introduced to minimize the data analysis time. The segmentation is initialized by interactively placing guide points along the left ventricles borders at a single cardiac phase. A mathematical model is fitted to the points and used to generate epicardial and endocardial surfaces. Each surface is then propagated across the cardiac cycle using the displacement information inherent in the phase data. Segmentation results compare well to corresponding manually defined contours, and the time required to segment an entire three dimensional data set is reduced by 10 fold, with only 5.6% of contours requiring readjustment. Finally, methods are presented to quantify bi-ventricular cardiac dyssynchrony using strain measurements obtained from multiple planes of 2D cine DENSE data. Results illustrate the variation of regional strain across the cardiac cycle between healthy and diseased hearts. Dyssynchrony is quantified using time to onset and time to peak strain metrics. Results illustrate bi-ventricular strain variations reflecting right and left bundle branch blocks.

Acknowledgements

This research project would not have been possible without the guidance and support from various individuals. I would like to express my sincere appreciation and gratitude to all of them.

First of all, I would like to thank my supervisor Bruce S. Spottiswoode, for his direction, unlimited support and inspiration through the course of this project. I could not have accomplished this work without his expert advice and contributions. I have learnt and benefited from his expertise in MRI, attitude towards scientific research and his incredible work passion.

I am most grateful to my co-supervisor Ernesta M. Meintjes for her willingness to take on my project for the final year of my research. Her guidance, expertise and contribution were invaluable.

My deepest gratitude goes to Dr Frederick H. Epstein for welcoming me into his research group during my visit to the University of Virginia. His support, encouragement and expert advice in cardiac MRI were invaluable.

Many thanks to Dr Xiaodong Zhong, for his contribution to this work, for his patience, and his eagerness to provide his expert advice and vast knowledge in cine DENSE analysis.

I would like to further thank Dr Christopher Ball for his valuable collaboration with the long axis DENSE analysis tool and his constant support and availability.

My appreciation to Dr Aaron Hess for his assistance and valuable discussions in strain theory; to Dr Drew Gilliam for his helpful discussions and suggestions with the left ventricular segmentation algorithm and to Dr Kenneth C. Bilchick for his clinical expertise and his support in acquiring patient data for this project.

I would like to thank my colleagues and friends Dr Ian Burger, Jia Fan and Muhammad Saleh for the useful and motivating discussions on research related and MRI topics.

My utmost recognition and gratitude to the University of Cape Town, principally to the Department of Human Biology for providing a motivating academic environment, and to the Division for Postgraduate Funding for the financial assistance during the length of my research through a research associate merit award and for providing financial aid to enable the visit to the University of Virginia (USA).

Funding was provided by the South African Research Chairs Initiative of the Department of Science and Technology and National Research Foundation of South Africa, NIH grants FA2005040800023, NIH/FIC and NIBIB R03 TW007633.

Finally, I would like to thank my family for their love and support. I could not have done this without them. I owe everything I have accomplished to my parents, and I appreciate everything they have done for me. I would like to dedicate this thesis to them.

Table of Contents

List of Tables

List of Figures

Preface

This dissertation presents and evaluates novel methods and techniques for the three dimensional (3D) analysis of myocardial function and strain in healthy and diseased hearts, using displacement encoding with stimulated echoes (DENSE) magnetic resonance imaging (MRI). The rationale for this work is to contribute towards the field of cardiac MR research by using a recently developed cardiac MRI technique to better quantify and understand the motion and function of the human heart in three dimensions.

This dissertation includes three independent articles which are found in chapters three, four and five. Each chapter includes an introduction that provides the necessary background and context of the work presented in that chapter. Each chapter further documents and evaluates aspects of the methodology, results and conclusions pertaining to that chapter. This allows for the direct access and evaluation of the different methodologies and follows a logical progression of the work. Due to this format of the thesis, the document necessarily contains repetition as each of the core chapters is presented as an independent article. The contributions of co-authors to each chapter are given below for examination purposes.

Chapter 1 provides a brief introduction of the purpose and scope of this dissertation.

Chapter 2 provides an overview of cardiac anatomy and physiology, cardiac imaging, basic MRI physics, relevant topics in cardiac MRI, and a comprehensive review of cardiac MR image analysis techniques.

Chapter 3 is journal article that has been peer reviewed and published in the *Journal of Cardiovascular Magnetic Resonance*. This chapter describes the application of 3D DENSE to assess the detailed motion of the entire right ventricle (RV) at a previously unachievable spatial resolution. Novel post processing techniques are introduced for tissue tracking and strain computation, and a method for subdividing the RV for regional strain analysis using clear anatomical landmarks is proposed. Quantitative strain results are presented for five normal volunteers. I was the primary author of this article with insights and assistance from all other co-authors. Xiaodong Zhong and Frederick H. Epstein developed and implemented the 3D spiral cine DENSE sequence and acquired the data. Bruce S. Spottiswoode and

Xiaodong Zhong participated in the development of DENSE post processing software. I implemented all RV-specific post processing techniques. These include 3D tissue tracking, a 3D strain algorithm, RV anatomical divisions, and all strain analyses.

Chapter 4 is a manuscript which has been prepared and submitted for publication to the *Journal of Cardiovascular Magnetic Resonance*. This chapter describes a semi-automated method for segmenting the left ventricle (LV) from its surrounding anatomical structures for volumetric 3D cine DENSE data. The chapter includes the description of the algorithm, which is based on a guide point model approach, noise removal techniques, and a novel method to robustly propagate LV epicardial and endocardial surfaces of the model using the displacement information encoded in the phase images of the DENSE data. I was the primary author of this article with insights and assistance from all other co-authors. Xiaodong Zhong and Frederick H. Epstein developed and implemented the 3D spiral cine DENSE sequence and acquired the data. Bruce S. Spottiswoode and Xiaodong Zhong participated in the development of post processing DENSE software, including the phase unwrapping algorithm. I implemented all segmentation methods which include adapting the LV geometrical model for 3D DENSE MRI data, phase noise removal, LV 3D tissue tracking, and propagation of the LV model across the cardiac cycle while segmenting the LV myocardium.

Chapter 5 presents an application of cine DENSE to evaluate LV and RV strain in patients with cardiac dyssynchrony. Three dimensional cine DENSE is not yet suitable for routine clinical use due to impractical long scan times that are difficult for patients to tolerate. In this chapter, two dimensional (2D) cine DENSE data in two orthogonal views are combined to present reliable methods to quantify bi-ventricular dyssynchrony in the absence of true 3D DENSE clinical data. This material is being worked into a manuscript for future publication.

Chapter 6 presents a comprehensive discussion and summary of the main findings of the work, highlights the strengths and limitations of the methods presented, and discusses possible future work.

Chapter 7 presents the conclusion.

Chapter 1

Introduction

1.1 Rationale and Motivation

Cardiovascular disease (CVD) remains a leading cause of death worldwide, accounting for 33.6% of deaths in the USA in 2007 [1]. The American Heart Association plans to reduce deaths from CVD by 20% and improve the cardiovascular health of all Americans by a further 20%. In order to achieve these goals, the ability to diagnose, treat, manage current patients and individuals with risk factors must be improved. Heart disease can affect any region of the myocardium, and the complex movement and contraction of the heart occurs in a three dimensional (3D) manner. To date, our understanding of cardiac function and pathology is still limited and various techniques have been developed for the effective diagnosis and treatment of CVD's. The ability to non-invasively image myocardial wall motion has significant potential for the diagnosis, treatment and management of heart disease. There have been various techniques developed for cardiac imaging in order to provide qualitative and quantitative information on the morphology and functioning of the heart. Cardiovascular magnetic resonance (CMR) imaging provides a number of advantages over other imaging modalities, such as excellent spatial resolution, superior contrast and image quality, and no exposure to radiation. CMR has therefore been an active platform for the development of several non-invasive techniques designed to understand myocardial structure, function and perfusion.

Myocardial wall motion abnormalities occur in nearly all heart diseases. Wall motion imaging and regional strain are therefore clinical indicators of myocardial function and viability, but inferring these measures from standard morphological MRI videos is limited as the motion of the heart is complex (rotation, twist, and shear) and there are few distinct anatomical features within the myocardium. Several MRI tissue tracking techniques have been developed in order to study the motion of the heart, including myocardial tagging, phase contrast velocity encoding, and displacement

encoding with stimulated echoes (DENSE). Myocardial strain can be quantified using these techniques and in turn be used as an indicator for pathology.

In DENSE, displacement is encoded into the phase of the images so that myocardial motion can be quantified at a high spatial resolution over segments of the cardiac cycle [2, 3]. DENSE is a technique which has the potential to overcome the disadvantages of tagging and velocity encoding while combining and enhancing the advantages of each. However, three dimensional imaging and tissue tracking techniques are required to accurately capture the complex 3D motion of the heart. A 3D spiral cine DENSE sequence has recently been designed and implemented in order to provide 3D volumetric displacement encoded data [4]. This thesis presents novel methods and techniques for the analysis of regional myocardial function in three dimensions using 3D cine DENSE MRI.

Chapter 2

Background

2.1 Physics of MRI

2.1.1 Principles of MRI

The core to understanding the principle of MRI is to understand the concept of magnetic / nuclear spin. Nuclei of atoms consist of particles, namely protons and neutrons, exhibiting independent quantum mechanical behavior. MRI relies on the fact that atoms with an odd number of protons and / or neutrons possess a non-zero nuclear spin angular momentum, **I**. This nuclear spin results in a magnetic dipole moment, **μ**, which is randomly orientated. When these atoms are placed in the presence of an external magnetic field $\mathbf{B_0}$, the interaction is given by the nuclear Zeeman relationship:

$$H = -\boldsymbol{\mu} \cdot \mathbf{B_0} \tag{2.1}$$

where H is the potential energy of the magnetic dipole **μ** in $\mathbf{B_0}$. This torque causes the magnetic dipole moment to precess about the magnetic field $\mathbf{B_0}$ at a resonant frequency ω_L, known as the Larmor precession frequency given by

$$\omega_L = \gamma \mathbf{B_0} \tag{2.2}$$

where γ is the gyromagnetic ratio for a particular nucleus. The magnetic field is typically 1.5T or 3T in medical applications, and applied in the z-direction known as the longitudinal direction. This precession of millions of dipole moments gives rise to a net magnetization vector **M**, which is initially parallel to $\mathbf{B_0}$. In MRI, the most commonly used atom is hydrogen due to its abundance both in the human body and naturally, as well as its excellent MR properties.

Consider a collection of hydrogen atoms in a sample of tissue. Initially the spins / magnetization vectors are all randomly orientated with respect to each other, resulting in a net magnetization equal to zero. In the presence of $\mathbf{B_0}$ the spins align parallel to

the magnetic field, while they precess at the Larmor frequency ω_L, with a net magnetization **M**. An oscillating radiofrequency (rf) electromagnetic field $\mathbf{B_1}$ applied perpendicular to $\mathbf{B_0}$ at the Larmor frequency excites the spins, causing the magnetic field **M** to flip towards the transverse (X-Y) plane. After application of the rf pulse, the magnetization will have both a transverse ($\mathbf{M_{xy}}$) and longitudinal ($\mathbf{M_z}$) magnetization component. The ability of a small rf field applied at the Larmor frequency to flip the magnetization is referred to as the *magnetic resonance phenomenon*. $\mathbf{B_1}$ is defined by

$$\mathbf{B_1}(\mathrm{t}) = \mathbf{B_1}\mathrm{e}^{-\mathrm{i}\omega_0\mathrm{t}} \tag{2.3}$$

The equation of motion for the magnetization is given by

$$\frac{\mathrm{d}\mathbf{M}(\mathrm{t})}{\mathrm{d_t}} = \mathbf{M}(\mathrm{t}) \times \gamma\mathbf{B}(\mathrm{t}), \tag{2.4}$$

which describes precessional motion of the magnetization vector around an effective magnetic field **B**(*t*). Assuming the rf pulse is applied exactly at resonance ($\omega_0=\omega_L$), the effective field is simply $\mathbf{B_1}$, so that the magnetization precesses around $\mathbf{B_1}$ for the duration of the rf pulse at a frequency $\gamma\mathbf{B_1}$. The magnetization rotates through an angle $\boldsymbol{\alpha}$, known as the flip angle, which is determined by the magnitude and duration of the rf pulse, $\alpha=\gamma\mathbf{B_1}\mathrm{t}$. The resultant components of the magnetization vector with initial condition **M** (0) = M_0 are;

$$\mathbf{M_{XY}} = \mathrm{M}_0 \sin(\gamma\mathbf{B_1}\tau)\mathrm{e}^{-\mathrm{i}\omega_0\mathrm{t}} \tag{2.5}$$

$$\mathbf{M_z} = \mathrm{M}_0 \cos(\gamma\mathbf{B_1}\tau)\mathrm{e}^{-\mathrm{i}\omega_0\mathrm{t}} \tag{2.6}$$

where τ is the duration of the rf pulse and t is the time. Once the rf pulse is turned off, the energy is released and the magnetization returns to its state of equilibrium. Precession of the magnetization around the net magnetic field $\mathbf{B_0}$, now induces an emf in a receiving coil according to Faraday's law. This signal is the MR signal. Since the magnetization relaxes back to equilibrium, the signal decays, resulting in what is known as a Free Induction Decay (FID). The Bloch equations describe the motion of the components of the magnetization vector and are given by

$$\frac{dM_x}{dt} = \left(\mathbf{M}(t) \times \gamma \mathbf{B}(t)\right)_x - \frac{M_x(t)}{T_2} \tag{2.7}$$

$$\frac{dM_y}{dt} = \left(\mathbf{M}(t) \times \gamma \mathbf{B}(t)\right)_y - \frac{M_y(t)}{T_2} \tag{2.8}$$

$$\frac{dM_z}{dt} = \left(\mathbf{M}(t) \times \gamma \mathbf{B}(t)\right)_z - \frac{M_z(t) - M_0}{T_1} \tag{2.9}$$

In the above, T_1 is the longitudinal relaxation time constant, which is dependent on the energy exchange between the spin and its lattice, while T_2 is the transverse relaxation time constant, which is dependent on the energy exchange between individual spins.

2.1.2 Image formation

Images are reconstructed from the signal received by the receiver coils. However, as the signal is a function of time, the spatial distribution of magnetization is not possible. Magnetic field gradients are therefore used to spatially encode the signal, using slice selection, frequency encoding and phase encoding gradients.

The slice encoding gradient G_z is applied perpendicular to the imaging plane during the rf pulse. This causes the resonance condition to be satisfied for only a particular band of frequencies, exciting a specific slice of tissue. The width of the slice is dependent on the strength, G_z of the gradient as well as the bandwidth of the rf pulse.

The frequency encoding gradient G_x encodes the frequency in one of the in plane directions, say the x-direction, during signal acquisition, causing the frequency of the signal to vary as a function of position. The phase encoding gradient G_y is applied after the rf pulse, but before signal acquisition. The gradient encodes phase along the y-direction. The gradient creates a linear variation in spin frequency, where the higher spin frequencies acquire more phase, than the lower frequencies during the duration of the pulse. For an image consisting of a matrix size m×n, the phase encoding step is repeated n times in order to uniquely encode the phase pattern of every pixel in the y-direction. The frequency and phase encoded data are decomposed using 2D Fourier

Transform to produce an MR image. The 2D Fourier space is also known as k-space. Each row corresponds to a repetition of the sequence for a different phase encoding gradient. The order in which k-space is filled is directly related to the sequence and this can be varied to optimize acquisition for different applications.

2.2 The Human Heart

The heart is a four chambered muscular pump, the parts of which work in unison to supply blood to the entire body. The right side of the heart receives deoxygenated blood / venous blood through the superior (SVC) and inferior vena cava (IVC), and pumps it through the pulmonary trunk to the lungs for oxygenation. The left side of the heart receives oxygenated / arterial blood from the pulmonary veins, and pumps it to the entire body via the aorta. The heart is surrounded by a fibrous sac which is bound to the central tendon of the diaphragm, the sternum and the posterior mediastinum, keeping the heart relatively tethered in place. Between the fibrous pericardium and the heart exists the pericardial cavity. It contains a thin film of fluid which allows the heart to move in a friction free environment. The muscular wall of the heart itself consists of three layers; the endocardium, myocardium and the epicardium. The endocardium is the endothelial internal membrane which also covers the heart valves. The myocardium is the thick middle layer which is composed of the cardiac muscle, and the epicardium is a thin external layer formed by the visceral layer of the pericardium. The walls of the heart consist mainly of thick myocardium, especially the ventricles.

The heart is situated obliquely in the thoracic cavity, and consists of the apex directed anteriorly and to the left, the base which is directly opposite the apex facing posteriorly, and the diaphragmatic, sternocostal and pulmonary surfaces. An anterior view of the heart in the thoracic cavity is seen in Figure 2.1 [5].

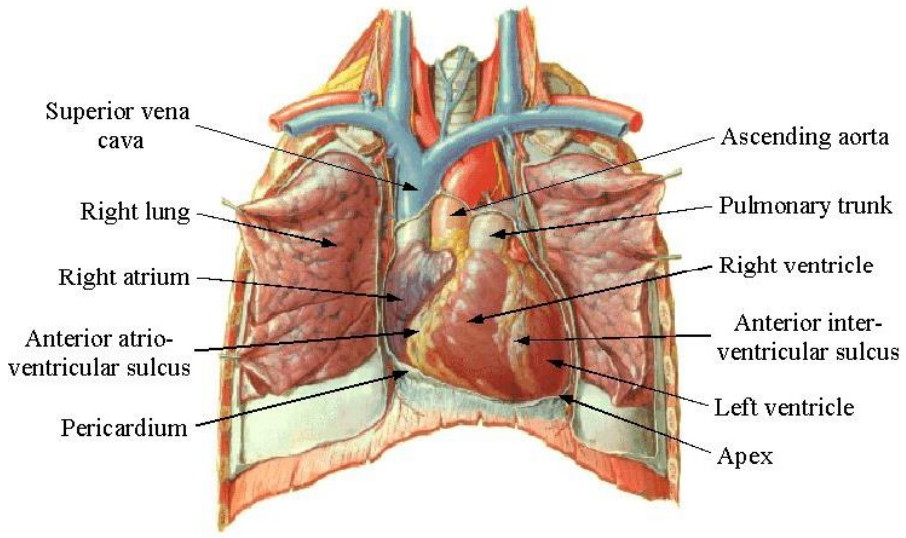

Figure 2.1: Anterior view of the heart in situe. The Pericardium has been removed. Image adapted from Netter (1998).

The heart consists of four chambers, namely, the left and right atriums (RA and LA) and the left and right ventricles (LV and RV). The RA receives venous blood from the SVC and IVC, and pumps it into the RV through the tricuspid valve. The RV then pumps the blood to the lungs. The LA receives the oxygenated blood from the lungs and pumps it to the LV through the bicuspid / mitral valve.

The LV is responsible for supplying the entire body with arterial blood. The LV therefore requires the greater pumping force and as a result consists of the thickest myocardial wall. The RV pumps blood to the lungs at a much shorter distance away. The walls of the RV are therefore much thinner when compared to the LV. The interventricular septum is a thick muscular wall shared by both ventricles. The portion of the ventricles excluding the septum is referred to as the free walls. The functioning of the LV is vital, as it is solely responsible for pumping blood the greatest distance around the body. However, the heart is a single organ with its chambers working in conjunction with each other. The malfunctioning of one chamber, can easily affect another.

The myocardium is mostly made up of contractile muscle cells known as myocytes that are joined end-to-end to form cardiac muscle fibers, each surrounded by its own membrane. Myocytes are joined at each end by specialized cell junctions known as

intercalated disks, providing cell-to-cell cohesion. Along the muscle fibers, the cell membranes of adjacent fibers fuse forming gap junctions. This arrangement allows for the mechanical and electrical coupling of the cells and the production of the hearts contractile force. The myocardium is arranged in a helical micro-structure where myocytes are arranged in bundles of myofibers. The orientations of the fiber angles vary continuously across the wall from approximately -60° to $+60^{\circ}$. From the apex to the base the fibers follow left handed spiral from the epicardium to the midwall, following a planar circular geometry in the midwall, and a right handed spiral from the midwall to the endocardium which are orientated more circumferentially. These layers are therefore spatially orientated in various directions transmurally and in an apical-basal direction [6].

Young et al. showed that fibers are bundled and form layers of 3-4 cells thick known as sheets [7]. Sheet orientations also vary not only transmurally but in an apical-basal direction. The LV is characterized as an orthotropic material with three mutually orthogonal axes oriented along the fibers, transverse to the fibers (within a sheet), and orthogonal to the sheet. The regional variations in fiber arrangements within and between each of the ventricles show a functional variation according to the structure.
The orthotropic properties of the myocardium influence both the spread of electrical activation, re-polarization and contraction. The speed of the waveform will be affected by the direction in which it is traveling, i.e. fastest along the fibers and slowest normal to the sheets.

The ordinary sequence of events in the cardiac cycle allows the chambers of the heart to contract and function as a synchronous pump. Upon electrical stimulation, the cardiac muscle fibers begin to contract. This contraction results in muscle wall shortening parallel to the wall and thickening perpendicular to the wall. The electrical stimulation begins at the sinuatrial node (SA node) otherwise known as the ‘pacemaker’ of the heart. The propagation and coordination of contraction is accomplished by cardiac muscle cells and specialized conducting fibers. The signal is propagated via myogenic conduction to the avtrioventricular node (AV node). The AV node then distributes the signal to the ventricles through the AV bundle. The bundle divides into two branches in the interventricular septum, the right and left

bundles in order to supply the right and left ventricles respectively. The branches split and pass deep into the sub-endocardial branches (Purkinje fibers) to stimulate the walls of the ventricles.

A cardiac cycle is defined as the period of time from the beginning of one heart beat to the next. The cycle is comprised of relaxation (diastole) when the chambers are filled with blood and contraction (systole) where each chamber contracts and expels the blood out. The two atria contract together before the ventricles, and therefore the period of systole is divided into atrial and ventricular systole. As the atria contract, the ventricles are in a state of diastole in order to accumulate blood. As the atria begin to relax and the ventricles begin to contract, the tricuspid and mitral valves close to prevent regurgitation of blood from the ventricles back into the atria. This is known as isometric contraction. The leaflet of each valve is attached to a papillary muscle, which during contraction and relaxation, allows for opening and closing of the valves. These muscles are often seen in an MRI image.

An electrocardiogram (ECG) is a measure of the electrical activity generated by the heart during the cardiac cycle. Figure 2.2 illustrates this concept [8].

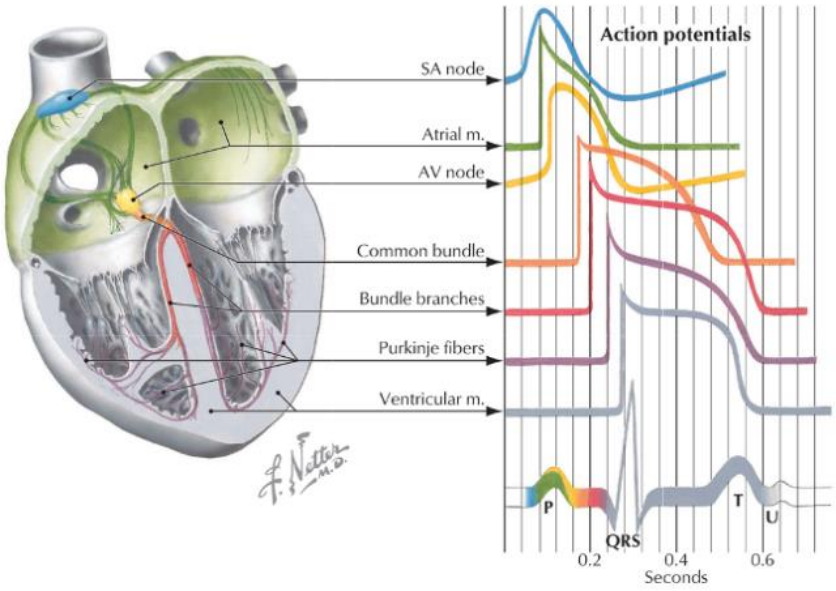

Figure 2.2: ECG diagram depicting the cardiac cycle. Image adapted from Hansen et al. [8].

The ECG is comprised of the P-wave, QRS complex and T-wave. The P-wave is caused by the depolarization of the atria, resulting in atrial contraction. The QRS complex is the most prominent feature in the ECG, which occurs immediately after atrial contraction, and represents ventricular depolarization. The T-wave shows the repolarization of the ventricles and ventricular diastole. As the heart is a moving organ, ECG triggering is often used during structural imaging of the heart. This is known as ECG gating. Imaging is typically performed during diastole when the motion of the heart is less.

(For more detail on the anatomy and physiology of the human heart, please refer to Moore et al. 2006. [9])

2.3 Cardiac Imaging

Echocardiography, X-ray angiography and nuclear cardiology are all examples of cardiac imaging modalities used in the diagnosis and management of CVD's.

X-ray angiography is performed to specifically image the blood vessels of the body, head, the coronary arteries and veins and the blood chambers of the heart. During an angiogram, a catheter is placed into a blood vessel, in either the groin (femoral artery) or the elbow (brachial artery). The catheter is guided to the area of risk or the area to be studied. An iodine dye is administered and its time course recorded by taking a rapid series of X-rays. This provides excellent contrast X-ray images of the area in question, providing both morphological and functional information. An angiogram is typically used to study the narrowing / blockage of a blood vessel, heart chamber size and heart valve function. This is, however, an invasive procedure that cannot be repeated often. The information is only acquired in 2D, and limited information is provided with regards to myocardial motion and contractility.

Due to its widespread availability, echocardiography (echo) is used as the first line imaging modality to evaluate cardiac function. Echo is used to characterize cardiac function such as volume measurements, wall motion and flow, which further allows for the assessment of valve function. Echo uses standard ultrasound techniques to create an image of the moving heart. Ultrasonic waves are transmitted, and when a boundary is encountered (tissue-blood / tissue-tissue interface), some waves are

reflected back, allowing for an image to be created. Echo is inexpensive and widely used; however, image quality is much lower than that of MRI. Ultrasonic waves cannot penetrate through bone and lung tissue effectively, therefore the ultrasonic window is poor in certain cases. Echo data can be used to assess inter-myocardial function, by incorporating speckle tracking. However, this method provides data in the longitudinal orientation of the myocardium, therefore limiting displacement information analysis in CVD's.

Nuclear cardiology / scintigraphy is an excellent tool for myocardial functional analysis. However, the low spatial resolution limits this technique in the morphological analysis of the heart. Nuclear scintigraphy requires the patient to infuse a radio-pharmaceutical which is taken up into the cardiac muscle in proportion to localized blood flow. Gamma rays are emitted from the compound and captured by external detectors. This makes this technique a commonly used method in myocardial perfusion imaging.

Magnetic resonance imaging is well suited for studying cardiac function and cardiac pathologies. Cardiac MRI techniques can assess both global function such as volumes, regional contractile function and a measure of blood flow. Cardiac MRI further has the ability to illustrate tissue perfusion, tissue oxygenation and concentration of metabolites. Furthermore, MRI does not require ionizing radiation, it can provide high quality images of cardiovascular structures without being affected by the bone or air, it can produce high resolution 3D images of both cardiac tissue and blood vessels, and it does not require any invasive procedures. Currently, MRI is the best tool for assessing myocardial viability using late gadolinium-enhanced imaging. Disadvantages of cardiac MRI include longer examination times and the requirement of more patient cooperation.

2.4 Cardiac MRI

Cardiac MRI is generally challenging since MRI is a relatively slow imaging modality and the heart is the organ with the fastest movement in the body. The movements of the lungs and diaphragm during the respiratory cycle further contribute to motion artifacts in the image.

ECG triggering is done almost without exception. As described above, the ECG signal is a periodic trace which describes the electrical potential related to the contraction of the heart. Imaging a moving organ requires that each part of the image be acquired during the same portion of the cardiac cycle (typically during diastole). The ECG signal is commonly triggered at the R wave of the QRS complex. In cardiac MR, image acquisition is a slow process, and sampling is done over a number of heartbeats. This process is illustrated in Figure 2.3.

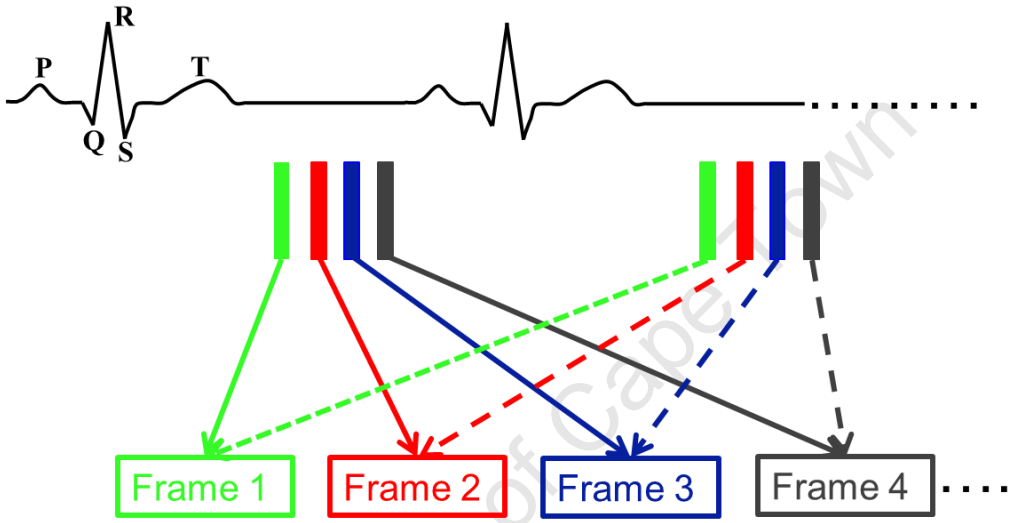

Figure 2.3: ECG triggering in segmented cine cardiac MRI. Multiple samples are taken during consecutive cardiac cycles, each sample contributing to an image of a single frame / slice.

The samples from different phases of the cardiac cycle can be used in a multi-slice collection of images, or combined into a cine image. Cine images are short movies that are able to show the contraction and motion of a single slice of the heart.

Respiratory motion artifacts are alleviated as the patient is often asked to hold his / her breath during each scanning sequence. During 3D imaging, the breath hold time is typically too long and therefore navigator echoes are used. These navigators allow the patient to breathe freely but minimize the effects to motion by monitoring the position of the diaphragm and only acquiring data when the diaphragm is located within a specific predefined window.

In MRI of the body, the imaging planes are orientated orthogonal or parallel to the long axis of the body. Typically, images are acquired in sagittal, coronal and transverse planes. However, due to the position of the heart in the thoracic cavity, such planes are not orthogonal to the walls of the heart, thus preventing accurate anatomic and functional measurements. During cardiac imaging, planes that are orthogonal to the long axis of the heart are therefore used. The standard planes used can be seen in Figure 2.4. These include, short axis, horizontal long axis (four chamber view), and vertical long axis (two chamber view). The planes are defined from a longitudinal line extending from the apex to the center mitral valve of the LV. The short axis plane is defined as perpendicular to the long axis of the heart, while the long axis planes are parallel to longitudinal axis of the heart and aligned either vertically or horizontally.

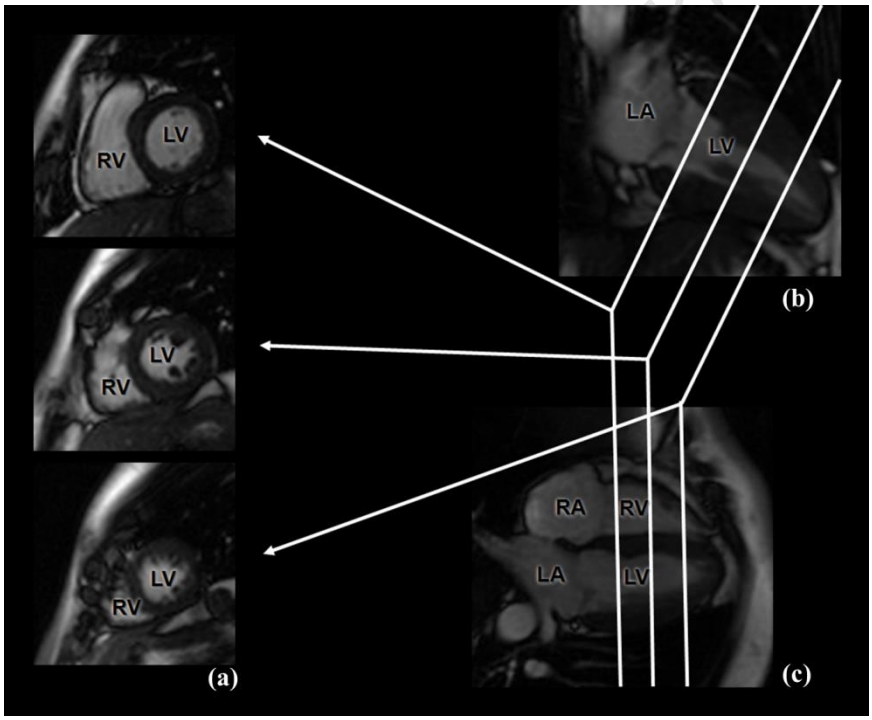

Figure 2.4: Image shows orientation of imaging planes with respect to the heart that are used during cardiac MR image acquisition. (a) Short axis view, (b) vertical long axis view and (c) horizontal long axis view. Image adapted from Bruce S. Spottiswoode, PhD.

2.5 Quantitative Cardiac MR Imaging Techniques

A variety of non-invasive cardiac MRI techniques have been developed to quantitatively evaluate and measure intra-myocardial motion and strain. These include

myocardial tagging, phase contrast velocity encoding (PC) and displacement encoding with stimulated echoes (DENSE).

2.5.1 Myocardial tagging

Myocardial tagging is well established and considered the gold standard in non-invasive cardiac motion and strain analysis. Myocardial tagging involves producing a spatial pattern of saturated magnetization within the myocardium which appears as black lines, otherwise known as tag lines. These tag lines move with the heart as it contracts, thus providing features which may be tracked and used to compute regional measures of myocardial displacement [10, 11]. An example of myocardial tagging MR images are given in Figure 2.5.

Figure 2.5: Myocardial tagging 1D magnitude images showing deformation of tag lines during three stages of the cardiac cycle. (a) End diastole, (b) mid systole and (c) end systole. Image adapted from Moore et al. [12].

The tag lines are applied during end diastole, and are undeformed as per Figure 2.5(a). During systole, the distortion of the tag lines is clear (Figure 2.5(b, c)). As the heart contracts, the blood pool moves out of the imaging plane, therefore, the tag lines do not appear in the blood pool at end systole. The automatic detection of tag lines is difficult due to tags fading during the cardiac cycle and therefore requires extensive user input. However, automated myocardial tag tracking has been achieved with harmonic phase analysis (HARP) [13, 14]. HARP is essentially an image processing technique where one harmonic spectral peak in the k-space of a tagged image is filtered using a k-space bandpass filter. After performing 2D inverse Fourier transform, a complex image is obtained of which the phase image is modulated by the

same pattern as the tag lines. Tissue tracking can therefore be performed by tracking the phase of the HARP image. Figure 2.6 illustrates this concept.

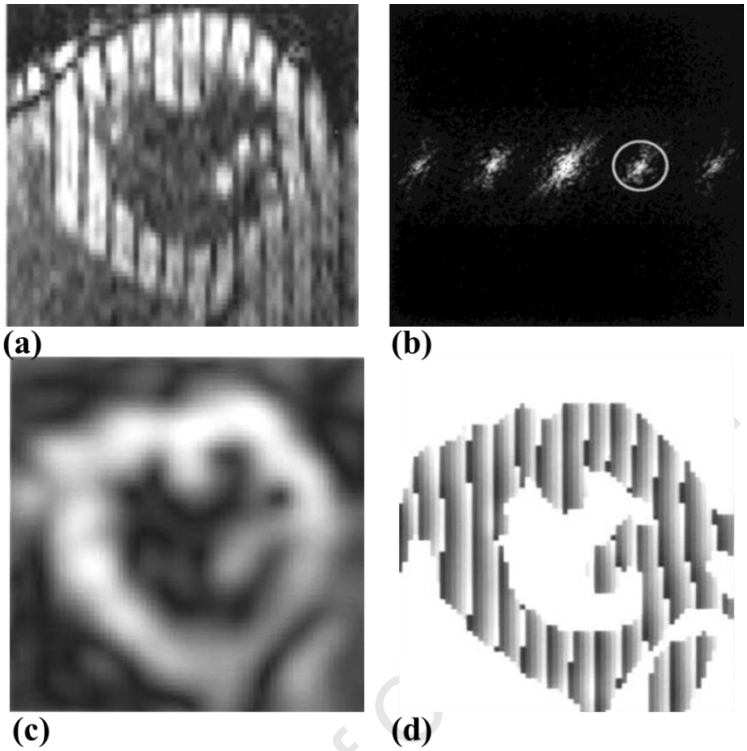

Figure 2.6: Illustration of the steps involved in HARP analyses. (a) 1D tagged magnitude image, (b) k-space peak that will be isolated with a bandpass filter, (c) magnitude image of the inverse Fourier transform of the filtered peak and (d) HARP phase image that is used for tracking. Image adapted from Osman et al. [14].

Drawbacks of tagging include the inherent tag spacing, which limits the achievable resolution of myocardial tagging. Furthermore, multiple orthogonal slices are required in order to capture 3D motion, resulting in lengthy data acquisition times [15]. Kuijer et al. describe methods used to calculate 2D and 3D strains from deformation gradients derived from tagged data acquired in multiple directions and image orientations [16], while Moore et al. evaluated 3D strain of the LV using myocardial tagging [12].

2.5.2 Phase contrast velocity encoding

Phase contrast (PC) velocity encoding is an MR technique that encodes instantaneous tissue velocity directly into the pixel phase and can be used to map both the velocity of blood and myocardium [17-19]. This is achieved by using two opposing gradient

pulses. The spin phasing and dephasing effects of the two opposing gradients will cancel each other out in stationary tissue. However, if tissue motion occurs in the time between the pulses, a phase shift results which are directly proportional to the velocity along the direction of the gradients. An advantage of velocity encoding techniques is the ability to extract strain rate (measure of the time evolution of deformation of the myocardium) directly from the velocity data without needing to segment myocardial contours [20]. Zhu et al. presented a method to compute a strain tensor in order to evaluate intramyocardial deformation [21] using tissue tracking methods described in [22]. PC velocity encoding is often used to quantify and assess blood flow. Three dimensional spatial encoding with PC MRI enables visualization of the complex flow and motion patterns of the blood in the thoracic aorta in 3D [23]. Unlike myocardial tagging, PC velocity encoding benefits from a high spatial resolution with velocity measures at a voxel resolution. Because PC data does not directly measure displacement, but rather a strain rate, displacement and strain calculations are not trivial as an additional integration step is required in order to compute displacement [22]. Due to the accumulation of an integration error that arises from using phase information of other cardiac phases, an additional bi-directional integration step using the periodicity of cardiac motion is necessary.

2.5.3 Displacement encoding with stimulated echoes

Displacement encoding with stimulated echoes (DENSE) is a technique that combines the advantages of both myocardial tagging and PC velocity encoding, and is capable of measuring displacements over longer periods of time at a high spatial resolution. DENSE is a quantitative myocardial wall motion imaging technique which encodes tissue displacement directly into the image phase [2]. DENSE allows for the direct extraction of displacement relative to the time of encoding (typically end diastole) at a pixel resolution.

The DENSE pulse sequence to measure displacement in the x-direction is illustrated in Figure 2.7. DENSE allows for encoding in any direction, but is typically applied in 2-3 orthogonal directions. As with tagging, DENSE MR imaging contains a spatial modulation of magnetization (1-1 SPAMM) kernel in order to position encode the longitudinal magnetization [3]. Displacement is accumulated during a long mixing

period, which is followed by an rf pulse flipping the magnetization onto the transverse (x-y plane). A second gradient lobe of the same amplitude as the first, but with a reversed polarity is applied, rewinding the phase dispersion caused by the first lobe of the tagging kernel. For stationary spins, there is a zero net phase, however, for spins that have moved Δx, the phase accrual is proportional to the displacement. Because all displacement information is stored in the phase image, any phase inhomogeneity's need to be corrected. In DENSE, a phase reference scan is subtracted from the phase of the encoded image so that tissue with zero displacement has zero phase.

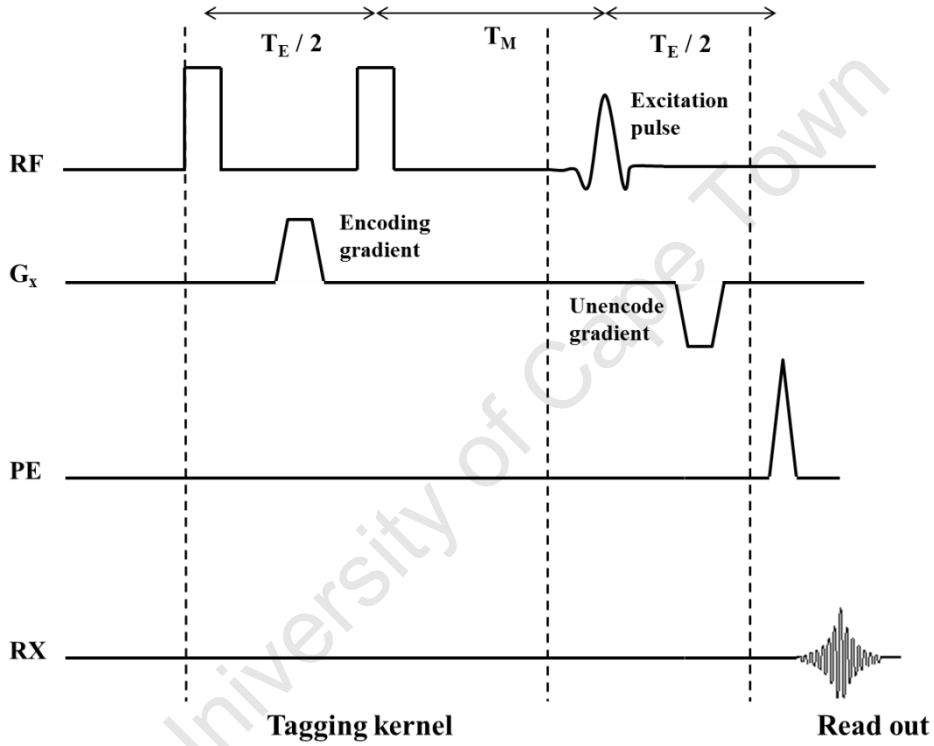

Figure 2.7: Schematic timing diagram of the DENSE pulse sequence: RF – radio frequency pulse; G_x – magnetic gradient in the horizontal direction; PE – phase encoding pulse; RX – receiver coil; T_E – echo time; T_M – mixing time. The encoding and unencoding gradients are of same magnitude, but opposite signs.

For an arbitrary spin with image coordinate $\mathbf{x} = (x_1, x_2)$, the transverse magnetization M_{xy} in the x encoding direction, is given by Equation 2.8.

$$\mathbf{M_{xy}}(x,t) = \frac{M_{z0}}{2}\sin(\alpha)e^{\frac{-t}{T_1}}e^{-jk_e\Delta x} + \frac{M_{z0}}{2}\sin(\alpha)e^{\frac{-t}{T_1}}e^{-jk_e(\Delta x+2x)} + M_0\sin(\alpha)(1-e^{\frac{-t}{T_1}})e^{-jk_e(\Delta x+x)} \quad (2.8)$$

where M_0 is the thermal equilibrium value of the longitudinal magnetization, M_{z0} is the longitudinal magnetization prior to the application of the displacement encoding pulse, α is the flip angle due to the excitation pulse, Δx is the tissue displacement which occurred in the x-direction between the tagging and measurement, and k_e is the phase encoding frequency.

Equation 2.8 comprises three terms, each of which represent a distinct echo in k-space, the stimulated echo (phase directly proportional to displacement), complex conjugate echo and the T_1 relaxation echo. Figure 2.8(a) illustrates the position of each echo in k-space for a stationary phantom, k = (0, 0), ($2k_e$, 0) and (k_e, 0), respectively.

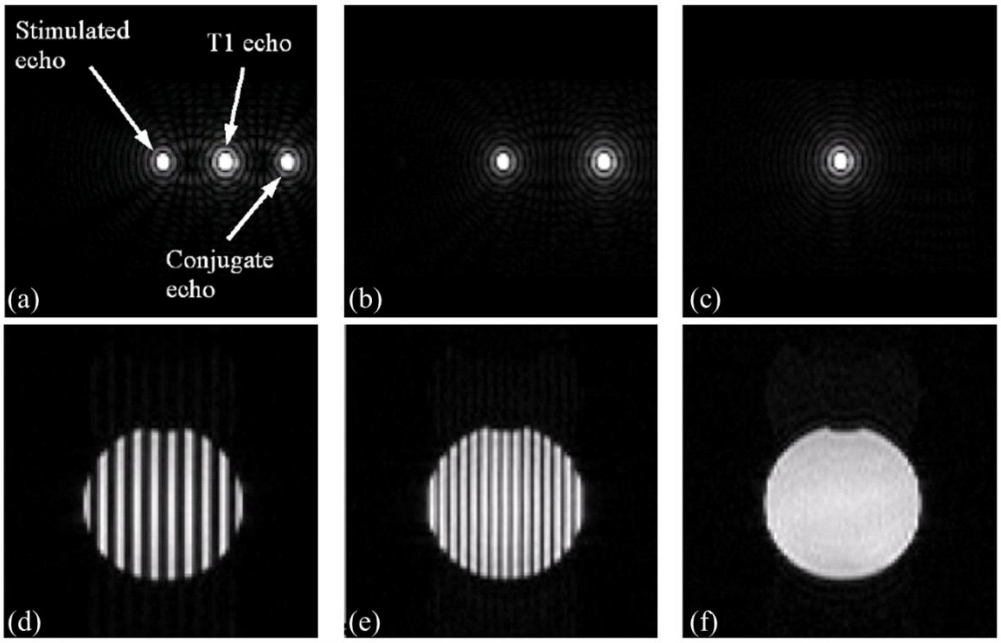

Figure 2.8: K-space images of a stationary phantom with corresponding magnitude images, showing the effects of artefact-generating DENSE echoes and the results after each echo is suppressed. (a, d) illustrate k-space and magnitude images after the stimulated echo is centred by the unencoding gradient, (b, e) illustrate k-space after k_e has been set high enough in order to shift the conjugate echo out of k-space, and its corresponding magnitude image, and (c, f) effects of removing the T_1 echo with CSPAMM, and the corresponding magnitude image, with no artefacts.Images adapted from Xiaodong Zhong, PhD.

The two high frequency artefact generating echoes are suppressed in order to ensure only the stimulated echo contributes to the image. If not, Figure 2.8(d) illustrates the tag line artefacts created by the undesired echoes on the DENSE magnitude image. The complex conjugate echo is suppressed by setting the encoding frequency k_e high enough to shift the conjugate echo out of the sampled k-space. Kim et al. showed how complimentary SPAMM (CSPAMM) can be used to suppress the T_1 echo [3]. CSPAMM is a technique used in myocardial tagging in order to compensate for the fading of tag lines due to T_1 relaxation [24]. A CSPAMM subtraction further improves the SNR by signal averaging and doubles the magnitude of the stimulated echo and the complex conjugate echo. Other methods such as inversion recovery [25] and various degrees of phase cycling [3, 26] have also been used to suppress the T_1 echo. However, inversion recovery can only be done at a single time point, therefore it is not ideal for cine DENSE. Phase cycling has been shown to suppress and isolate either of the echoes and improve SNR, but at the expense of a lengthy scan time.

Equation 2.8 shows that the stimulated echo / DENSE magnetization decays according to T_1 and is reduced by a factor of 2, indicating that the DENSE signal has of only ½ the magnitude when compared to a normal echo. This is an inherent limitation of stimulated echo techniques.

Figure 2.9 illustrates DENSE reconstructed magnitude and phase images encoded in the vertical direction, with the corresponding displacement vectors derived from horizontal and vertically encoded DENSE data at three different times in the cardiac cycle. The measured signal in the phase images is bound between the limits of $\{-\pi:\pi\}$. The true phase is thus wrapped within this range and therefore phase unwrapping is required to obtain absolute displacement measurements. Using manually defined epicardial and endocardial contours and phase unwrapping methods presented in [27], the unwrapped phase images are obtained. Once the phase unwrapping algorithm has been implemented, the corresponding displacement field is derived from the cine DENSE images.

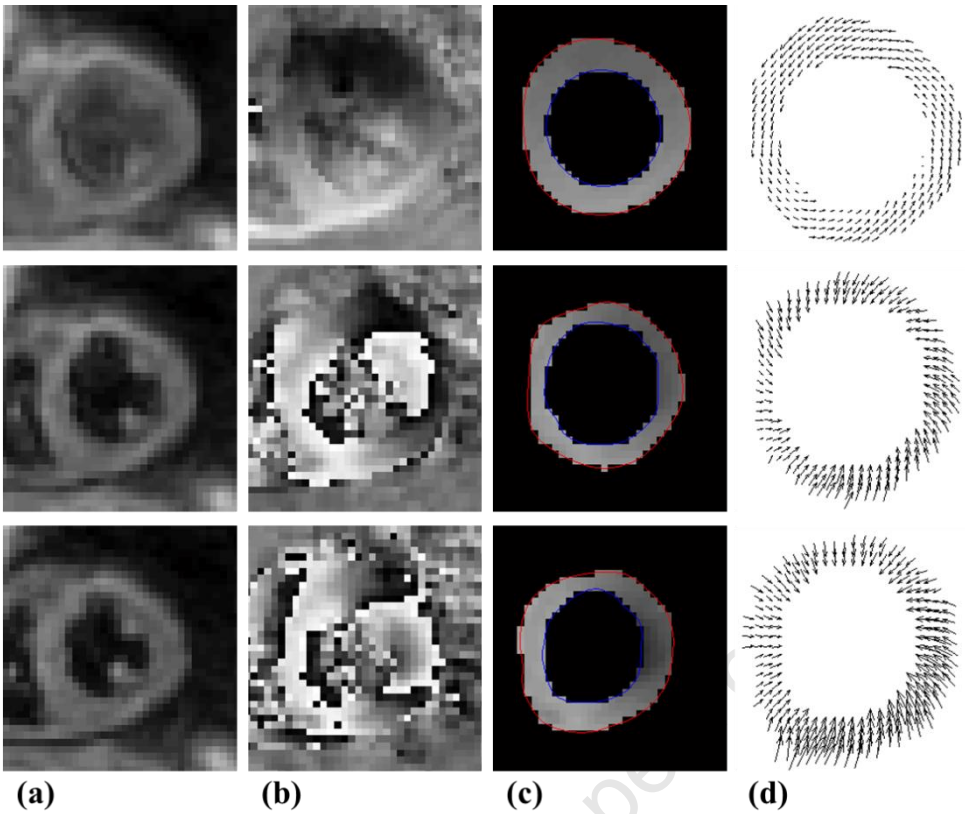

Figure 2.9: (a) Cine DENSE magnitude-reconstructed images at early systole (top), mid systole (middle) and end systole (bottom). (b) Corresponding phase reconstructed DENSE images encoded for motion in the vertical direction. (c) Unwrapped DENSE phase images after LV contouring and applying the phase unwrapping algorithm. Light pixels indicate motion to the right and dark pixels indicate motion to the left. (d) Corresponding DENSE displacement fields derived from unwrapped phase images encoded in both horizontal and vertical directions.

To date, the majority of DENSE applications focus on 2D imaging of a single slice. Since the heart contracts and moves in a 3D manner, 3D volumetric information if preferred. Recently, a free-breathing navigator-gated 3D spiral cine DENSE sequence has been developed to quantify tissue motion and strain in three dimensions within the entire LV and RV in a single scan [4].

The 3D sequence can be divided into three parts. During 2D DENSE data acquisition, in order to reduce respiratory motion artefacts, patients are asked to hold his / her breath during each scanning sequence. By contrast, the use of a navigator allows subjects to breathe freely during the scan while reducing respiratory motion artefacts by only using data acquired when the diaphragm is located within a predefined region. Due to long scan times for 3D DENSE, navigator methods were used. The first part of

the sequence comprises of the navigator and fat suppression pulses. The navigator echo is run before the ECG trigger so as to not interfere with the displacement encoding module. A cross-pair navigator echo is implemented using two orthogonal slice selective 90º and 180º rf pulses. The slice orientations of each RF pulse must be accurate to prevent interference of the echo with the magnetization of the heart. Furthermore, a fat suppression pulse applied prior to the displacement encoding module reduces the contribution of fat to the displacement encoding magnetization. The second module is the displacement encoding module, which is implemented using balanced multi-point displacement encoding strategies. There are three advantages to multi-point encoding, namely equivalent phase noise in all directions, increased signal to noise ratio (SNR) for a fixed k_e, and extension for signal averaging. Three-point phase cycling was used to suppress artefact generating echoes. A combination of CSPAMM and cosine and sine modulation methods was used. The displacement encoding module is followed by the spiral readout module, which samples k-space using an interleaved stack of spiral trajectories. Spiral readout increases SNR when compared to an echo-planar approach. A ramped flip angle was introduced in order to ensure an equalized SNR for all cardiac phases. Two disadvantages of 3D DENSE are lengthy scan times and the need to manually segment the myocardium, which restrict its application to the clinical environment.

3D spiral cine DENSE offers better spatial resolution and improved SNR over myocardial tagging and PC velocity encoding. While previous studies have been limited to the LV, analysis of the motion of the RV now becomes possible. A 3D segmentation algorithm is, however, required to reduce the lengthy segmentation time and provide a fully automated solution. In order to assess its ability to assist with the diagnosis and management of cardiac disease, DENSE requires application in diseased hearts. The present thesis presents some solutions to the analysis of 3D DENSE data, both in terms of RV analyses and an automated segmentation algorithm for the LV.

The data used in Chapters 3 and 4 for the analysis and quantification of myocardial motion and strain were acquired from healthy volunteers using the navigator-guided

3D spiral cine DENSE sequence, providing a temporal resolution of 32 ms and spatial resolution of $2.8 \times 2.8 \times 10\ mm^3$.

2.6 Assessing myocardial mechanics using DENSE MRI

A series of post processing steps are required for the analysis of DENSE MRI data. This includes: segmentation, phase unwrapping and displacement extraction, tissue tracking, temporal fitting, and strain calculation.

Phase unwrapping uses spatiotemporal phase unwrapping methods described by Spottiswoode et al. that have been extended to 3D [27]. It is performed within a contoured region in order to remove phase aliasing. The phase data from the 3 encoding directions are combined to create 3D Eulerian displacement fields. Figure 2.10 illustrates contoured DENSE magnitude and unwrapped phase images and the corresponding 3D vector displacement fields during end systole for a single short axis slice. The accuracy, speed and robustness of the phase unwrapping depends on the accurate delineation of the myocardium from surrounding anatomical structures. Segmentation of the myocardium is discussed at length in section 2.8.

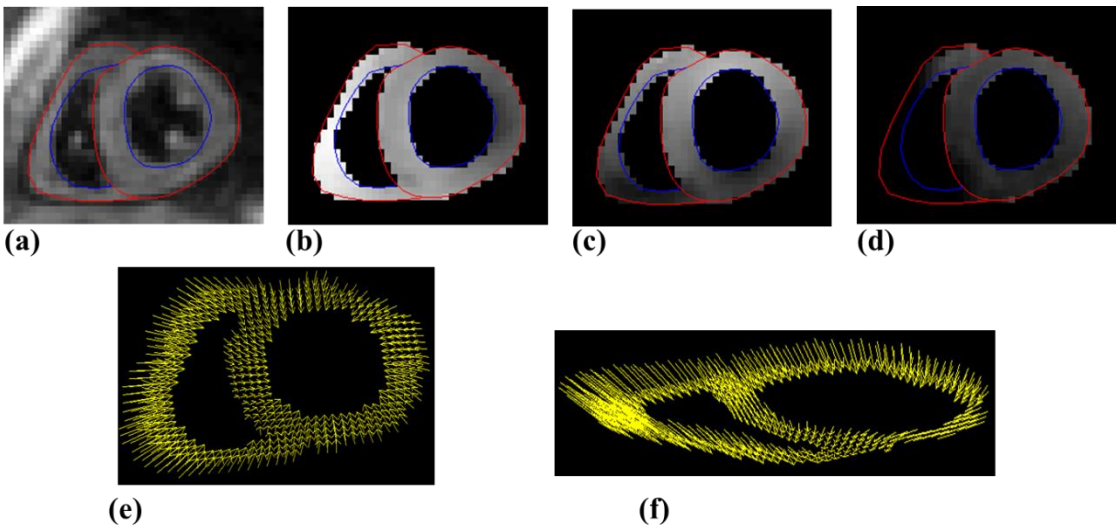

Figure 2.10: A single short axis slice of 3D cine DENSE data during mid systole. The data is shown with epicardial (red) and endocardial (blue) contours. (a) DENSE reconstructed magnitude image, (b, c, d) DENSE unwrapped phase images encoded for motion in the x, y, z directions, respectively. (e, f) In plane and through plane views of the corresponding 3D vector displacement field. Notice the direction of each vector towards the center of the image, illustrating contraction of the myocardium.

Three dimensional imaging and tissue tracking techniques are required to accurately capture the highly complex 3D motion and contraction patterns of the heart. This will allow for appropriate 3D strain tensor calculations and representation of the fiber architecture of the heart wall, which can assist with diagnosis of diseases that are patchy in their manifestation, such as Arrythmogenic Right Ventricular Cardiomyopathy.

2.6.1 Tissue tracking and temporal fitting

Myocardial 3D tracking is necessary for volumetric strain analysis. Three dimensional tissue tracking using myocardial tagging involves images in both short and long axes. However, the spatial resolution is limited by both the tag spacing and the intersection between short-axis and long-axis data. The 3D motion is therefore often quantified with the use of 3D geometrical models of the LV and RV [28-30]. Using 3D DENSE, 3D motion can be quantified without using geometrical models.

In DENSE, the displacement of each voxel is encoded as a phase shift that has accrued since the time of encoding. Therefore, each displacement vector throughout

the cardiac cycle will reference the material position of the myocardium at the time of encoding (t_0). DENSE displacement vectors can be visualized as having their heads positioned at the centre of the myocardial voxel, while the tail originates from the reference position at the time of displacement encoding, which may or may not be at the centre of a voxel. Displacement fields allow for a direct and independent calculation of strain at each time frame. However, the use of these vectors as indicators of myocardial motion and deformation is limited as they provide a net measurement of displacement from t_0, and not a frame-to-frame measurement. A method for calculating and acquiring the frame-to-frame motion trajectories of each voxel within the myocardium has been implemented for 2D DENSE. Motion trajectories are obtained as follows: If the centre of an arbitrary voxel within the myocardium is chosen at an end diastolic time frame, the three closest vectors to this point are identified. These vectors are depicted by the red vectors in Figure 2.11(a, b). Using the three chosen vectors, two dimensional distance-weighted linear interpolation is used to obtain an estimate of the displacement vector of the chosen voxel for this time frame. This is illustrated in Figure 2.11 by the blue vector. This is done at each time frame. The motion trajectory of the voxel is then calculated by subtracting the interpolated vector of successive frames from one another, thus providing the motion trajectory for the material point, as depicted in Figure 2.11(c). These trajectories are then used for the calculation of myocardial strain [27].

The 2D DENSE tracking method described above can be extended to 3D with certain modifications.

Using slice following, Spottiswoode et al. incorporated 3D tissue tracking in 2D cine DENSE [31] in order to compensate for through plane motion. As the origin of each vector in the displacement field lie in the same imaging plane, similar methods as those described above were used.

However, in 3D cine DENSE, displacement is encoded in both the through plane direction and in plane directions, resulting in 3D vector fields, where vector heads lie in the plane, while the corresponding vector tail is projecting from out of the image plane to their position at the time of encoding. As the reference position of each voxel

is required for tissue tracking, tracking the motion of voxels in a single slice requires inclusion of displacement vectors of multiple adjacent slices. Thus, when tracking voxels on each slice, the three closest neighbouring slices are used to interpolate each displacement vector. This method can be implemented for both the LV and RV.

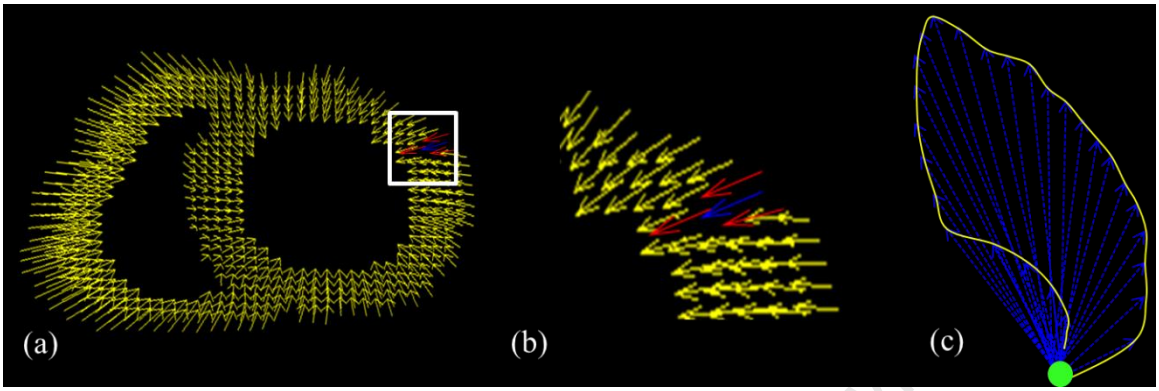

Figure 2.11: Tissue tracking illustration for 2D cine DENSE data. (a) Eulerian vector displacement field during systole. The blue vector tail depicts the material point of interest, and the three red vectors are the closest vectors at *this* frame that are used for interpolation. The blue vector is the interpolated vector. (b) A magnified view. (c) The motion trajectory for the chosen material point, calculated by subtracting interpolated vectors at successive time frames.

The frame-to-frame trajectory obtained using tissue tracking is usually contaminated by image noise. In cine DENSE, the measured displacements are independent of cardiac phase, providing a framework suited to temporal fitting. The accuracy of a point's position can therefore be improved by providing an estimate of its position at the preceding cardiac phase. This is accomplished by fitting curves to each of the spatial coordinate components as a function of time.

The periodic and natural behaviour of cardiac motion suggests that a periodic descriptor should be used for the fit. Fourier basis functions (5^{th} order) have been shown to be suitable to describe cardiac motion [32]. In practice, it is common that not a full cardiac cycle be imaged. Therefore, the missing positions at the end of the fit are linearly interpolated back to the starting point. This has two disadvantages: firstly, if the unsampled portion is large, this can significantly affect the temporal fit and, secondly, the percentage corresponding to the sampled portion of the cardiac cycle is needed and is sometimes difficult to determine. Polynomial fitting was

therefore used in order to avoid possible fitting errors, as well as due to its simplicity and robustness [27, 33]. Temporal fitting was done for each ordinate direction of each of the trajectories using a 10th order polynomial, which is analogous to a 5th Fourier basis function. Figure 2.12 illustrates the concept by applying 2D temporal fitting using 5^{th} order Fourier basis functions in order to smooth the motion trajectory.

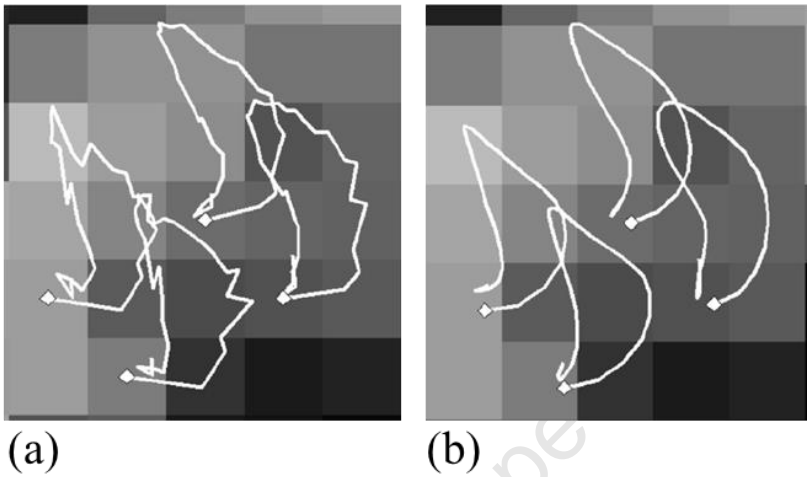

Figure 2.12: Motion trajectories of four different voxels. (a) Raw trajectories, (b) corresponding fitted trajectories. Image adapted from Xiaodong Zhong, PhD.

2.6.2 Strain calculation

Strain is a measure of contraction and / or expansion of a material at one point in time, relative to the material's state at another point in time. Lagrangian strain is commonly reported in myocardial mechanics as it measures the deformation of the myocardium relative to end diastole.

Calculating strain from the trajectories of the tracked myocardium offers various advantages. As the motion trajectories can be evaluated at any point in time, strain can be calculated at any desired temporal resolution. Furthermore, the myocardial deformation can be viewed and analysed at a pixel resolution throughout the cardiac cycle. A standard method of representing strain in cardiac MR is by producing strain-time curves. Each curve presents the evolution of strain across the cardiac cycle averaged over a circumferential segment of the myocardium.

The deformation gradient tensor **F** describes the state of the material post-deformation. The tensor is derived from three co-planar vectors, given by Equation 2.9. Consider a single trajectory position X = (x_1, x_2, x_3) at some cardiac frame. Looking at trajectories around X, L = (x_1 - 1, x_2, x_3), R = (x_1 + 1, x_2, x_3), U = (x_1, x_2 + 1, x_3), B = (x_1, x_2 - 1, x_3), A = (x_1, x_2, x_3 - 1) and P = (x_1, x_2, x_3 + 1) correspond to trajectory points to the left, right, above, below, anterior and posterior of X, respectively. From these six points around X, any three co-planar vectors (V_1, V_2 and V_3) can be formed, corresponding to either configuration UXRA, UXRP, UXLA, UXLP, DXRA, DXRP, DXLA and DXLP. These configurations are present for the majority of the pixels in the myocardium.

$$\mathbf{F} = [\mathbf{V_1'V_2'V_3'}] / [\mathbf{V_1V_2V_3}] \tag{2.9}$$

where $\mathbf{V_1}$, $\mathbf{V_2}$ and $\mathbf{V_3}$ represent the pre-deformation vectors forming the columns of one matrix and $\mathbf{V'_1}$, $\mathbf{V'_2}$ and $\mathbf{V'_3}$ represent the corresponding post-deformation vectors and form the columns of another matrix. The "/" operator is a matrix right division.

The deformation gradient tensor (**F**) is calculated using spatial derivatives, which is highly sensitive to noise. Furthermore, regions where there are fewer neighbouring points such as the ventricular septum or the basal and apical slices at the extremities, a further error can result from this approximation. It is worth noting that this error caused by points in alternate slices is higher, as the through plane resolution is greater than the in plane resolution. To reduce this error, a number of points can be chosen within a neighbourhood and **F** can be approximated using a linear least-squares approach. Alternatively, **F** can also be calculated using single value decomposition with similar methods that include N nearest available neighbour voxel positions.

The Lagrangian finite strain tensor (**E**) describes the systolic deformation relative to end diastole. The principal strains ($\mathbf{E}_1$, $\mathbf{E}_2$ and $\mathbf{E}_3$) are defined by the eigenvalues corresponding to the strain tensor **E**. Each principal strain is associated with a corresponding principal direction along which the deformation occurs; this is described by the eigenvectors of the strain tensor **E**. The Lagrangian strain tensor can be calculated by Equation 2.10.

$$\mathbf{E} = \frac{1}{2}(\mathbf{F}^{\mathrm{T}}\mathbf{F} - \mathbf{I}) \tag{2.10}$$

where T denotes the transpose operation and **I** is the identity matrix. The Lagrangian strain tensor is calculated for each vector configuration for each voxel (X).

In cardiac MRI, the strain tensor is normally aligned to a coordinate system [12, 28] of which the axes are defined as radial, circumferential and longitudinal. The strain tensor **E** can be decomposed into first, second and third principal strains, which correspond to the axes of the coordinate system. Principal strain magnitudes are calculated using the eigenvalues of **E** and each principal strain direction is calculated using the eigenvectors of **E**.

Cerqueira et al. described a standardized way of dividing the LV into anatomical segments in order to describe characteristics of the myocardium in different areas [34]. Currently, there is no standard for dividing the RV into anatomical segments, however, a method that uses anatomical landmarks is proposed in Chapter 3.

2.7 Measuring right ventricular mechanics

A limited number of studies have characterised RV motion using MRI. These studies include techniques such as myocardial tagging, phase contrast velocity encoding, and DENSE MRI. As described above, the RV receives deoxygenated blood from the right atrium and pumps it to the pulmonary circulation for oxygenation. The RV shares the interventricular septum with the LV and as such, many diseases affecting the RV can inevitably affect the LV, and vice versa. A technique capable of quantifying abnormal RV kinematics could help diagnose the presence and severity of such diseases.

Characterizing the kinematics of the RV is a challenging task due to its thin walls, complex geometry and irregular motion. There have been a few myocardial tagging studies that have successfully reconstructed and analysed the 3D motion of the RV [28, 30, 35]. Due to the thin wall of the RV, a limited number of tag lines fall on the RV wall so that both tag data and contour data have to be used to reconstruct the 3D motion [35]. Methods therefore include multiple imaging views and 3D motion

reconstruction techniques using a biventricular finite element model. A local coordinate system is typically defined for the RV, thus allowing for displacement information to be acquired in the radial direction. Young et al. used similar methods to assess the RV mid-wall surface motion and strain by fitting a finite element model to the RV mid-wall surface [30]. Fayad et al. presented a model free 1D tangential surface strain in the longitudinal and circumferential directions [36].

MR imaging of the RV relies heavily on endocardial and epicardial contours. PC velocity encoding MR imaging ensures high spatial and temporal resolution while measuring the velocity of the myocardium between demarcated contours [37].

The pioneering paper by Aletras et al. demonstrated how DENSE provides a high density measure of myocardial displacement for both left and right ventricles in an intact canine heart for a single cardiac phase [2]. Wen et al. performed a study on displacement encoded data in order to determine the effects of two adaptive post processing techniques, namely phase unwrapping and noise suppression [38]. While epicardial and endocardial contours were drawn for the LV, only a mid-line contour was drawn for the RV due to its thin myocardial wall. Circumferential strain was calculated and assessed. There are no comprehensive studies of the RV using DENSE. In the analysis of LV-RV inter ventricular dyssynchrony, methods to study the RV using 2D cine DENSE have been introduced [39].

2.8 Myocardial Segmentation

In MRI, the demarcation of myocardium using epicardial and endocardial borders is essential for the analysis of regional cardiac displacement and strain. Segmentation of cardiac images is a complex problem as the heart is a non-rigid moving organ, which is in turn being displaced by respiratory motion. Furthermore, the heart illustrates fewer anatomical landmarks when compared to other organs (such as the brain), making the task even more challenging.

The anatomical nature of the heart and signal limitations of MRI makes it difficult to distinguish the myocardial boundaries. Currently, in cine DENSE MRI and most other cardiac MR techniques, the segmentation process is dependent on human interaction,

whereby the user manually demarcates the ventricles from surrounding structures. The accuracy of this method is left to the user's interpretation, making the process prone to inconsistencies and incredibly time consuming. Computer aided segmentation has the potential to offer more time efficient and accurate results when compared to manual segmentation. Extensive research has therefore been allocated to formulating various semi-automated and automated methods for segmenting the myocardium in medical images.

There are a number of segmentation methods that can be implemented to accurately delineate the myocardium from surrounding structures. Methods include thresholding, classifiers, clustering, random field models, and deformable models. Each technique, however, is most effective under certain conditions and for specific imaging techniques. Current segmentation techniques struggle to delineate accurate myocardial boundaries in a fully automated manner due to poor image quality, lack of clear delineation between myocardium and surrounding structures, and the complex shape and motion of the heart [40].

Active contour models (snakes) introduced by Kass et al. (1988) have been used widely in cardiac segmentation [41]. Snakes are deformable contours moving within certain deformation constraints and under the influence of the image forces. Image forces typically include the image gradient which pushes the contour towards the high contrast boundary of the image, resulting in boundary tracking. A number of modified active contour models have been created in order to obtain more accurate and stable results [40, 42, 43]. Rueckert and Burger proposed geometrical templates where the deformation is controlled by an energy function [44]. The function is based on non-affine deformation of the template from its equilibrium shape based on prior shape information. Cho and Benkeser demonstrate how active contour models use encoded motion information images to derive external forces. Here, they implement a tensor based orientation gradient force (OGF) that uses the bidirectional velocity images from PC MRI to differentiate between myocardial motion and blood flow [40].

The first fully automated segmentation algorithm for tagged MRI was proposed by Montillo et al. whereby deformable surface models were applied to the ventricles in

order to segment the myocardium [45]. Here the myocardium is delineated into three surfaces, two endocardial surfaces, one for each ventricle and a common epicardial surface for both ventricles. Each surface is initialized to an approximation of the required surface and then deforms under image forces to fit the image data. Young et al. proposed a semi-automated segmentation method for tagged MRI data, where a user defines the LV borders by placing guide points along the boundaries [46]. Although it still requires user interaction, defining the boundaries with a single mouse 'click' improves the accuracy and reduces the manual segmentation time required. Both methods by Montillo and Young employ finite element models.

While there has been a number of segmentation algorithms developed for MRI, there has been little development of segmentation algorithms for cine DENSE MR images. Spottiswoode et al. presented a 2D semi-automated segmentation technique that uses the encoded motion of the myocardium to project a manually defined region of interest (ROI) through the cardiac cycle [47]. The method shows promise for the segmentation of DENSE MR data as it uses the inherent property of displacement encoding. The algorithm is, however, dependent on accurate phase unwrapping and displacement vector calculations [27]. Chen et al. presented a semi-automated method for the segmentation of 2D cine DENSE by introducing a segmentation model [48]. The model is divided into two steps, preparation and evolution. The preparation step includes image cropping and image processing for intensity standardization. The second / evolution step is driven by a minimization of the energy function. This was based on work by Pluempitiwiriyawej et al. to present novel active contour segmentation methods [49].

The time consuming and laborious process of manual LV demarcation limits imaging techniques such as DENSE from being routinely employed in clinical practice. It would therefore be beneficial if an accurate and reliable myocardial segmentation algorithm could be developed to assist medical practitioners in their understanding of cardiac motion and function as well as in the diagnosis of heart related diseases.

Chapter 3

Mapping Right Ventricular Myocardial Mechanics using 3D cine DENSE MRI

Daniel A. Auger, Xiaodong Zhong, Frederick H. Epstein, Bruce S. Spottiswoode

Abstract

The mechanics of the right ventricle (RV) are not well understood as studies of the RV have been limited. This is, in part, due to the RV's thin wall, asymmetric geometry and irregular motion. However, the RV plays an important role in cardiovascular function. This study aims to describe the complex mechanics of the healthy RV using three dimensional (3D) cine displacement encoding with stimulated echoes (DENSE) MRI. Whole heart 3D cine DENSE data were acquired from five healthy volunteers. Tailored post processing algorithms for RV mid-wall tissue tracking and strain estimation are presented. A method for sub-dividing the RV into four regions according to anatomical land marks is proposed, and the temporal evolution of strain was assessed in these regions. The 3D cine DENSE tissue tracking methods successfully capture the motion and deformation of the RV at a high spatial resolution in all volunteers. The regional Lagrangian peak surface strain and time to peak values correspond with previous studies using tagged and strain encoded MRI. The inflow region consistently displays lower peak strains than the apical and outflow regions, and the time-to-peak strains suggest RV mechanical activation in the following order: inflow, outflow, mid, then apex. Model-free techniques have been developed to study the myocardial mechanics of the RV at a high spatial resolution using 3D cine DENSE MRI. The consistency of the regional RV strain patterns across healthy subjects is encouraging and the techniques may have clinical utility in assessing disrupted RV mechanics in the diseased heart.

3.1 Background

Right ventricular (RV) function may be impaired in a number of heart conditions, including myocardial infarction, congenital heart disease and cardiomyopathy [50]. The function of the RV may also be affected in diseases of the left ventricle (LV) where it is difficult to ignore the complex nature of ventricular interaction [51, 52].In the past, the importance of the LV in cardiac research has overshadowed the study of the RV. This neglect is, in part, because the RV is difficult to image. The wall of the RV myocardium is thin (2-5 mm) when compared to that of the LV (7-11 mm) [51]. Furthermore, the RV has a complex geometry, eccentric motion [28, 50] and it is heavily trabeculated, thus it does not offer the clearly defined endocardial margins typically seen in the LV.

Various MRI studies have assessed properties such as strain, motion and volumes of the RV. The MRI techniques used include turbo gradient echo and steady state free precession (SSFP) [53], myocardial tagging [28, 30, 35],phase contrast velocity encoding [37] and strain encoded (SENC) MRI [54].

The standard cardiac imaging planes are based on the relatively uncomplicated geometry of the LV. However, no standardized localization exists for the RV. Two dimensional strain estimates of the LV are reliable in short axis views because the through plane motion is relatively uniform [55]. This does not apply to the RV because of its complex shape and motion, so 2D imaging may be insufficient to accurately assess strain in the RV [28]. To date, no detailed studies of the RV have been presented using displacement encoding with stimulated echoes (DENSE) MRI.

DENSE is a quantitative MRI technique used for measuring myocardial displacement and strain. DENSE encodes tissue displacement directly into the image phase (typically with reference to end diastole), thus allowing for the extraction of motion data at a pixel resolution [2, 3]. A recently developed free breathing 3D cine DENSE sequence [4] is well suited for quantifying the complex behavior of the RV. A high signal to noise ratio (SNR), which is necessary for imaging the thin RV walls, is achieved using a spiral k-space trajectory and three point phase cycling. Furthermore,

DENSE is inherently a black-blood technique, which together with fat suppression, provides a more accurate delineation of the RV walls.

The purpose of this study was to develop tailored processing techniques for assessing detailed 3D RV motion and surface strain using cine DENSE, and to quantify these parameters for the healthy human heart.

3.2 Materials and Methods

3.2.1 Imaging protocol

Whole heart 3D cine DENSE data were acquired from five healthy male volunteers (age range 21 – 45) on a 1.5T MRI scanner (Siemens MAGNETOM Avanto, Erlangen, Germany) using a two-channel anterior body array coil and an eight-channel spine array coil.

The entire heart was imaged with the imaging volume aligned along the heart's long axis and at a 2.8 × 2.8 × 10 mm^3 spatial resolution and 32 ms temporal resolution. Fourteen 3D partitions were acquired. Displacement was encoded in three orthogonal directions and a spiral k-space trajectory was used with 6 interleaves per 3D partition. Images were acquired during a 20.5 ± 5.7 min scan time with prospective ECG gating and diaphragmatic navigator respiratory gating. Other imaging parameters include: field of view = 360 × 360 × 140 mm^3, displacement encoding frequency k_e = 0.06 cycles/mm, ramped flip angle up to 20 degrees, TR = 16 ms, TE = 1.3 ms. Zero-padding was used during image reconstruction to increase the 14 acquired 3D partitions to 28 partitions, reducing the through plane resolution to 5mm. All imaging was conducted after informed consent and in accordance with protocols approved by the University of Virginia Institutional Review Board.

3.2.2 Post processing

A number of tailored post processing steps were implemented to analyze the RV myocardial DENSE data. All software development was performed using MATLAB (The Mathworks, Natick, MA).

3.2.2.1 Contouring, phase unwrapping and tissue tracking

Both the RV and LV myocardium was demarcated from surrounding structures by manually drawing each epicardial and endocardial contour on the reconstructed short-axis DENSE magnitude images.

Spatio-temporal phase unwrapping [27] was performed within the contoured area to remove phase aliasing, and the phase data from the three encoding directions were combined to create 3D Eulerian displacement fields. Figure 3.1 illustrates contoured cine DENSE magnitude and phase-unwrapped images and the corresponding 3D displacement fields for a single short-axis slice.

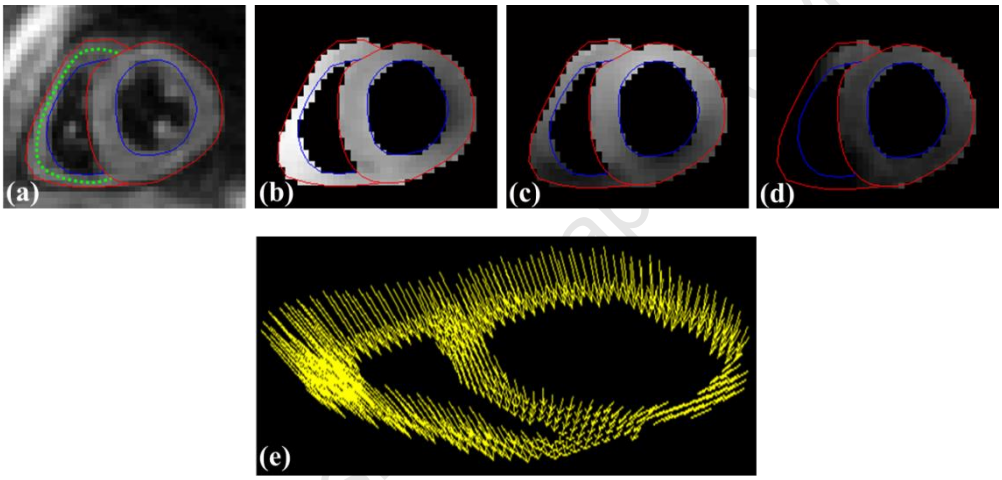

Figure 3.1: A single short axis slice of the 3D cine DENSE data at mid systole. (a) DENSE magnitude image illustrating the myocardial mid-line for the RV (green dotted line). (b, c, d) DENSE unwrapped phase images encoded for motion in the x, y and z directions, respectively. (e) Corresponding 3D DENSE displacement field. Red lines correspond to epicardial surfaces and blue lines correspond to endocardial surfaces.

There are typically too few transmural pixels spanning the RV to acquire a full 3D strain tensor, so we focused on assessing 2D strain at the RV mid-wall surface. The mid-line between epicardial and endocardial contours was used to produce tissue tracking seed points, which were spaced at pixel-distance intervals on the first cardiac phase. The mid-line contours were spatially smoothed within and across partitions using 4^{th} order polynomials fitting to ensure a continuous RV surface. An example of the RV mid-line points is shown in green in Figure 3.1(a).

A 2D tissue tracking algorithm involving interpolation of the displacement fields [27] was directly extended to 3D for this application. The position of each mid-line point along its motion trajectory throughout the cardiac cycle was estimated using 3D distance weighted linear interpolation. The full 3D mid-line motion trajectories were calculated by subtracting the interpolated vectors of successive frames from one another. Prospective gating only allowed about 90 percent of the cardiac cycle to be imaged, therefore, temporal fitting was done for each ordinate direction of each of the trajectories using a 10^{th} order polynomial, as fifth order Fourier basis functions have been shown to sufficiently describe cardiac motion [32].

3.2.2.2 Lagrangian surface strain

Lagrangian strain was calculated directly from the 3D motion trajectories and oriented tangential to the RV mid-line surface. Considering an arbitrary point on the mid-wall, the deformation gradient tensor **F** was calculated using two or four of the nearest neighboring mid-line points as follows

$$\mathbf{F} = [\boldsymbol{V`_1 V`_2 V`_3}] \,/\, [\boldsymbol{V_1 V_2 V_3}] \tag{3.1}$$

where $\mathbf{V_1}$, $\mathbf{V_2}$ and $\mathbf{V_3}$ represent the pre-deformation vectors which are perpendicular to each other in 3D space as shown in Figure 3.2 and form the columns of one matrix, $\mathbf{V`_1}$, $\mathbf{V`_2}$ and $\mathbf{V`_3}$ represent the corresponding post-deformation vectors and form the columns of another matrix, and the "/" operator is a matrix right division.

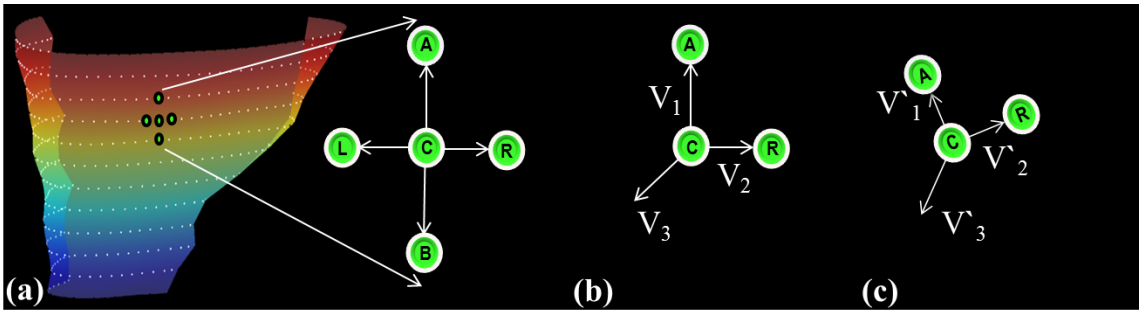

Figure 3.2: 2D Lagrangian surface strain estimation. (a) RV surface image with superimposed mid-line points (white dots) showing all partitions. All possible vector configurations are shown for a chosen point (C) using mid-line points (A)bove, (B)elow, to the (L)eft and to the (R)ight. (b, c) Pre- and post-deformation, respectively, for a single vector configuration. Strain for the chosen point C is calculated using the configuration of points above and to the right (ACR). $\mathbf{V_1}$ and $\mathbf{V_2}$ represent the co-planar vectors formed. $\mathbf{V_3}$ represents the orthogonal unit vector calculated from the cross product of $\mathbf{V_1}$ and $\mathbf{V_2}$. $\mathbf{V`_1}$ and $\mathbf{V`_2}$ represent the corresponding post-deformation co-planar vectors, and $\mathbf{V`_3}$ is the cross product of $\mathbf{V`_1}$ and $\mathbf{V`_2}$.

In practice, depending on the position of the mid-line point on the RV wall, each motion trajectory could have adjacent points to the right and/or left, and on partitions above and/or below. The deformation gradient tensor is therefore calculated for a minimum of two and a maximum of four co-planar vector configurations for each mid-line point. The case of two co-planar vector configuration is illustrated in Figure 3.2 (b) and (c), and Equation 1 for simplicities. Orthogonal unit vectors (e.g. $\mathbf{V_3}$ and $\mathbf{V`_3}$) were created perpendicular to the RV surface using cross products of each set of co-planar vectors. The general case of four co-planar vector configuration is illustrated in Figure 3.2a, and Equation 1 can be extended straightforwardly to include the other co-planar vectors and orthogonal unit vectors so that $\mathbf{F}$ can be calculated more accurately in the statistical sense. Three dimensional Lagrangian strain was then calculated for each deformation gradient configuration as follows

$$\mathbf{E} = \frac{1}{2}(\mathbf{F}^{\mathrm{T}}\mathbf{F} - \mathrm{I}) \tag{3.2}$$

were T denotes the transpose operation, and I represent the identity matrix. Note that this construction of a 3D tensor using a unit normal vector assumes that the cardiac tissue is non-compressible and has been implemented here to simplify the strain calculations. The 3D strain tensor was decomposed into its corresponding eigenvalues (strain) and eigenvectors (direction of deformation). The eigenvalue corresponding to

the orthogonal unit vector (E_1) is aligned with the direction normal to the surface (radial) and is zero because of the aforementioned unit normal vector assumption. The remaining two eigenvalues (E_2 and E_3) provide an estimate of the 2D tangential surface strain. The eigenvalues E_2 and E_3 are of similar magnitude, and there are regional differences in the myofiber (and eigenvector) orientation across the RV surface, so we were unable to discern between E_2 and E_3. The results of the surface strain analysis are thus presented as a mean Lagrangian 2D principal strain. It has been shown that tangential strain in the circumferential and longitudinal directions are good indicators of LV dyssynchrony [56]. In order to infer details about the strain directions in the RV, one dimensional (1D) strains were calculated in the longitudinal and circumferential directions in the same manner as usually done for the LV, and relative to the orientation of the LV. Each 1D strain was calculated from the motion trajectories by only considering points above and below (longitudinal) or to the left and right (circumferential) of each mid-line point.

3.2.2.3 Anatomical sub-divisions for strain-time analyses

Unlike the LV, there is currently no standard method for dividing the RV into anatomical sub-regions. Previous studies of the RV using myocardial tagging adopted different conventions for sub-dividing the RV.

Klein et al. divides each RV basal, mid and apical short axis slice into three regions: superior, mid and inferior [57]. Haber et al. divided the RV into four regions according to anatomical landmarks. The parietal and septal bands were used to demarcate the outflow region, while the free wall was identified based on the normalized height of the septum in a long axis view [28]. Fayad et al. divides the RV using the supraventricular crest (SC), moderator band, papillary muscles and the tricuspid valve as landmarks, creating four distinct regions: the inflow, outflow, mid and apical regions [36].

We propose dividing the RV surface in a similar manner to Fayad et al. These regions are illustrated in Figure 3.3. The divisions were defined by navigating through the 3D DENSE magnitude-reconstructed images and identifying three landmark coordinates as follows:

Coordinate 1: The SC is an accentuation of the muscular wall demarcating the inflow and outflow tracts within the RV. Navigate from apex to base along the short axis magnitude images until the SC appears in the image. The first coordinate is marked on the RV free wall at the level of and adjacent to the SC.

Coordinates 2 and 3: The moderator band is a muscular band connecting the interventricular septum to the anterior papillary muscle of the tricuspid valve. Navigate from base to apex along the short axis magnitude images and define the slice where the moderator band becomes evident as a segment of myocardium crossing the RV cavity. The second and third coordinates are defined as the anterior and inferior RV-LV insertion points at this level, respectively.

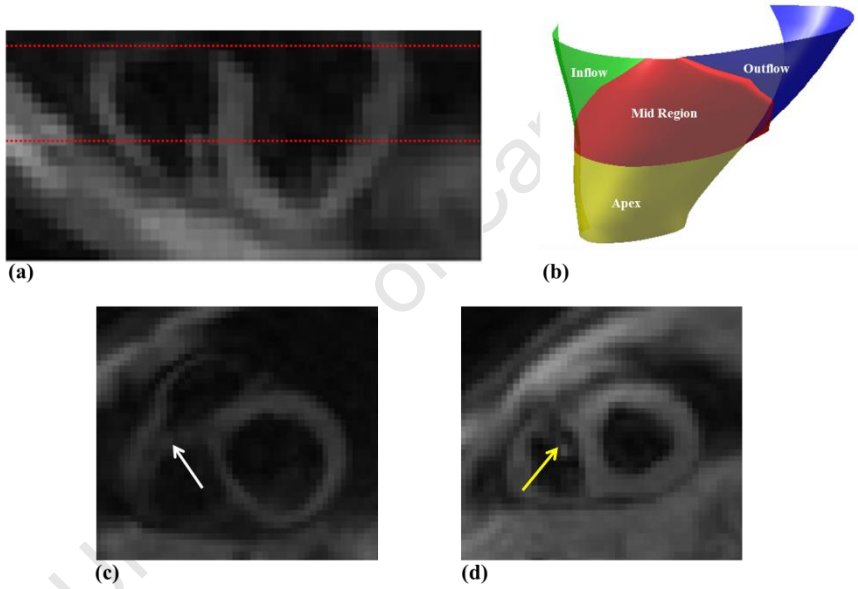

Figure 3.3: Right ventricular regional divisions. (a) Long axis view showing the level of the SC (top red dotted line) and moderator band (bottom red dotted line). (b) RV surface showing the four anatomical regions. (c, d) Short axis view corresponding to the partitions at the level of the SC and moderator band, respectively. The white and yellow arrows show the SC and moderator band, respectively.

The apical RV region is defined as the myocardium lying apical to the slice identified by the moderator band. The inflow, mid and outflow RV regions are defined using two planes defined by the SC and the RV-LV insertion points. The first plane is defined by the SC and the anterior RV-LV insertion point, while the second plane is defined by the points at the SC and the inferior RV-LV insertion point.

The strain values (2D and 1D Lagrangian) were averaged in each of the 4 segments and assessed as through the duration of the cardiac cycle for all 5 volunteers.

3.3 Results

The frame-to-frame 3D mid-line motion trajectories for both the LV and RV are illustrated in Figure 3.4. The red and blue colours represent the positions along the motion trajectories for the RV and LV, respectively. The evolution of displacement during the cardiac cycle can be appreciated in detail, and the large range of motion of the RV compared to the LV is evident.

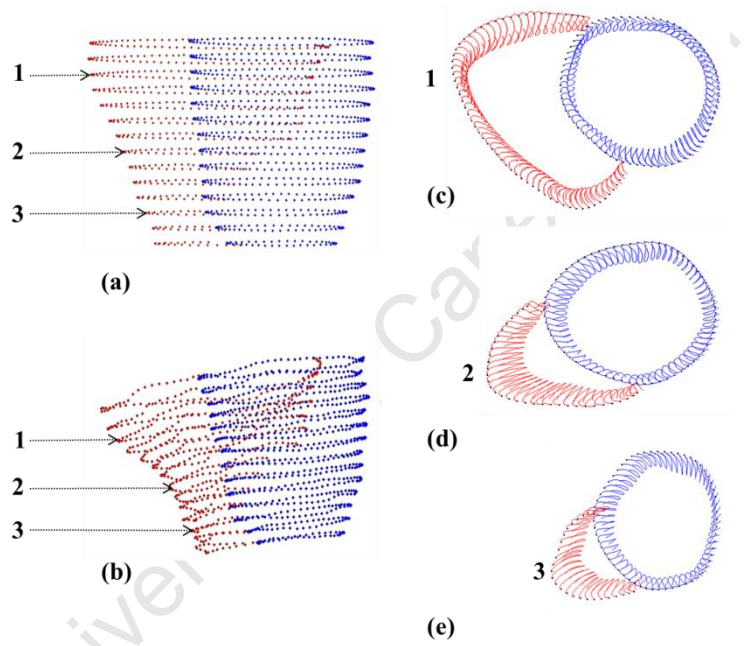

Figure 3.4: 3D mid-line motion trajectories. (a, b) show the RV (red) and LV (blue) positions during end diastole and end systole, respectively. (c, d and e) represent the motion trajectories for the respective myocardial slices 1,2 and 3.

The regional mean RV mid-wall strain-time curves for the five volunteers are plotted in Figures 3.5 and 3.6. Figure 3.5 shows the mean of the principal strains E2 and E3, while the 1D tangential circumferential and longitudinal strain are shown in Figure 3.6. The data are represented as mean ± one standard deviation. A summary of the maximum strain and the time to peak strain for each RV anatomical region is given in Table 3.1.

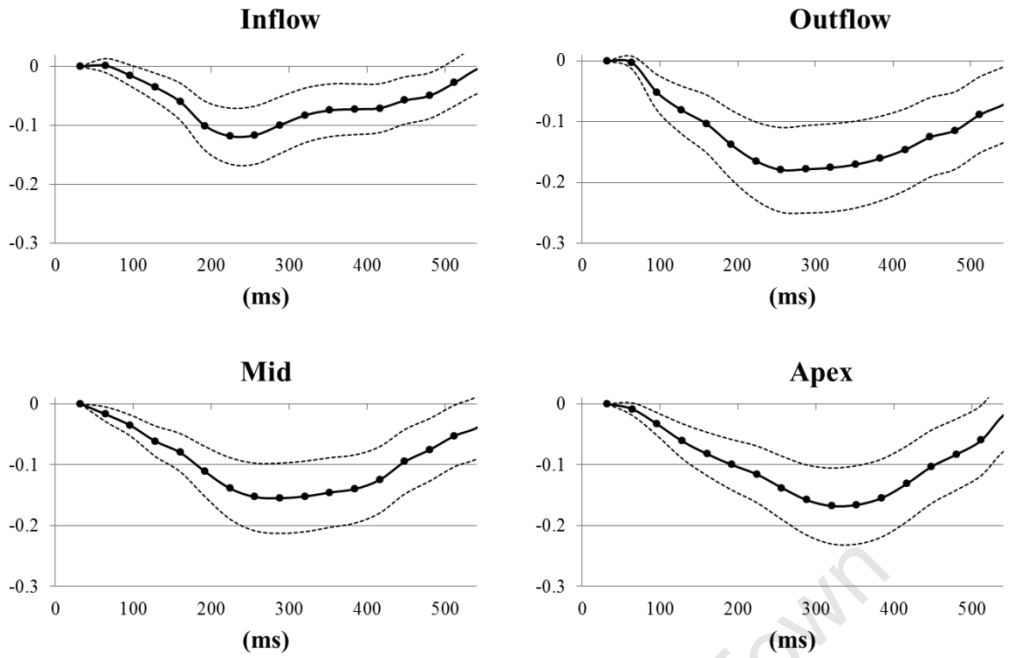

Figure 3.5: Mean principal 2D Lagrangian regional RV surface strain time curves for 5 normal volunteers. Data shown as strain vs. time (ms).

All strain values are consistently negative, indicating muscle shortening or contraction, and the longitudinal shortening is greater for all regions when compared to circumferential shortening.

The inflow region has the lowest peak strain value of all the regions, while the outflow region generally reaches the highest peak strain. However, Figure 3.6 illustrates that during tangential shortening in the circumferential direction, the apical region tends to have a slightly greater strain than the outflow region. Good consistency between the patterns of strain evolution is shown for the various strain estimates in Figures 3.5 and 3.6. The four regions each arrive at a maximum strain at slightly different time points in the cardiac cycle. The time sequence of regional myocardial shortening, as confirmed by all strain estimates is: inflow, outflow, mid then apical.

Table 3.1: Right ventricular regional Lagrangian strain and Time to peak

Strain quantification method and anatomical region	Maximum strain	Time to peak (ms)
1D Circumferential		
Inflow	-0.10 ± 0.04	224
Outflow	-0.15 ± 0.05	256
Apex	-0.17 ± 0.06	320
Mid Region	-0.16 ± 0.06	320
1D Longitudinal		
Inflow	-0.16 ± 0.06	256
Outflow	-0.22 ± 0.08	288
Apex	-0.20 ± 0.07	352
Mid Region	-0.18 ± 0.06	288
Mean principal strain		
Inflow	-0.12 ± 0.05	224
Outflow	-0.18 ± 0.07	256
Apex	-0.17 ± 0.06	320
Mid Region	-0.16 ± 0.05	288

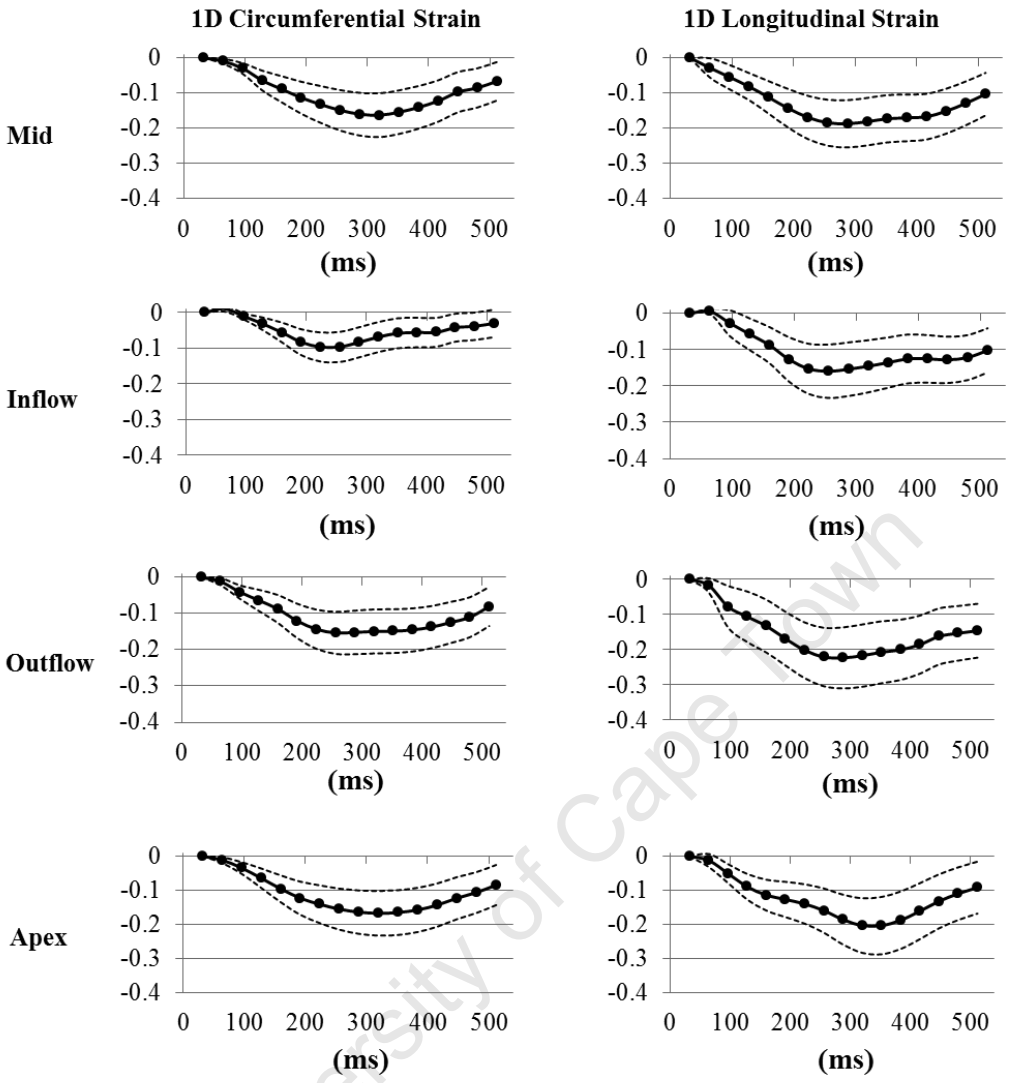

Figure 3.6: 1D Lagrangian regional RV surface strain time curves for 5 normal volunteers.

Figure 3.7 demonstrates 3D DENSE bi-ventricular mid-wall tissue tracking in two views for one volunteer during end diastole, mid systole and end systole, with the tracked points colour coded according the mean principal strain.

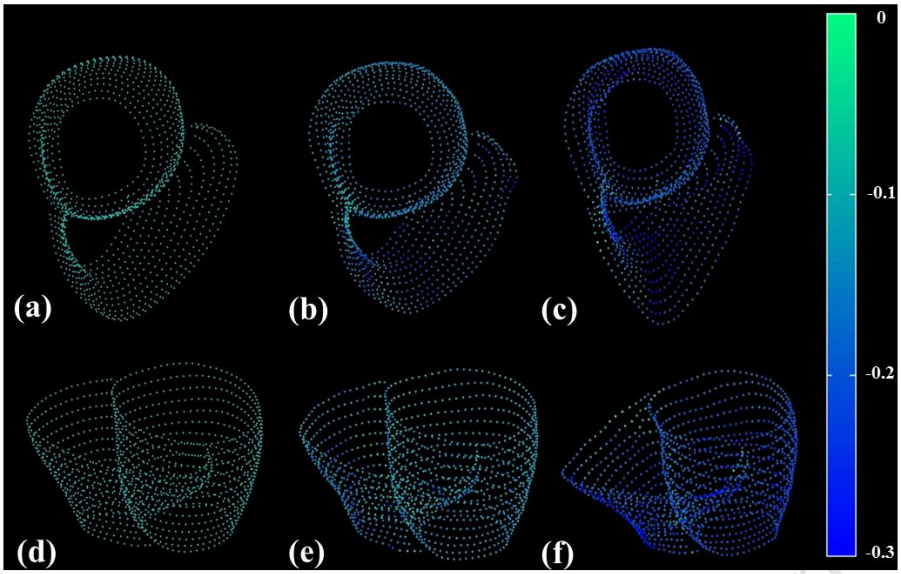

Figure 3.7: Tissue tracking and mid-wall strain. LV and RV mid-line images representing mean principal 2D Lagrangian surface strain in two views. (a, d) End diastole, (b, e) mid systole and (c, f) end systole. The dots represent the motion trajectory positions, while color represents mean principal strain.

3.4 Discussion

This paper introduces post processing algorithms developed for 3D tissue tracking and strain analysis of the RV from 3D cine DENSE data. Unlike previous studies of 3D RV motion using tagging [28, 30]; no models were used to describe the underlying data. Furthermore, no spatial smoothing was applied to the data, and the only form of filtering was the temporal polynomial fitting applied to the mid-line motion trajectories. This temporal fitting provides a more realistic trajectory behavior and allows for motion to be estimated at any temporal resolution.

Both the peak strain and the time-to-peak strain were found to vary in each RV region. The inflow region consistently demonstrated lower strains and early strain peak times, while the apex consistently showed larger strain values and later peak times. Some variation does exist in the outflow region when comparing the different strain calculation types.

As there is no current standard for dividing the RV, it is difficult to make a direct comparison with results from previous studies. In general, however, the magnitude of the strain measurements from this study compare favorably with previous RV studies

using myocardial tagging and SENC. From our study the peak mean principal strains values in the apical, mid and outflow regions are -0.17, -0.16 and -0.18, respectively. These values are similar to the corresponding values of -0.17, -0.19 and -0.22 reported in a tagging study by Haber et al. [28].

In the SENC study by Hamdan et al.[54], they show longitudinal strains to be largest at the base, with a lower strain at the apex, and the lowest strain in the mid region. For circumferential strain they show the largest strain at the apex, with a lower strain in the mid and basal regions. These regional strain comparisons show excellent agreement with those presented in Table 3.1. In our results, during longitudinal contraction, the largest strain is found in the outflow region (basal), followed by the apical and mid regions, while circumferential strain in the apical region is larger, followed by the mid and outflow (basal) regions.

The 1D peak longitudinal strains in Table 3.1 area all larger than the corresponding 1D peak circumferential and mean principal strains, a result confirmed in tagging studies by both Haber et al [28] and Fayad et al. [36]. Fayad et al., who used a very similar method to ours for sub-dividing the RV, found regional peak circumferential strains to range from largest to smallest in the following order: apical, mid, inflow and outflow. For peak longitudinal strains the corresponding order was: outflow, inflow, apical and mid regions. The peak strain values in Table 3.1 also correlate well with the segmental shortening presented by Fayad et al., except for the inflow region where our values are consistently lower.

Limitations of this study include a lengthy scan time, the need for manual contouring, and the difficulty to discern between the minimum and intermediate principal strains. A reduction in the scan time could be accomplished by incorporating parallel imaging and/or outer volume suppression. The time taken to contour the images may be considerably reduced with the extension of previous work on motion guided segmentation for 2D cine DENSE images [47]. Even with the use of the eigenvectors, discerning between the two principal strains was not possible. A geometric or finite element model of the RV could solve this problem, whereby the equivalent of an RLC coordinate system for the LV is defined according to the RV geometry.

The 2D surface strain estimates are expected to have a lower accuracy in the through plane direction because the through plane image resolution is lower than the resolution. This should lead to a less accurate representation of strain in the longitudinal direction compared to the circumferential direction, but this is not evident in the standard deviation curves in Figure 3.6.

An inherent limitation of DENSE is the reduction in SNR associated with the stimulated echo. The SNR was typically sufficient to clearly identify the RV because of the short echo times associated with the spiral readout. However, signal loss due to through plane dephasing is particularly pronounced in the RV because of its large through plane strain [27]. This reduction in SNR was evident in a few instances, and these data had to be excluded from the analyses. For future work on the RV, this through plane dephasing could be minimized by lowering the displacement encoding frequency, but at the expense of displacement sensitivity.

3.5 Conclusions

Three dimensional cine DENSE is a promising technique for assessing RV mechanics. The methods presented here enable the motion and deformation of the entire RV to be captured at a pixel resolution. The RV strain measured by 3D cine DENSE is comparable to that of previous studies using tagging and SENC.

We further describe a method for dividing RV into regions according to anatomical land marks. The measured temporal strain evolution in the proposed RV anatomical sub-divisions indicates that these regions may also be functionally distinct. Future work will involve applying these techniques to studying variations in regional RV function in various types of cardiac disease.

3.6 Acknowledgements

The authors would like to thank Aaron Hess, Ph.D. for the helpful discussions regarding the surface strain algorithm, and Professor Leon Axel M.D., Ph.D. for his valuable and insightful recommendations on the RV regional anatomical divisions. The authors further appreciate the clinical input from Dr. Bongani Mayosi M.D.

Chapter 4

Semi-automated Left Ventricular Segmentation Based on a Guide Point Model Approach for 3D cine DENSE MRI

DA. Auger, X. Zhong, FH. Epstein, EM. Meintjes, and BS Spottiswoode

Abstract

The most time consuming and limiting step in three dimensional (3D) cine displacement encoding with stimulated echoes (DENSE) MR image analysis is the demarcation of the left ventricle (LV) from its surrounding anatomical structures. The aim of this study is to implement a semi-automated segmentation algorithm for 3D cine DENSE MRI using a guide point model approach. Whole heart 3D cine DENSE data were acquired from four healthy volunteers. A 3D mathematical model is fitted to guide points which were interactively placed along the LV borders at a single time frame. An algorithm is presented to robustly propagate LV epicardial and endocardial surfaces of the model using the displacement information encoded in the phase images of DENSE data. The resulting LV contours are compared to manually delineated contours. The segmentation algorithm offers a 10-fold reduction in the time required to identify LV epicardial and endocardial borders for a single 3D DENSE data set. The model-defined contours display a good correlation when compared to the corresponding manually defined contours. This is based on a measure of segmentation error on intra- and inter-observer spatial overlap variability. Mass and volume calculations at end diastole and end systole demonstrate good correlation between manual and model methods, showing no significant difference. Functional LV parameter results compare favorably, while similarity coefficients show a good reproducibility and accuracy when comparing the algorithm defined contours to manually defined contours. This is a significant step towards the automation of the 3D cine DENSE data analysis.

Key Words: Cardiac MRI, DENSE, segmentation, guide point modeling

4.1 Introduction

Cardiac magnetic resonance (CMR) imaging techniques provide accurate and reproducible quantitative measurements of cardiac functional parameters for the diagnosis and treatment of cardiovascular disease. Techniques include balanced steady state free precession (SSFP) for morphological cine imaging [58, 59], myocardial tagging for intra-myocardial strain analysis [10, 60] and phase contrast velocity encoding for tissue velocity and strain rate imaging [17, 61]. Each technique plays a vital role in quantifying myocardial function, however, each consists of inherent limitations. Myocardial tagging has relatively low spatial resolution for the resultant strain maps, and the image analysis of tagging data is time consuming. PC velocity encoding suffers from errors accumulated across cardiac phases, and complicated tracking and integral algorithms have to be applied to correct these errors to calculate strain rate. Both MR imaging modalities suffer from low blood-myocardium image contrast. Balanced SSFP is an imaging technique that consists of high signal efficiency and is characterized by a strong blood-myocardium contrast. SSFP is used to quantify global parameters such as ejection fraction and mass, however, SSFP endures off resonance effects. A commonality between all techniques lies in the essential step of demarcating the left ventricle (LV) from surrounding structures during CMR image analysis. However, the anatomical nature of the heart and limitations in MRI techniques can make it difficult to distinguish LV boundaries. Extensive research has been dedicated to formulating various semi-automated and automated methods for segmenting the myocardium in MR images. In myocardial tagging, segmentation methods include deformable models [42, 43] and a combinations of active contours and region based segmentation techniques [45]. Guttman et al. used a dynamic programming method based on a minimum cost algorithm [62], while Alatter et al. incorporated a region growing algorithm [63]. A model based approach is often used in the analysis of LV function and segmentation. Montillo et al. and Young et al. described fully automated and semi-automated segmentation methods [46, 64], respectively, using an LV finite element model. In PC velocity encoding MRI, active contour models and the velocity phase data are used to distinguish between myocardium and blood [40]. Kainmüller et al. introduced a method that uses edge detection, curvature, flow and prior shape information [65].

SSFP segmentation techniques mostly incorporate image processing methods, which include thresholding, edge detection, mathematical morphology, and image filtering [66]. Prior geometric and spatiotemporal information methods are described in [67, 68].

Displacement encoding with stimulated echoes (DENSE) is an MRI technique well suited to quantifying regional functional parameters of the heart. This dark blood imaging technique provides regional myocardial displacement and strain measurements. The tissue displacement is encoded directly into the phase of the stimulated echo (typically with reference to end diastole), allowing for the extraction of motion and strain data at a pixel resolution [2, 3]. DENSE benefits from the advantages of both myocardial tagging and PC velocity encoding, and is capable of measuring large displacements over reasonable periods of time at a high spatial resolution. A free-breathing navigator-gated 3D spiral cine DENSE sequence has been developed to quantify tissue motion and strain within the entire LV in a single scan [4]. Like the other methods, DENSE ventricular analysis requires LV myocardial segmentation from surrounding structures. However, there are fewer LV segmentation algorithms for DENSE data analysis. Spottiswoode et el. presented a 2D semi-automatic segmentation algorithm guided by the phase information inherent in the DENSE data [47]. Chen et al. further described a method to segment myocardial contours using image intensity standardization and model evolution techniques [48]. However, to date, the segmentation processes in most reported studies were usually performed manually by an experienced user [4, 33]. A 3D cine DENSE data set typically comprises over 600 epicardial and endocardial LV contours, which would take an experienced user between 1 and 2 hours to demarcate. The clinical implementation of this technique is therefore limited by this necessary but prohibitively time consuming step.

The purpose of this study was to develop a tailored semi-automated segmentation algorithm for 3D cine DENSE MRI. This algorithm is largely based on the DENSE phase images, allowing 3D tissue tracking methods and an LV finite element model to drive the segmentation across the cardiac cycle.

4.2 Materials and Methods

4.2.1 Data acquisition

3D cine DENSE data of the whole heart was acquired for four healthy male volunteers (age range 21 – 45) on a 1.5T MRI scanner (Siemens MAGNETOM Avanto, Erlangen, Germany) using a six channel phased-array radio frequency (RF) coil. The entire heart was imaged in short axis slices at a 2.8 × 2.8 × 10 mm^3 spatial resolution and 32 ms temporal resolution. Fourteen 3D partitions were acquired. Displacement was encoded in three orthogonal directions. Images were acquired during a 20.5 ± 5.7 min scan with prospective ECG cardiac gating and diaphragmatic navigator respiratory gating. Other imaging parameters include: field of view = 360 × 360 × 140 mm^3, displacement encoding frequency k_e = 0.06 cycles/mm, ramped flip angle up to 20 degrees, TR = 16 ms, TE = 1.3 ms. Zero-padding was used during image reconstruction to increase the 14 acquired 3D partitions to 28 partitions, reducing the through plane resolution to 5mm. A spiral readout was used with 6 spatial interleaves per partition. All imaging was conducted with informed consent and IRB approval.

4.2.2 Image analysis

Each step in the segmentation algorithm is described below, while a summary of the algorithm is shown in Figure 4.1. All software development was performed using MATLAB (The Mathworks, Natick, MA). All computation was completed on an Intel(R) Core(TM) i3 CPU, at 2.27 GHz with 4GB of RAM.

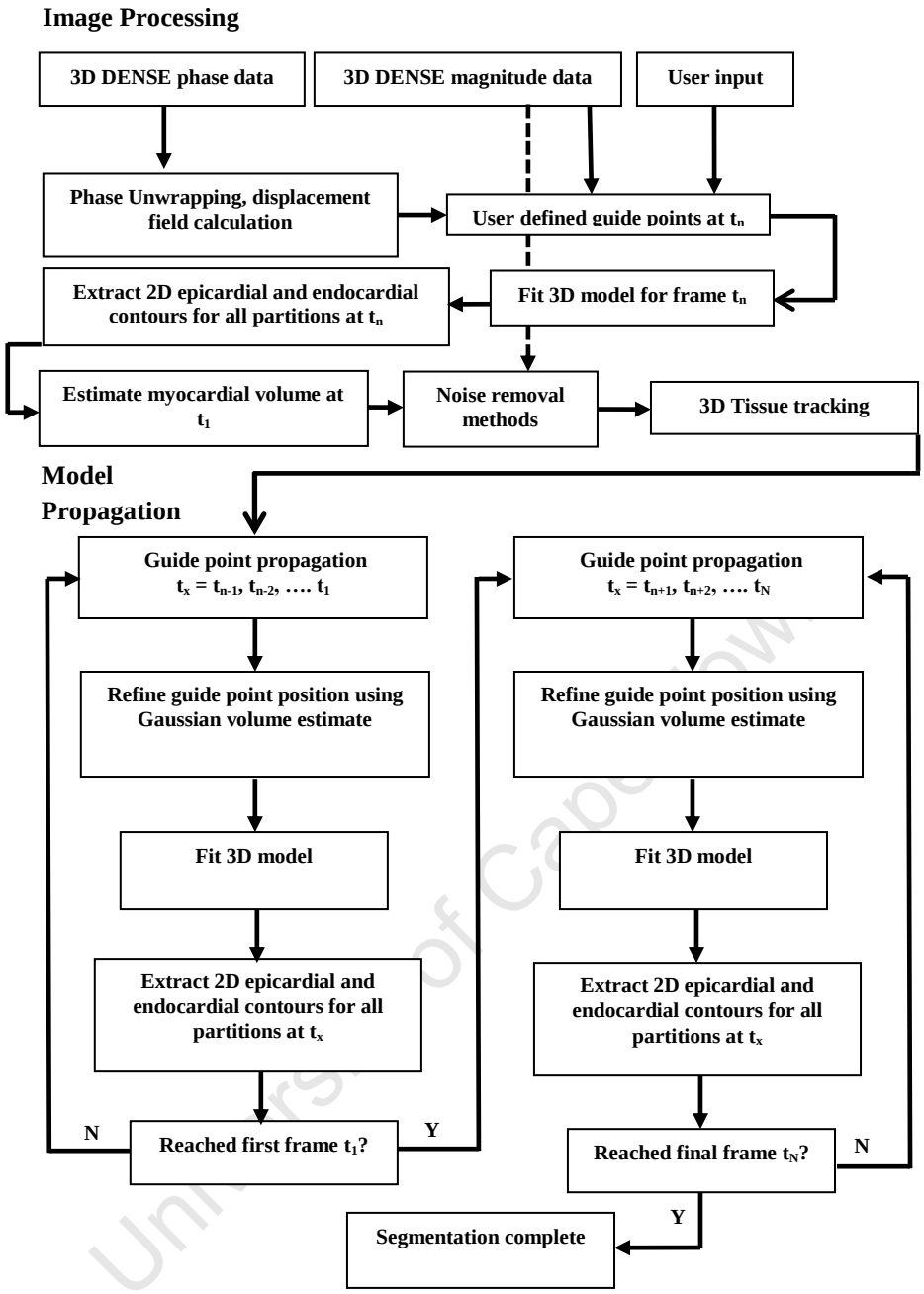

Figure 4.1: Image processing and model propagation. Flow diagram shows each step from image processing, definition of guide points, and model propagation through the cardiac cycle, required for the segmentation algorithm.

4.2.2.1 Phase unwrapping and estimation of displacement fields

Spatio-temporal phase unwrapping [27] was performed in order to remove phase aliasing and acquire the absolute displacement measurements. The phase data from each of the three encoding directions were combined to create 3D Eulerian displacement fields. Figure 4.2 illustrates un-contoured cine DENSE magnitude and

unwrapped phase images in three orthogonal directions, with the corresponding 3D displacement field (view from above) for a single short-axis slice. The LV displacement vectors are evident as continuity in the image, illustrating the contracting motion of the LV, as the displacement vectors are pointing towards the center of the LV. In contrast, displacement vectors describing the surrounding tissue such as the liver are coherent in a single direction, while the lungs and blood are represented by randomly scaled and oriented vectors.

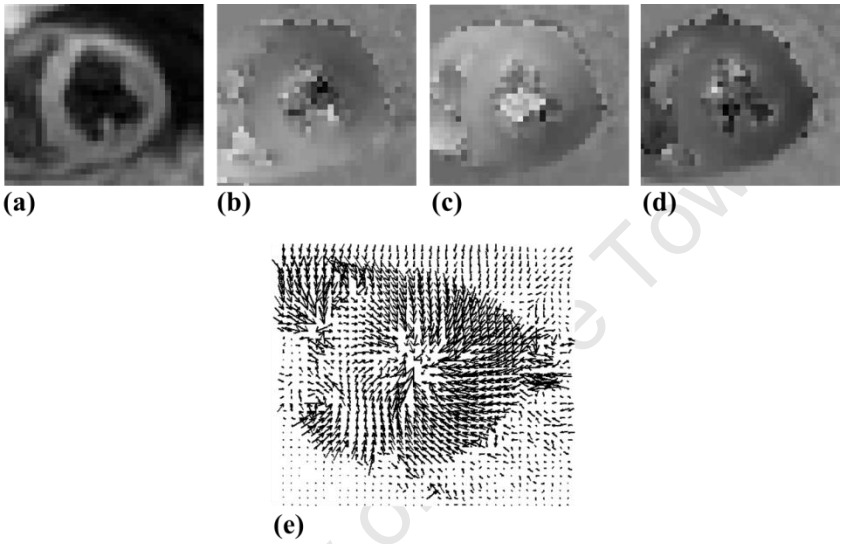

Figure 4.2: A single short axis slice of the 3D cine DENSE data during systole. (a) DENSE magnitude image, (b, c, d) DENSE phase images after applying spatiotemporal phase unwrapping without predefined contours, encoded for motion in the x, y and z directions, respectively. (e) Corresponding 3D DENSE displacement field derived (view from above).

4.2.2.2 Initializing epicardial and endocardial surfaces

A 3D finite element model of the LV was employed to create each epicardial and endocardial surface separately [69, 70]. Each surface is manually initialized at a single time point by defining 3 sets of coordinates. First, the user defines points along the corresponding border at the most apical and the most basal slice. The last coordinate required corresponds to the position of the mid LV – mid septum. The surface is then defined by interactively placing guide points along the respective boundary in a Cartesian coordinate system. This is done on the DENSE magnitude images of all the slices at any single cardiac time point (t_n) where the LV myocardium is easily distinguishable from the surrounding structures. Each 3D surface point is transformed into a prolate spheroidal coordinate system as described in [69]. Prolate spheroidal

coordinates provide a convenient representation of the LV geometry, and further facilitate surface calculations in a deforming LV. Figure 4.3 illustrates the user defined guide points placed at three different short axis slices (apical, mid and basal) at each LV boundary during a systolic cardiac time frame. During initialization, each surface consists of a number of parameters which can affect the accuracy of the model. These parameters include the number of user defined guide points, the magnitude of the smoothing weight constraints, and the model mesh size which is dependent on the number of elements. In this work, we define a set of initial model parameters using 8 guide points to define each surface, yielding an ellipsoidal mesh composed of 32 bicubic Hermite elements (4 circumferential and 8 longitudinal). Each surface was defined at an early systolic time frame (t_n), with smoothing weights α and β consisting of values of 0.1×10^{-1} and 0.2×10^{-1} respectively. The ratio of the smoothing weights (α/β) penalizing bending and stretching of the fitted surface, is maintained at 0.5 [69, 70]. Hashima et al. describes the implementation of weight constraints and its effects [70].

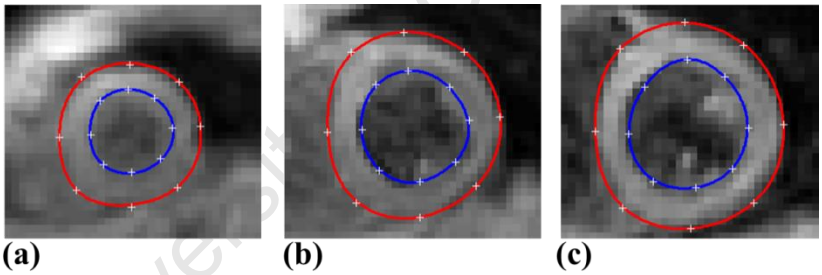

Figure 4.3: 3D DENSE magnitude images at (a) apex, (b) mid LV and (c) base. Each image shows 8 spatially placed user defined guide points (+) at the epicardial and endocardial boundaries, with the corresponding LV model defined epicardial (red) and endocardial (blue) contours.

The model describes the complete 3D LV epicardial and endocardial surface at the cardiac frame, t_n. Each surface is then sampled at the z-coordinate corresponding to the data slice in order to extract a set of initial 2D contours.

4.2.2.3 Noise removal and tissue tracking

In DENSE, the displacement vectors at all-time points in the cardiac cycle will reference the material position of the myocardium at the time of encoding. This inherent property of DENSE, allows for the myocardium enclosed in the first set of

contours derived from the user defined guide points, to be estimated at the first time frame (t_1), where tissue tracking is initiated. Obtaining suitable motion trajectories from noisy displacement vector fields requires tissue tracking refining steps where unwanted vectors are excluded from tissue tracking.

A spatial derivative function and a low signal-to-noise (SNR) filtering step were implemented in order to remove the effects of noisy vectors from the lungs and blood pools, and include vectors only corresponding to the LV myocardium in the tissue tracking methods. These two filters are implemented as follows:

Combining the orthogonal spatial derivatives of the displacement fields at each cardiac time point creates a modulus deformation mask [47]. A threshold of 80% is used to exclude noisy vectors. This limit is well above myocardial deformation values found in the healthy LV [12]. The spatial derivative for a single time point (t_n) is given by Equation 1.

$$S(X,t_n) = \frac{1}{2}\sum_{k=\hat{\imath},\hat{\jmath},\hat{k}}\left[\left(\frac{\partial u_k(X,t_n)}{\partial \hat{\imath}}\right)^2 + \left(\frac{\partial u_k(X,t_n)}{\partial \hat{\jmath}}\right)^2 + \left(\frac{\partial u_k(X,t_n)}{\partial \hat{k}}\right)^2\right]^{\frac{1}{2}} \tag{4.1}$$

where X represents the spatial position in the image plane, $u_{\hat{\imath}}$, $u_{\hat{\jmath}}$ and $u_{\hat{k}}$ represent the displacement vector components in the three orthogonal directions, $\hat{\imath}$, $\hat{\jmath}$, and $\hat{k}$, respectively.

An SNR filter is implemented in order to remove low SNR voxels surrounding the LV. The filter is based on the myocardial image intensity and the background noise. A region of background noise is identified by the user, and the myocardium intensity is defined by the tissue enclosed within first set of contours initiated at time t_n at each slice, for all slices. The mean and standard deviation of the enclosed myocardium is calculated and voxels below two standard deviations are excluded.

The modulus deformation mask is applied prior to tracking where the majority of unwanted vectors are removed. The SNR filter is then applied to further exclude any further noise surrounding the LV.

Previous DENSE tracking algorithms describe the interpolation of vector displacement fields for tissue tracking through the cardiac cycle [27, 33]. This work implements a similar tracking algorithm, where the position of each tissue tracking point along its motion trajectory was estimated using 3D distance weighted linear interpolation, using the entire 3D displacement vector volume. Trajectories are further improved by applying temporal fitting for each ordinate direction of each of the trajectories using a 10^{th} order polynomial [4].

Using 3D motion trajectories, each user defined guide point can be propagated to successive cardiac frames. The time direction in which this is done is irrelevant.

4.2.2.4 Guide point propagation

The position of the guide points at all time frames in the cardiac cycle can be estimated using the closest myocardial motion trajectory to each guide point. A refinement step is necessary to ensure that the guide point position accurately coincides with the border of the myocardium. This is achieved using a separate series of images, which are created by representing each trajectory position at each frame by a 3D Gaussian function with an integrated intensity of unity. The contribution from all tracked points is added to create a combined Gaussian image at each time frame. As each guide point is propagated across the cardiac cycle, its position is refined by moving the point along the intensity gradient of the combined Gaussian image towards the endocardial / epicardial boundary until a value of 0.5 is reached. A Gaussian standard deviation of 1.25 was used for the in plane x and y directions, while a standard deviation of 1.5 was used in the z direction allowing for an ellipsoidal distribution. This was found suitable as the slice thickness dimension is greater than the in plane resolution. If the standard deviation is set too low, there is a pixelated effect in the Gaussian image where the distribution is unequal, while if the standard deviation is set too high the distribution is expanded and the LV dimensions are shown to be much larger, similar to the effect described in [47].

4.2.2.5 Experimental validation

In order to quantify the voxel-based accuracy of the segmentation results, all four 3D data sets were manually contoured by a single experienced user. LV mass, end

diastolic volume (EDV) and end systolic (ESV) volume were calculated from both user defined and semi-automated contours using Simpson's rule [71]. The LV stroke volume (SV) and ejection fraction (EF) were calculated as SV = EDV – ESV, and EF = (SV / EDV) × 100, respectively. The LV mass was calculated by LV_{mass} = 1.05 × (epicardial volume – endocardial volume). The papillary muscles were excluded from both mass and volume calculations. The semi-automatic segmentation was completed for all four data sets using the above model parameters that were chosen based on visual assessment of accuracy. The following model parameters were then individually varied in order to determine the optimal parameters and how each can have an effect on the segmentation results: (1) the model was initialized during a late systolic time frame, as oppose to an early systolic time frame, (2) four user defined guide points defined each surface, as appose to the initial eight, (3) the smooth weight constraints α and β were decreased from 0.1×10^{-1} and 0.2×10^{-1} to 0.1×10^{-3} and 0.2×10^{-3}, respectively and (4) the model mesh size was adjusted from 32 to 64 elements. A paired Student's t-test and one-way analysis of variance (ANOVA) were used to assess statistical significance of volume and mass results; $p < 0.05$ was considered to indicate a statistical significant difference.

In order to quantify the reproducibility and accuracy of the 2D contour geometry, three slices (apical, mid and basal) at end diastole and end systole were manually contoured by 2 separate operators (Operator A and Operator B). The corresponding semi-automated contours were validated against these manual contours by comparing the percentage of overlapping and discrepant voxels. This was done by calculating mean and union overlaps (Dice and Jaccard metrics) [72], as well as false positive and false negative errors. The Dice and Jaccard metrics represent the reproducibility and accuracy, respectively, based on the spatial overlap of the manual and semi-automated contours. A value of zero indicates no spatial overlap, while a value of 1 indicates complete perfect overlap. The Dice (D) and Jaccard (J) coefficients are calculated by $D = 2((S_r \cap T_r) / S_r + T_r)$ and $J = ((S_r \cap T_r) / S_r \cup T_r)$, respectively. Here, S_r is the region on the source image enclosed by the manual contour and T_r is the region on the target image enclosed by the semi-automated contour. ∩ and ∪ denote intersection and union, respectively. The false positive measure indicates the percentage of tissue that is falsely identified as myocardium, while the false negative measure indicates the

percentage of myocardium missed by the algorithm. The false negative error is given by $(T_r - (S_r \cap T_r)) / S_r$ and the false positive error is given by $(S_r - (S_r \cap T_r)) / S_r$.

4.3 Results

The complete semi-automated segmentation process takes approximately 8-15 minutes per subject. The time is divided between the manual guide point placement (~5 minutes) and the computation time (~10 minutes). Figure 4.4(a, b) illustrates examples of epicardial and endocardial generated surfaces, where (a) represents a case where both surfaces were at an end diastolic time frame, and (b) represents a case where both surfaces were at end systole.

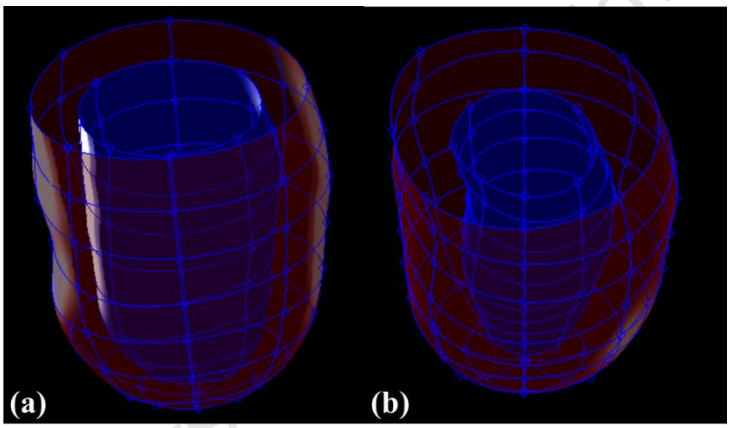

Figure 4.4: Three dimensional LV model epicardial (red) and endocardial (blue) surface as a result of user defined guide points. Surface shown during, (a) end diastole, and (b) end systole.

Figure 4.5 illustrates, for a selected short axis slice, the effects of the noise removal techniques used to discard unwanted displacement vectors. These images show how each step removes randomly oriented and scaled vectors, while the vectors describing myocardium remain.

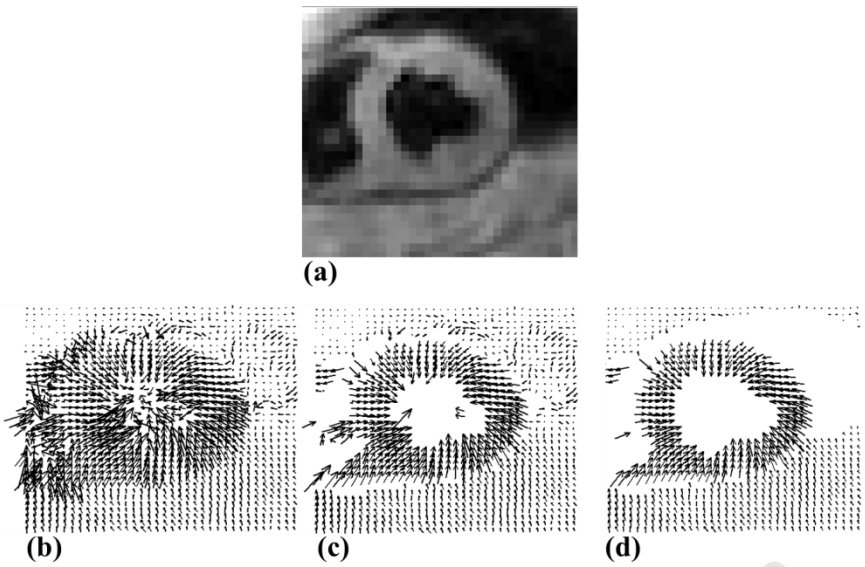

Figure 4.5: (a) LV-mid DENSE magnitude image during end systole, (b) corresponding vector displacement field without pre-defined contours, (c) vector displacement field after applying modulus deformation mask, showing removal of randomly orientated vectors predominantly in the blood pool, (d) vector displacement field after applying the SNR filter, further removing noisy vectors. Vectors incorporated in 3D tissue tracking.

Figure 4.6 illustrates contoured data of a mid ventricular slice during end systole for varying model parameters: (a) *corresponds to initializing the model during end systole*, 8 guide points per slice, model mesh size of 32 elements and smoothing weight factor of $\alpha = 0.1\times10^{-1}$ and $\beta = 0.2\times10^{-1}$, (b) corresponds to initializing the model during early systole, *4 guide points per slice*, model mesh size of 32 elements and smoothing weight factor of $\alpha = 0.1\times10^{-1}$ and $\beta = 0.2\times10^{-1}$, (c) corresponds to initializing the model during early systole, 8 guide points per slice, *model mesh size of 64 elements* and smoothing weight factor of $\alpha = 0.1\times10^{-1}$ and $\beta = 0.2\times10^{-1}$ and (d) corresponds to initializing the model during early systole, 8 guide points per slice, model mesh size of 32 elements and *reduced smoothing weight factors* of $\alpha = 0.1\times10^{-3}$ and $\beta = 0.2\times10^{-3}$.

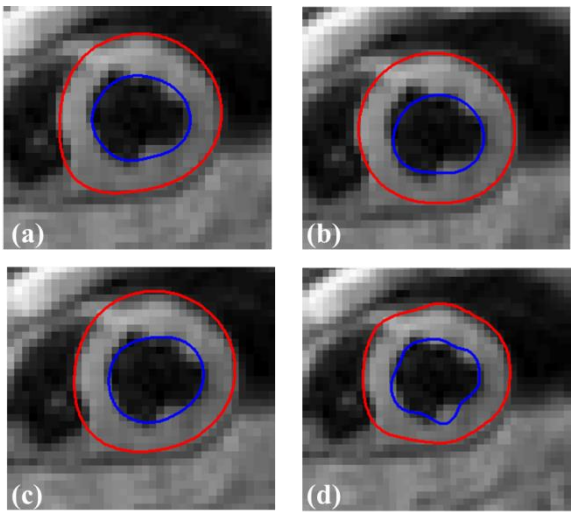

Figure 4.6: Segmentation results during end systole. Each image represents the results after varying an individual model parameter. (a) Initialization of model during end systole as oppose to early systole, (b) decreased user guide points from 8 to 4 per short axis slice, (c) model mesh size is increased from 32 to 64 elements and (d) smoothing weight factors reduced from $\alpha = 0.1\times10\text{-}^{1}$ to $0.1\times10\text{-}^{3}$ and $\beta = 0.2\times10\text{-}^{1}$ to $0.2\times10\text{-}^{3}$.

The EDV, ESV, SV, EF and mass values obtained in the volunteers for both manual and semi-automated contours are presented in Table 4.1. Table 4.1 also includes mass and volume results using the contours derived after varying model parameters. The data are presented as mean ± one standard deviation. Table 4.2 presents statistical analysis results from the student t-test and one-way ANOVA. The student t-test shows no statistical significance ($p < 0.05$) results between the manually drawn contours and the model derived contours with the chosen initial parameters. The ANOVA analysis compares the statistical variation between contours defined manually, contours according to chosen model parameters, and contours produced by a model with variations in the parameters. There is no statistical significance between each method. A summary of the Dice and Jaccard spatial overlap, false positive and false negative results between two observers and the model is given in Table 4.3. Table 4.4 shows the overlap correlation results between a single observer and the model, given individual parameter variations.

Table 4.1: Volume and mass calculations for operator defined contours, model contours with initial selected model parameters, and contours after varying individual model parameters. The initial model parameters consist of: 8 user defined guide points, 32 element model defined at early systole, with smoothing constraints of $\alpha = 0.1\times10\text{-}1$ and $\beta = 0.2\times10\text{-}1$.

Measure	Operator A	Initial model parameters	Individual model parameter variation			
			4 Guide points	64 Model elements	Late-systolic initialization	$\alpha = 0.1\times10^{-3}$ $\beta = 0,2\times10^{-3}$
EDV (ml)	130.0±15.4	121.1±22.2	109.5±17.2	114.9±12.9	116.3±12.7	113.2±10.4
ESV (ml)	58.4±10.2	57.7±9.2	53.9±6.5	58.3±5.8	54.9±7.2	61.1±2.8
EF (%)	56.45±5.7	52.2±1.9	50.5±4.7	49.0±5.0	52.8±3.5	51.6±6.0
SV	73.0±7.4	63.4±13.3	55.6±12.6	56.54±10.8	61.4±7.6	52.1±9.0
Mass (g) (*Diastole)*	139.1±7.9	145.6±13.8	141.8±9.8	148.0±16.0	140.6±6.4	148.0±19.0
Mass (g) (*Systole)*	146.5±6.2	146.7±9.5	140.1±24.0	138.5±18.3	141.2±13.9	143.9±19.7

Table 4.2: Student T-test and ANOVA statistical variation test for mass and volume results in Table 4.1 ($P < 0.05$). Table shows corresponding t-values with corresponding p-values, and F-values with corresponding p-values.

Measure	T-Test [a*]		Individual model parameter variation. ANOVA(df = 2,9) [b*]							
			4 Guide Points		64 Element model		Late-systolic initialization		$\alpha = 0.1\times10^{-3}$ $\beta = 0.2\times10^{-3}$	
	t	p	F	p	F	p	F	p	F	p
EDV (ml)	0.66	0.54	1.24	0.34	0.77	0.49	0.65	0.55	1.02	0.40
ESV (ml)	0.10	0.92	0.31	0.74	0.01	0.99	0.85	0.85	0.19	0.83
EF (%)	1.42	0.24	1.97	0.20	2.73	0.12	1.32	0.31	1.16	0.36
SV	1.27	0.26	2.33	0.15	2.35	0.15	1.60	0.25	4.18	0.05
Mass (g) (*Diastole)*	0.82	0.45	0.37	0.70	0.51	0.62	0.48	0.64	0.41	0.67
Mass (g) (*Systole)*	0.03	0.97	0.24	0.79	0.56	0.59	0.36	0.71	0.05	0.95

[a*] = T-test, manual contours versus initial model parameters, $p < 0.05$
[b*] = ANOVA, manual contours, initial model parameters and varying a single parameter at a time, $p < 0.05$

Table 4.3: Spatial overlap results between contours defined by 2 separate operators (A and B) and the model derived contours. The model here used the initially defined parameters.

Measure	Operator A vs. Model			Operator B vs. Model			Operator A vs. B		
	Apex	*Mid*	*Base*	*Apex*	*Mid*	*Base*	*Apex*	*Mid*	*Base*
Dice Coefficient	0.85± 0.06	0.87± 0.04	0.88± 0.02	0.86± 0.02	0.89± 0.03	0.85± 0.03	0.88± 0.04	0.88± 0.02	0.92± 0.03
Jaccard Coefficient	0.75± 0.09	0.77± 0.06	0.78± 0.03	0.76± 0.02	0.80± 0.04	0.73± 0.05	0.79± 0.06	0.78± 0.04	0.86± 0.05
False positive	0.09± 0.1	0.11± 0.02	0.08± 0.07	0.06± 0.04	0.09± 0.03	0.1± 0.08	0.16± 0.07	0.12± 0.06	0.03± 0.04
False negative	0.19± 0.06	0.14± 0.06	0.16± 0.08	0.19± 0.02	0.13± 0.06	0.19± 0.08	0.09± 0.02	0.13± 0.06	0.11± 0.04

Table 4.4: Contour overlap validation between a single operator and geometrical model with individual parameter variation.

	4 Guide points			**64 Model elements**			**Late systolic initialization**			**$\alpha = 0.1\times10^{-3}$ $\beta = 0{,}2\times10^{-3}$**		
	Apex	*Mid*	*Base*	*Apex*	*Mid*	*Base*	*Apex*	*Mid*	*Base*	*Apex*	*Mid*	*Base*
Dice Coefficient	0.85± 0.03	0.86± 0.04	0.86± 0.05	0.80± 0.14	0.85± 0.03	0.85± 0.08	0.89± 0.03	0.92± 0.87	0.87± 0.15	0.81± 0.03	0.88± 0.01	0.86± 0.03
Jaccard Coefficient	0.74± 0.04	0.76± 0.07	0.76± 0.08	0.68± 0.17	0.73± 0.05	0.75± 0.11	0.81± 0.05	0.85± 0.02	0.79± 0.21	0.68± 0.04	0.78± 0.02	0.76± 0.05
False positive	0.05± 0.04	0.07± 0.04	0.06± 0.03	0.08± 0.01	0.09± 0.05	0.05± 0.03	0.03± 0.03	0.08± 0.02	0.04± 0.02	0.04± 0.04	0.10± 0.08	0.08± 0.02
False negative	0.22± 0.05	0.18± 0.10	0.19± 0.09	0.26± 0.19	0.19± 0.09	0.21± 0.10	0.17± 0.06	0.08± 0.03	0.18± 0.21	0.28± 0.06	0.14± 0.07	0.18± 0.06

Figure 4.7 (a-i) illustrate the segmentation results during three stages of the cardiac cycle, at an apical, mid and basal slice. The results are based on the initial chosen model parameters. Figure 4.7 (a, d and g) shows the algorithm's ability to enclose myocardium during end diastole, where it is visually difficult to discern between the myocardium and blood pool. Furthermore, all images show the accurate propagation of each surface across the cardiac cycle, by enclosing the LV myocardium and the three distinct time frames. Based on a visual analysis by an experienced user, only 125 out of a total of 2124 contours from all 4 data sets, or 5.6%, would require readjustment.

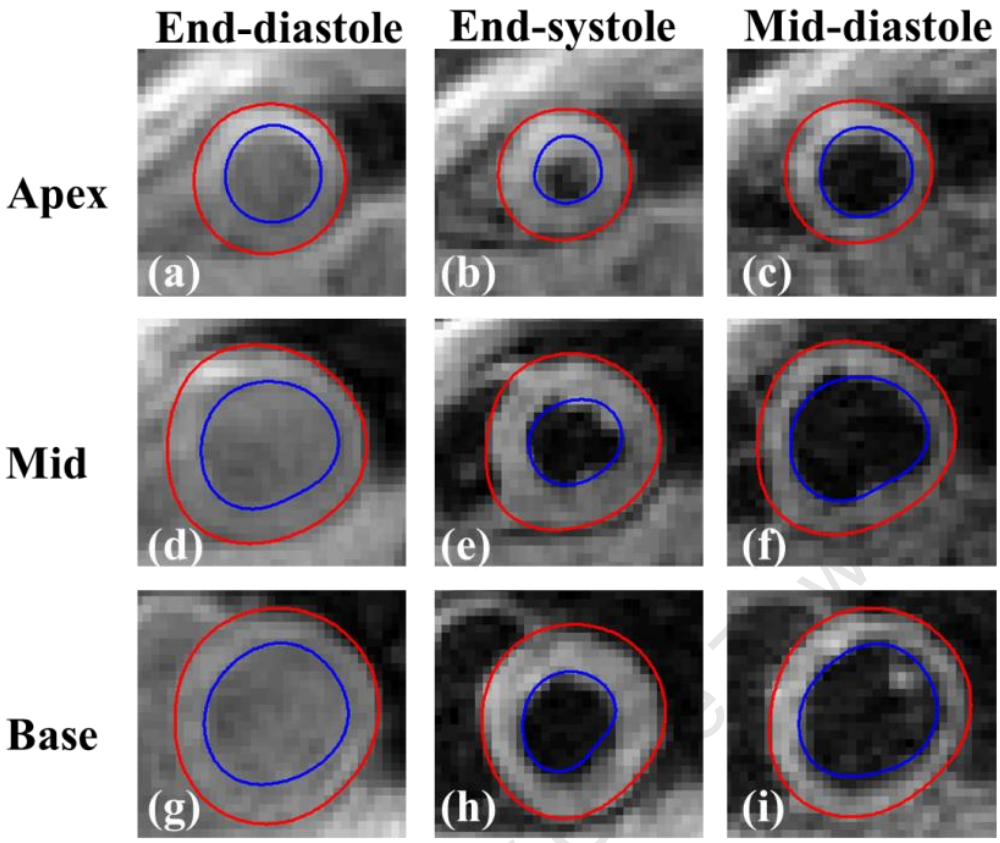

Figure 4.7: Segmentation results according to the initial LV model parameters chosen: 8 user defined guide points, 32 element model defined at early systole, with smoothing constraints of $\alpha = 0.1\times10\text{-}1$ and $\beta = 0.2\times10\text{-}1$.The results are shown at three separate cardiac time frames, at the LV apex, mid and base.

4.4 Discussion

This study presents a semi-automated LV segmentation algorithm for 3D cine DENSE MRI, using a guide point model approach. An LV finite element model has been used for segmentation with other 3D cardiac MRI studies [46, 73-75]. However, for previous work the model is typically manually initialized at each cardiac frame, whereas here the information inherent in the DENSE phase images provides the ability to propagate the model across the cardiac cycle. The use of guide points reduces the user interaction time to manually demarcate the LV. Furthermore, as the algorithm allows for the user to define guide points at any cardiac frame where the myocardium is clear and distinguishable, this reduces the risk of user input error. The model is sufficiently deformable to adhere to variations in LV shape, but smooth enough to correct for a degree of guide point misalignment.

The time required to manually contour an entire 3D DENSE data set for an experienced user is approximately 1-2 hours, whereas this semi-automated algorithm reduces the process to approximately 15 minutes. This time could be further reduced by altering model parameters such as the number of guide points used and the mesh size, but at the expense of segmentation accuracy. Computation time can also be improved by implementing the algorithm in a more efficient coding language (such as C++), and upgrading the computer hardware specifications.

As demonstrated by Figure 4.5, methods used to remove noisy vectors are shown to work appropriately, limiting the displacement fields predominantly to myocardial vectors. The spatial derivatives remove the majority of unwanted vectors by providing a deformation mask around the LV. As 3D spiral cine DENSE boasts a higher SNR than echo planar approaches [4] and a varying flip angle is used, an SNR threshold is appropriate to further remove unwanted vectors in the lungs and blood pools.
Tissue tracking using a full 3D volumetric displacement field at each frame, will improve the tracking accuracy in the LV compared to 2D DENSE

A number of CMR studies have reported on the normal ranges of LV mass and volume [46, 76-79], based on SSFP and gradient echo (GRE) cine imaging. Although the LV mass and volume calculations shown in Table 4.1 show a moderate agreement with the above studies, it is difficult to directly correlate volume and mass results. This may be attributed to the fact that this study only includes short axis data, while Alfakih et al., Hudsmith et al. and Maceira et al. all include long axis data in the analysis, thereby better incorporating the long axis movement of the basal parts of the LV [76, 78, 79]. In addition, according to Alfakih et al., age plays a vital role when determining normal LV physiological parameters. The age as well as the number of volunteers used in this study varies substantially when compared to the studies described above. However, the comparison between manual contours and the contours derived via the semi-automated algorithm is of greater relevance for this work.

Table 4.1 displays all mass and volume calculations using the manually drawn contours and all model defined contours. The model defined contour results are divided between the initial model parameters, and the varied model parameters. The

results show there is a good agreement between all contouring methods. The EDV for the manual contours is slightly higher. This can be attributed to an underestimation of the algorithm's endocardial contour towards the base of the LV, due to through plane motion not being accurately described by the relatively large slice thickness of the 3D DENSE data. However, the statistical analysis in Table 4.2 between these sets of results shows there is no significant difference between methods. In Table 4.2, the student t-test is performed to compare the hand drawn contours and the initial model parameter contours. The results show there is no significant difference between the two. Table 4.2 further displays one-way ANOVA results, between the manual contours and model contours with single parameter variation. The results show a good correlation between all contouring methods. This shows each model variation compared favorably to both manual contours and the initial contour model parameters. Each model variation comes with tradeoffs, which becomes apparent when looking at the spatial overlap results.

Table 4.3 shows the results of the spatial overlap results in the form of Dice and Jaccard coefficients, and false positive and false negative overlap results. The results were compared between the contours drawn by two separate Operators (A and B), and the initial model parameter derived contours. According to Zou et al. [72], Dice and Jaccard coefficient value of 0.7 and above, indicates a good spatial overlap. All Dice and Jaccard coefficient results shown are well above 0.7, except for two measurements, 0.68±0.17 and 0.68±0.04 using a 64 element model and half the smoothing factor respectively. Both results correspond to the LV apex, where the myocardial contrast is lower and is the area with the greatest curvature.

The highest Dice and Jaccard coefficient values were between Operator A and B, but the variations between each operator and the model were insignificant, implying a good spatial overlap agreement between manual contours from the two separate operators, and the model defined contours. A low false positive signifies a low percentage of tissue falsely identified as myocardium and a low false negative result signifies a low percentage of missed myocardium. Interestingly, the highest false positive values occurred between operator A and B, with values of 0.16 ± 0.07 and 0.12 ± 0.06 for the apex and mid LV respectively. This could be attributed to the

operators having inconsistent estimation of papillary muscles and the perimeter of the endocardium at the apex of the LV. Although the majority of the blood has been expelled, the contrast towards the LV apex is not always as clear as the contrast towards mid and basal slices. False negative results show higher values in the base and apex. At the apex, this could be attributed to the low LV contrast, while the propagation of guide points towards basal LV can produce underestimated epicardial contours due to the high displacement and motion at the base.

As each guide point governs the direction and shape of the surface, using fewer guide points can result in the underestimation of the LV curvature. This is shown by the slightly higher false negative results in Table 4.4 when using four guide points to initialize each surface. However, the overall spatial overlap results in Table 4.3 show good correlation between the operator and the model. Using 4 guide points placed symmetrically around the LV in order to reduce computation time and user interaction, is therefore a reasonable adjustment, showing good correlation between results.

Increasing the model mesh size will increase the computation time, and maintain a more uniform cylindrical surface. In Table 4.4, Dice and Jaccard coefficients show a good spatial overlap. The higher false negative value at the apex can be attributed to the model's uniform shape therefore over estimating the endocardial border. This will also contribute towards the high myocardial mass estimates.

The effect of initializing the segmentation process at late systole compared to early systole is summarized in Table 4.4, where a good spatial overlap, with low false positive values is seen. Slightly higher false negative values are found at the apex and base. The low LV contrast and through plane motion may account for these results, respectively. These results confirm that model initialization can be done at any time frame.

Significantly reducing the smoothing constraints in the model is shown to negatively affect the segmentation results. If a guide point is propagated incorrectly due to phase noise, the ability of the model to correct this misalignment is reduced. With reference

to Table 4.2, varying the smoothing had no significant effect on the SV, however, it does consist of the lowest p value of 0.05. A post-hoc test was carried out for the SV results, showing p = 0.01, when comparing the results with manually drawn contours and model contours with a reduced smoothing weight. A p-value of 0.22 is calculated between the hand drawn contours and the initial model contours with a higher smoothing weight. In order to maintain accurate contour results while lowering the smoothing constraints, one would have to increase the model mesh size and the number of user defined guide points.

The results show how decreasing the smoothing factor affects the results, however, it is important to note, that if the smoothing factor is significantly increased, the smoother model will not be able to describe as many variations in heart morphology.
The best model parameters to use in the segmentation based on accuracy, computation time and user required input are as follows; initialize the model at an early systolic frame using 8 guide points to define each surface, yielding an ellipsoidal mesh composed of 32 bicubic Hermite elements. Smoothing weights α and β of values of 0.1×10^{-1} and 0.2×10^{-1} respectively.

Although an underestimation of the segmentation algorithm may not be clear in averaged regional strain calculations, it is important to maintain accurate delineation of the myocardial boundaries when assessing diseased myocardium. Thus, the complexity of the algorithm is required in order to approximate segmentation results to that of a manually segmented data set.

There are a number of advantages to the semi-automatic segmentation method presented when compared to the current manual methods. The semi-automated technique offers minimal user interaction, a 10-fold reduction in total processing time, and reliable contouring at the first cardiac phase where it can be difficult to visually discern between blood and myocardium.

By visually reviewing the segmentation results among all four data sets, only 5.6% of contours required readjustment.

The method also consists of several limitations and potential sources for error; such as partial volume effects, phase unwrapping errors, and imperfect phase correction. The accuracy of the algorithm therefore fundamentally relies on correct displacement vector calculation, noisy displacement vector removal techniques and accurate tissue tracking. Towards the LV base, the thin myocardial walls, high longitudinal displacements and partial volume effects due to through plane dephasing can cause inaccurate displacement measurements, causing poor guide point propagation in these areas. The increase of the number of guide points can result in more accurate contours but at the expense of processing time and increased user interaction. However, by adjusting the model parameters accordingly, the work shows accurate segmentation results with good visual agreement. The model was conformed that good segmentation results could be achieved within the range of LV shapes encountered in this study.

This work has only been tested on four data sets and future work can be used to validate the method using an increased number of healthy and diseased hearts, in order to produce more definitive conclusions. The technique could also be extended to the right ventricle (RV) with the incorporation of a RV geometrical model and a more robust phase unwrapping algorithm. By incorporating active contour models in the model design, the guide point positions can be further improved using the magnitude reconstructed data.

4.5 Conclusion

The guide point modelling approach to segment 3D cine DENSE data shows promising results, offering a significant reduction in the segmentation time required for a 3D data set.

The methods presented here use motion trajectories to propagate a finite element model across the cardiac cycle, while adjusting to the geometrical shape of each epicardial and endocardial surface. LV mass and volumetric results show good correlation when compared to previous studies. The results further show no significant area-based differences between manually defined contours and the model derived contours. The initial model parameters provide the best results. However,

model parameter variations can be used while still maintaining accurate LV segmentation.

This work is a significant step towards the automation of 3D cine DENSE data analysis.

4.6 Acknowledgements

The authors appreciate the valuable contribution of Professor Jeffrey W. Holmes M.D., Ph.D. by providing the left ventricular finite element model for this study.The authors would like to further thank Ian Burger, Ph.D. and Drew Gilliam Ph.D. for their helpful discussions regarding the segmentation algorithm, Muhammad Saleh, .MSc for his contribution in the manual segmentation of the short axis data and Katy Parker for her expertise in using the finite element model.

Chapter 5

Ventricular Motion Analysis by Combining Long Axis and Short Axis 2D cine DENSE MRI and its Application to Cardiac Dyssynchrony

Abstract

The nature of motion and contraction of the ventricles impel a three dimensional (3D) analysis. However, in the absence of true 3D data, by combining results from 2D data in the longitudinal and circumferential directions, may allow for a more complete analysis of function in healthy and diseased cardiac tissue. Post processing techniques are presented for assessing right and left ventricular function and strain, using long and short axis cine displacement encoding with stimulated echoes (DENSE) data. Two-dimensional tissue tracking methods as well as tangential strain calculations are shown in the longitudinal and circumferential directions. Healthy volunteer data show regional strain that corresponds to previous 2D DENSE and myocardial tagging studies. Data of patients suffering from right and left bundle branch blocks were analyzed and the dyssynchrony quantified. In both healthy and diseased patients, both the long axis and short axis results correlate well with each other. These techniques are shown to be effective in identifying regional wall motion and strain, and are suitable to quantify interventricular dyssynchrony.

5.1 Introduction

Cardiovascular disease (CVD) remains a leading cause of death worldwide, accounting for 33.6% of deaths in the USA in 2007 [1]. A vast number of CVD's can affect any region of the myocardium. One such example is cardiac dyssynchrony where cardiac electrical conduction problems result in dyssynchronous contraction and impaired cardiac function. Electrical dyssynchrony is the result of any blockage or delay in the electrical stimulus required for mechanical contraction. The complexity of myocardial contraction is, however, such that mechanical dyssynchrony can occur due to and be related to regional myocardial disorders, as opposed to a stimulation delay [80]. Cardiac resynchronization therapy (CRT) is a well-established therapy for patients suffering from cardiac dyssynchrony [81]. The current criteria for receiving CRT is a QRS complex measurement of 120 ms or higher, but 30-40% of patients do not benefit from therapy [82]. Accurate identification of prospective responders to CRT has been the major impetus for development of meaningful measures of mechanical dyssynchrony, which may be a better predictor of outcome than electrical criteria.

Cardiovascular magnetic resonance (CMR) techniques are used to assess myocardial properties such as strain and motion, and global parameters such as volumes and ejection fraction. Helm et al. and Lardo et al. reviewed MRI methods for measuring mechanical dyssynchrony and the increasing role of cardiac MRI in selecting CRT responders [56, 83]. Abraham et al. showed the advantages of MR techniques in acquiring strain in three orthogonal directions when analyzing myocardial deformation [80]. Leclercq et al. showed the importance of mechanical coordination in ventricular function, as mechanical synchrony is independent of electrical synchrony [84]. Zwanenberg et al. further showed in the healthy heart how mechanical activation follows electrical activation, so that mechanical asynchrony is a more appropriate parameter to select candidates for CRT treatment [85]. They introduced concepts such as time to onset of strain, which is directly influenced by CRT, and time to peak strain to select candidates suitable for CRT.

Displacement encoding with stimulated echoes (DENSE) is a quantitative MR imaging technique for assessing regional myocardial displacement and strain [2, 3]. DENSE encodes tissue displacement directly into the phase of the stimulated echo (typically with reference to end diastole), allowing for extraction of motion and strain data at a pixel resolution. A recently developed navigator guided 3D cine DENSE sequence has been developed in order to quantify motion and strain in three dimensions within both ventricles in a single scan [4]. The sequence, however, requires a lengthy scan time so that it is not feasible to acquire full 3D patient data sets at this time.

Previously, cardiac research has been predominantly focused on the left ventricle (LV), and the inclusion of the right ventricle (RV) has been limited. This is in part due to the RV's thin myocardial wall, complex geometry and eccentric motion. However, a number of RV analysis techniques have been implemented in MR in order to quantify RV motion and strain. Wen et al. presented mean circumferential strain results using 2D cine DENSE data where the entire RV is represented as the free wall [38]. The strain was assessed based on the lengthening of the mid-wall RV contour. Using the RV mid-wall, healthy RV function has been quantified by Auger et al. using 3D cine DENSE data [33]. A number of myocardial tagging studies have also been completed that include RV analysis. Fayad et al. assessed RV and LV regional function using long and short axis myocardial tagging data [36], while Klein et al. focused primarily on the RV [57]. Young et al. and Haber et al. used 3D reconstructed geometrical models in order to analyze the 3D global function and local deformation of the RV using myocardial tagging [28, 30].

As the function of the RV can be affected in diseases of the LV, and vice versa, it is difficult to ignore the complex ventricular interaction when assessing heart function [51, 52]. In this work, methods are presented to quantify motion and strain in both ventricles using both long (LA) and short axis (SA) 2D cine DENSE MR data. We present a method to combine LA and SA data to provide an estimate of 3D function in order to fully assess ventricular motion in the absence of 3D cine DENSE data. The application of these methods to assess inter-ventricular dyssynchrony to distinguish healthy from diseased hearts are further described and demonstrated in this paper.

5.2 Methods

5.2.1 Imaging protocol

Two dimensional echo planar imaging (EPI) cine DENSE data were acquired from a single healthy volunteer and three patients on a 1.5 T Siemens Avanto scanner (Siemens Medical Systems, Erlangen, Germany). A four-channel body phased array RF coil was used to image subjects in a long axis four chamber view and three short axis views (apical, mid and basal). The patient and healthy volunteer data presented were acquired at different times with slight variations in the imaging parameters. Pertinent imaging parameters were as follows: field of view = 350 × 252 -350 mm^2, echo time = 11 – 17 ms with view sharing; repetition time = 17 – 20 ms; slice thickness = 8 mm; pixel size = 2.81 × 2.81 mm^2; temporal resolution = 17 – 20 ms; displacement encoding frequency = 0.1 cycles / mm. The strain results for the healthy and patient data were interpolated between different data sets in order to compensate for the small variation in temporal resolution. Prospective electrocardiogram gating was applied and only 85% of the cardiac cycle was imaged to account for beat-to-beat variations. Displacement was encoded in two orthogonal in plane directions and image reconstruction was performed online. All imaging was conducted after informed consent and in accordance with protocols approved by The University of Virginia Institutional Review Board.

5.2.2 Image analysis

The post processing of cine DENSE data typically includes tailored steps to analyze the myocardium. All software development was performed offline using custom code programmed in MATLAB (The Mathworks Inc., Natick, MA).

5.2.2.1 Myocardial segmentation and phase unwrapping

Quality guided path following phase unwrapping is typically applied for cine DENSE images [27, 31]. However, the thin-walled RV spans only 1 – 3 pixels and limits the reliability of the phase quality maps used to guide the path following. Robust phase unwrapping was achieved here by manually demarcating epicardial and endocardial

contours for the RV and applying spatio-temporal quality guided path following phase unwrapping. The phase data from the two encoding directions were combined to create 2D Eulerian displacement fields. Apical SA data were excluded from analyses, as it was difficult to accurately define the RV myocardial borders. Figure 5.1 illustrates contoured cine DENSE magnitude and phase-unwrapped images in short axis (top) and long axis (bottom row) views, respectively, with corresponding 2D displacement fields.

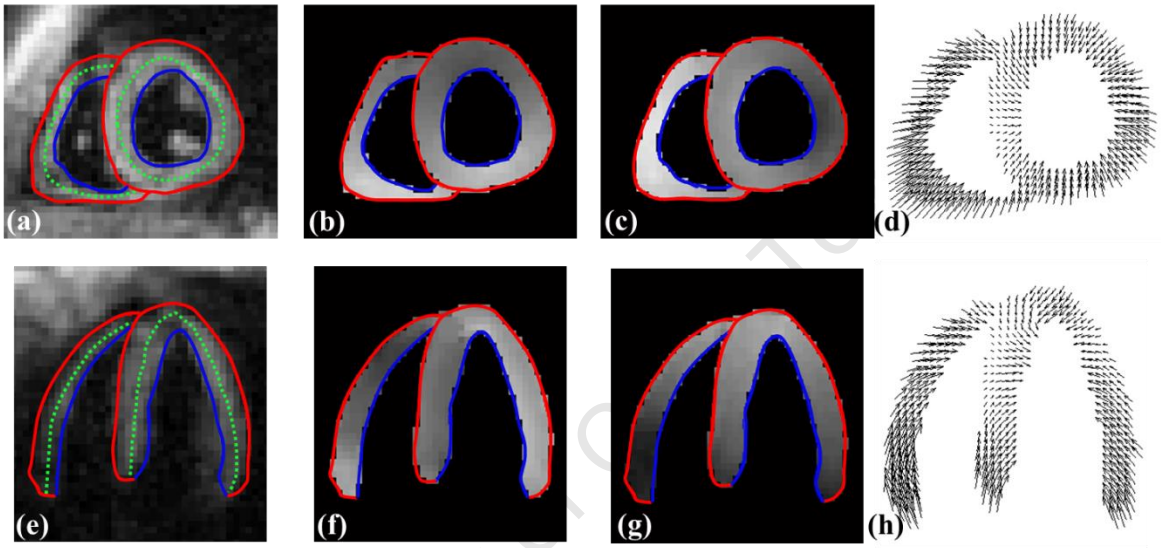

Figure 5.1: (a,e) Contoured DENSE magnitude images depicting mid-lines, (b,f) images phase encoded in x-direction, (c,g) images phase encoded in y-direction, and (d,h) corresponding vector displacement fields. All images are from an end systolic cardiac phase.

5.2.2.2 Tissue tracking and strain calculation

Due to the thin wall and complex shape of the RV it is difficult to acquire a full 2D strain tensor. It is therefore proposed to measure a Lagrangian strain taken tangential (E_{tt}) to the mid-wall. A contour mid-way between the epicardial and endocardial contours on the first frame (end diastole) was identified and pixel-spaced points along this contour were used as tissue tracking seed points. The mid-line points are shown in Figure 5.1(a, e). Two dimensional distance weighted linear interpolation of the nearest vector displacement fields around the seed points was used to determine displacement fields for the seed points and then compute frame-to-frame motion trajectories for the seed points using the method described previously [27]. As prospective gating only allowed 85% of the cardiac cycle to be imaged and fifth order Fourier basis functions have been shown

previously to sufficiently describe cardiac motion [32], temporal fitting was done in each ordinate direction for each of the trajectories using a 10^{th} order polynomial.

Lagrangian strain was calculated directly from the 2D motion trajectories. The strains are calculated in the longitudinal and circumferential directions from the long axis and short axis data, respectively. Considering an arbitrary point in the mid-wall p_n, where n represents a position along the mid-line, the tangential strain is obtained from the two adjacent points. If the undeformed length, l_0, is the distance between trajectory points p_{n-1} and p_{n+1} at the time of displacement encoding ($t=0$), and the deformed length, l_t is the distance between the same trajectory points at time t, the tangential strain (Ett) at p_n is given by

$$E_{tt} = \frac{1}{2}\left[\left(\frac{l_t}{l_0}\right)^2 - 1\right] \tag{5.1}$$

Unlike the LV there is no standard method for dividing the RV into anatomical segments, in both 2D long and short axis MR data. Various methods for dividing the RV using 3D MRI data have been proposed [28, 33, 36]. Klein et al. proposed dividing the RV into three segments when using 2D data, namely, superior, mid and inferior walls [57]. However, in this paper, we propose dividing the short axis RV into two anatomical segments, where the anterior two-thirds of the mid-wall are classified as the RV free wall and the remaining third as the diaphragmatic RV. The long axis RV is divided into two segments, the basal and apical RV. The LV segments are divided according to [34]. Figure 5.2 illustrates the anatomical LV and RV segmental divisions. Due to poor SNR, certain segments were excluded from analyses.

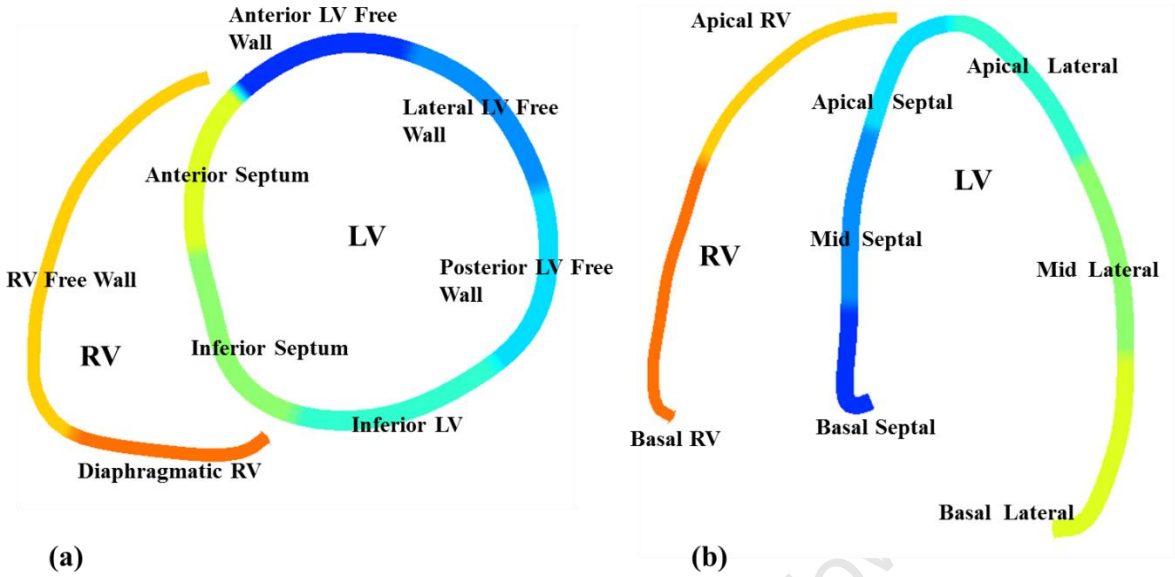

Figure 5.2: Myocardial segments for interventricular strain analysis for (a) short axis and (b) long axis data.

5.3 Results

Tangential strain maps and 2D ventricular motion for both the LV and RV for a healthy volunteer are illustrated in Figure 5.3. The contraction of ventricles is evident by the inward direction of the yellow displacement vectors, while the change in color represents the change in regional strain for long axis and short axis views, respectively. The evolution of displacement and strain can be appreciated during early systole, mid systole and end systole, respectively.

Figure 5.4 represents the mid-wall E_{tt} strain time curves for the different segments of the RV and LV for a healthy volunteer in the circumferential and longitudinal directions respectively. The values are shown as the mean strain for each anatomical segment. The graphs illustrate a synchronous contraction for both the LV and RV. All strain values are consistently negative, indicating muscle shortening. Strain in the longitudinal direction, particularly for the RV, shows higher values when compared to circumferential strain.

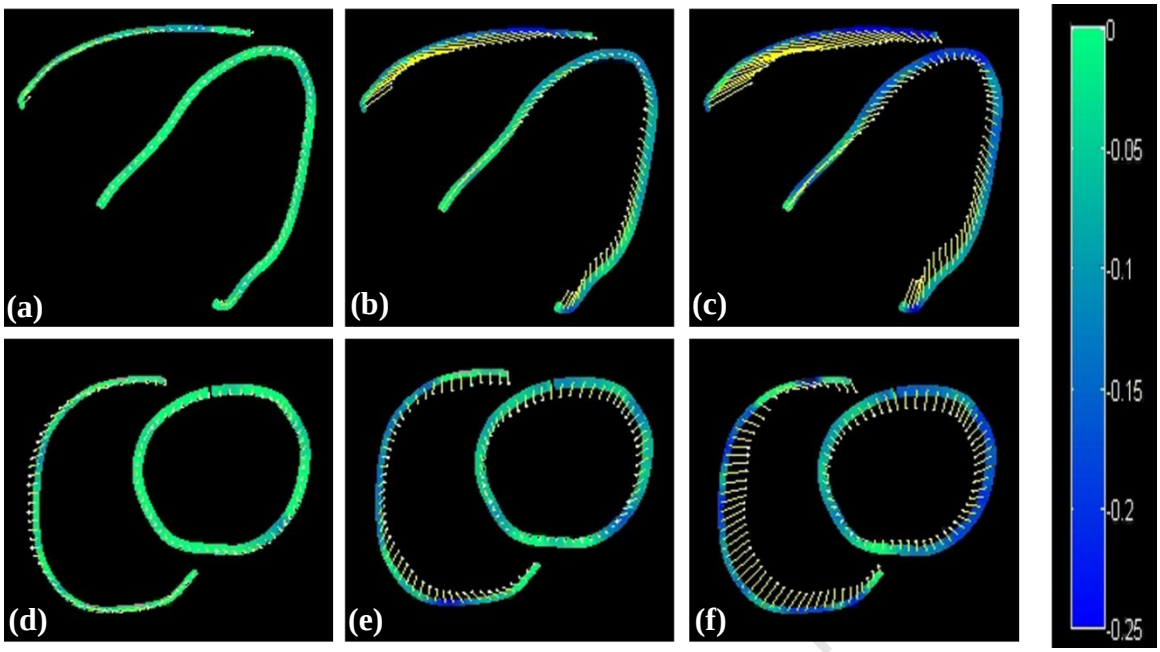

Figure 5.3: Tangential strain (E_{tt}) and displacement fields obtained from displacement trajectories for a healthy volunteer in long axis (a-c) and short axis (d-f), views respectively. (a, d) end diastole, (b, e) mid systole, and (c, f) end systole.

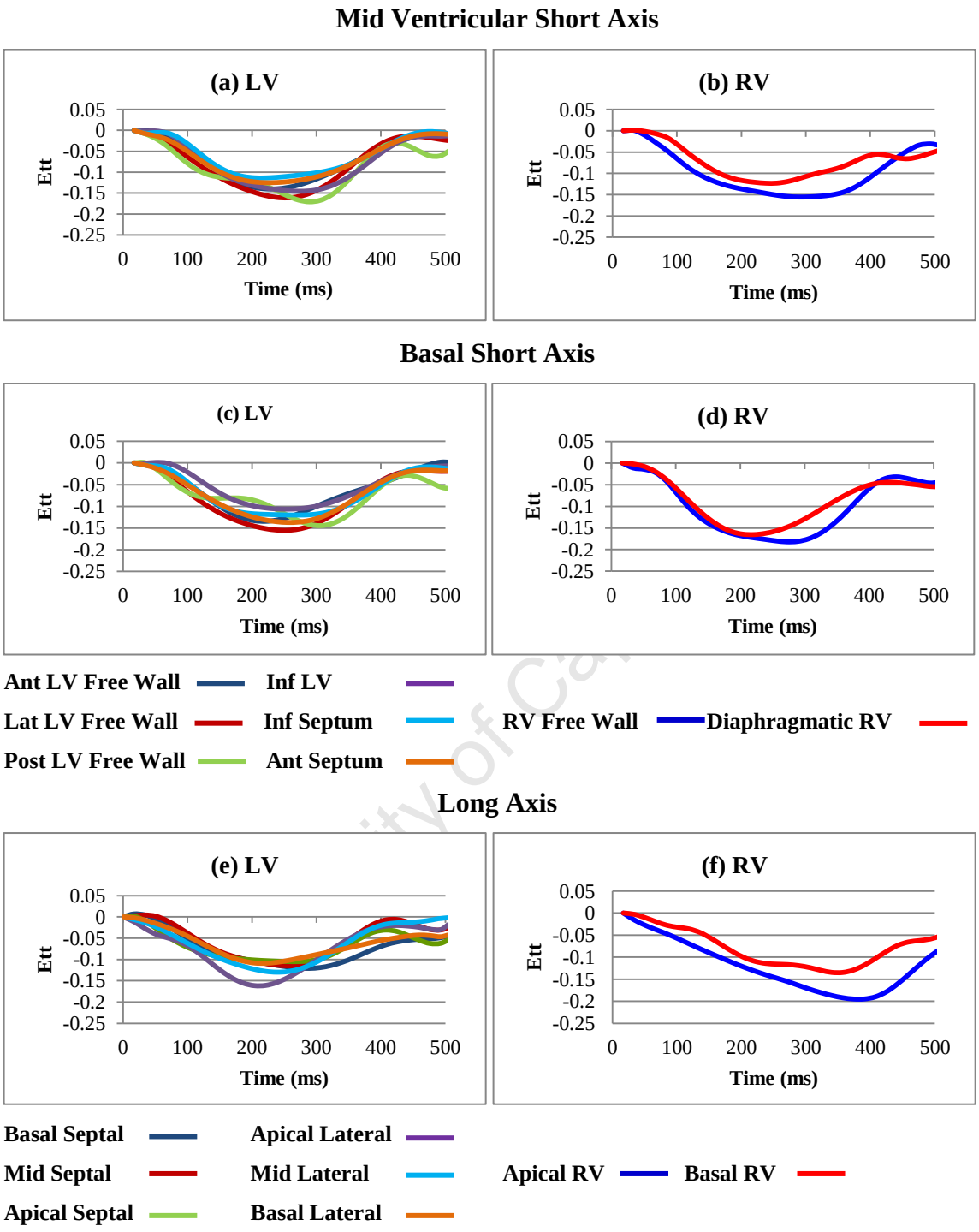

Figure 5.4: Strain time curves for a normal volunteer for a mid ventricular short axis LV (a) and RV (b), respectively; a basal short axis slice for the LV (c) and RV (d), respectively; and long axis LV (e) and RV (f) images, respectively.

Figure 5.5 illustrates the mid-wall E_{tt} strain time curves for a patient with a LBBB. The asynchronous contraction of the LV myocardium is evident in the short axis strain time curves, where a delayed onset of strain of roughly 50 ms in the posterior LV free wall and inferior LV is evident. The basal SA slice further shows delayed onset times in the posterior and lateral LV free walls, and in the anterior septum. The LA strain shows delays in peak strain in the lateral LV. The RV shows early strain peak times, except in the SA basal slice where the RV free wall shows a delayed contraction similar to that of the LV. When compared to the RV, the LV segments show delays in peak strain times in all SA and LA results. Certain segments were excluded due to low SNR, which may occur either because of a thin myocardial wall or through-plane dephasing.

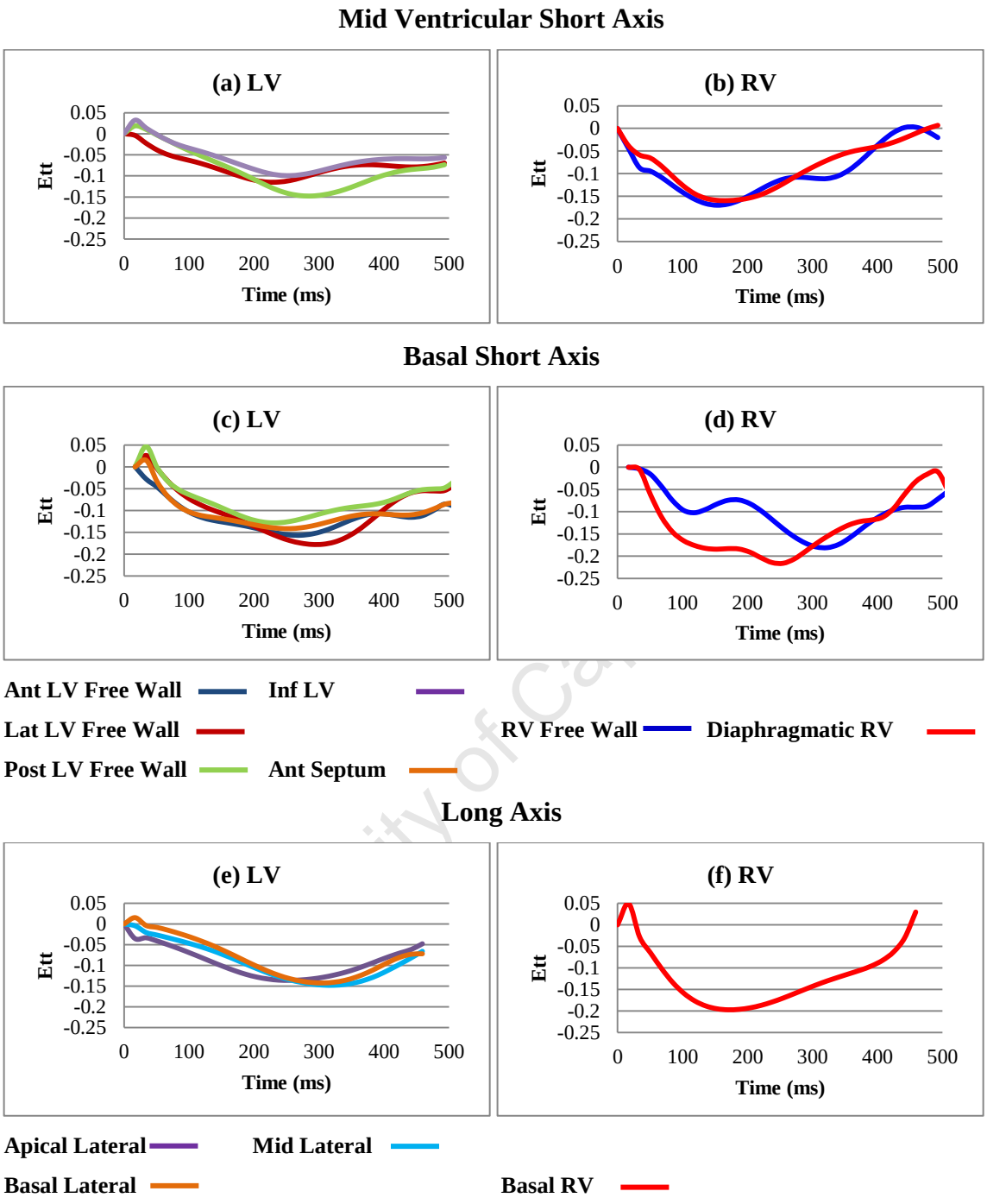

Figure 5.5: Strain time curves for a patient with LBBB: (a, b) mid ventricular short axis LV and RV strains, respectively; (c ,d) strains for basal short axis LV and RV, respectively, and (e, f) strains for long axis LV and RV, respectively.

Figures 5.6 and 5.7 illustrate the effects of a RBBB and regional myocardial infarct in a patient. Figure 5.6 includes a gadolinium-enhanced image showing an anteroseptal infarct with the corresponding strain and vector displacement fields at end systole. Delays in peak strain time is shown in the RV diaphragmatic and free wall in the mid SA slice, with delays of roughly 65-85 ms in onset of strain times. The RV free wall in the basal short axis slice shows a delay of roughly 120 ms in time to peak strain. The septal regions in the LA data show zero strain in the apical septal LV, and low strain values with a delay in onset time in the basal septal and mid septal LV. The curvature of the strain time curves further illustrates abnormal function in the region, while the basal and mid lateral regions of the LV show normal strain values, but with delayed peak times. The basal RV segment in the LA view shows a delayed onset time of roughly 50 ms with a delay in peak strain time of the order of 220 ms. This corresponds well with the RV free wall in the mid and basal short axis slices.

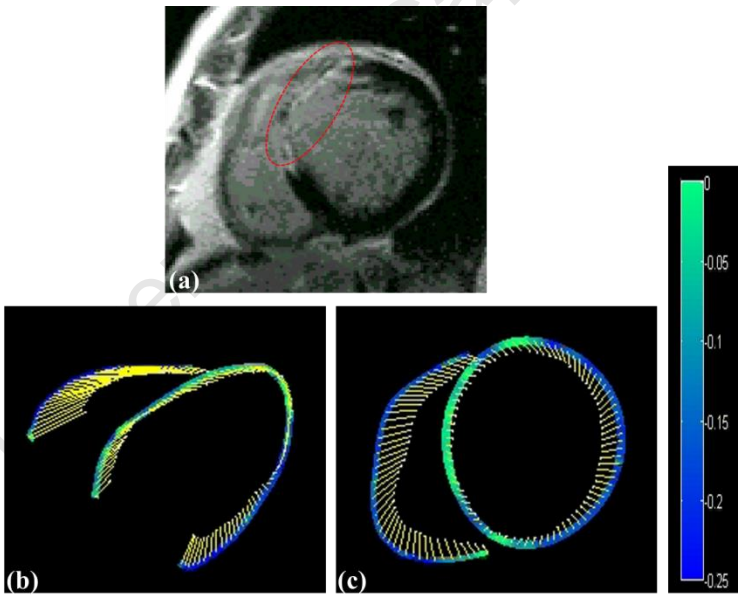

Figure 5.6: (a) Mid ventricular short axis Gd-enhanced image with the corresponding strain and vector displacement fields (b, c).

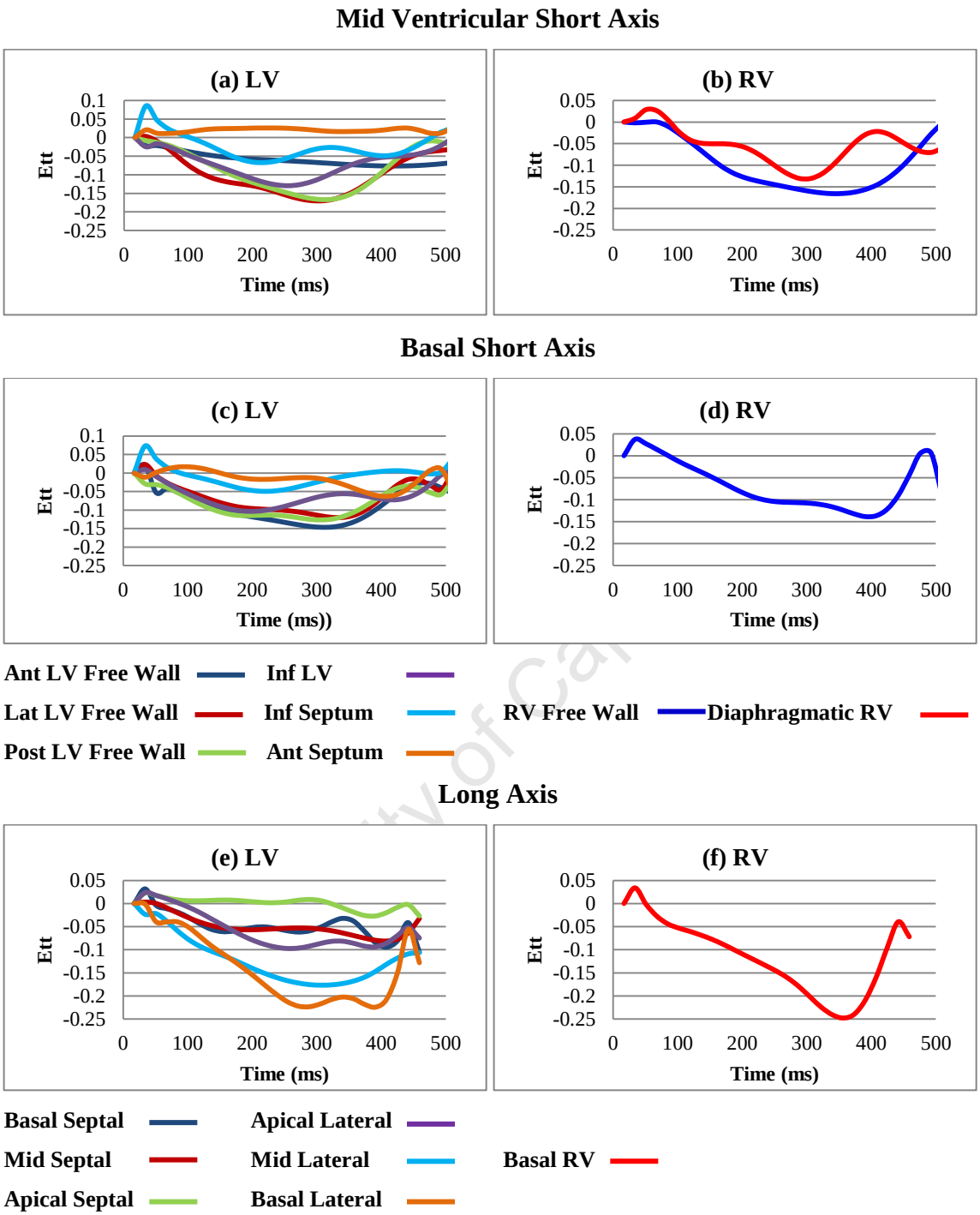

Figure 5.7: Strain time curves for a patient with RBBB with an anteroseptal infarct. (a, b) tangential strain time curves for the LV and RV, respectively, for a mid ventricular short axis slice; (c ,d) strains for basal short axis LV and RV, respectively; and (e, f) long axis LV and RV strains, respectively.

Figure 5.8 shows a second patient with RBBB, this time without an infarct. A delay in onset of strain of 100-140 ms in the anterior LV free wall and inferior septum is evident in the SA mid ventricular strain-time curves, while a delay in onset time of roughly 85 ms is evident in the anterior and inferior septum of the LV in the basal SA slice. A delayed onset is seen in the RV free wall, with a delayed peak strain time in both mid and basal slices. The basal and apical RV segments of the LA data each show delayed onset times of roughly 120 ms. The LV septal segments in the LA data further show delayed onset strain times, delayed peak times, and low strain values.

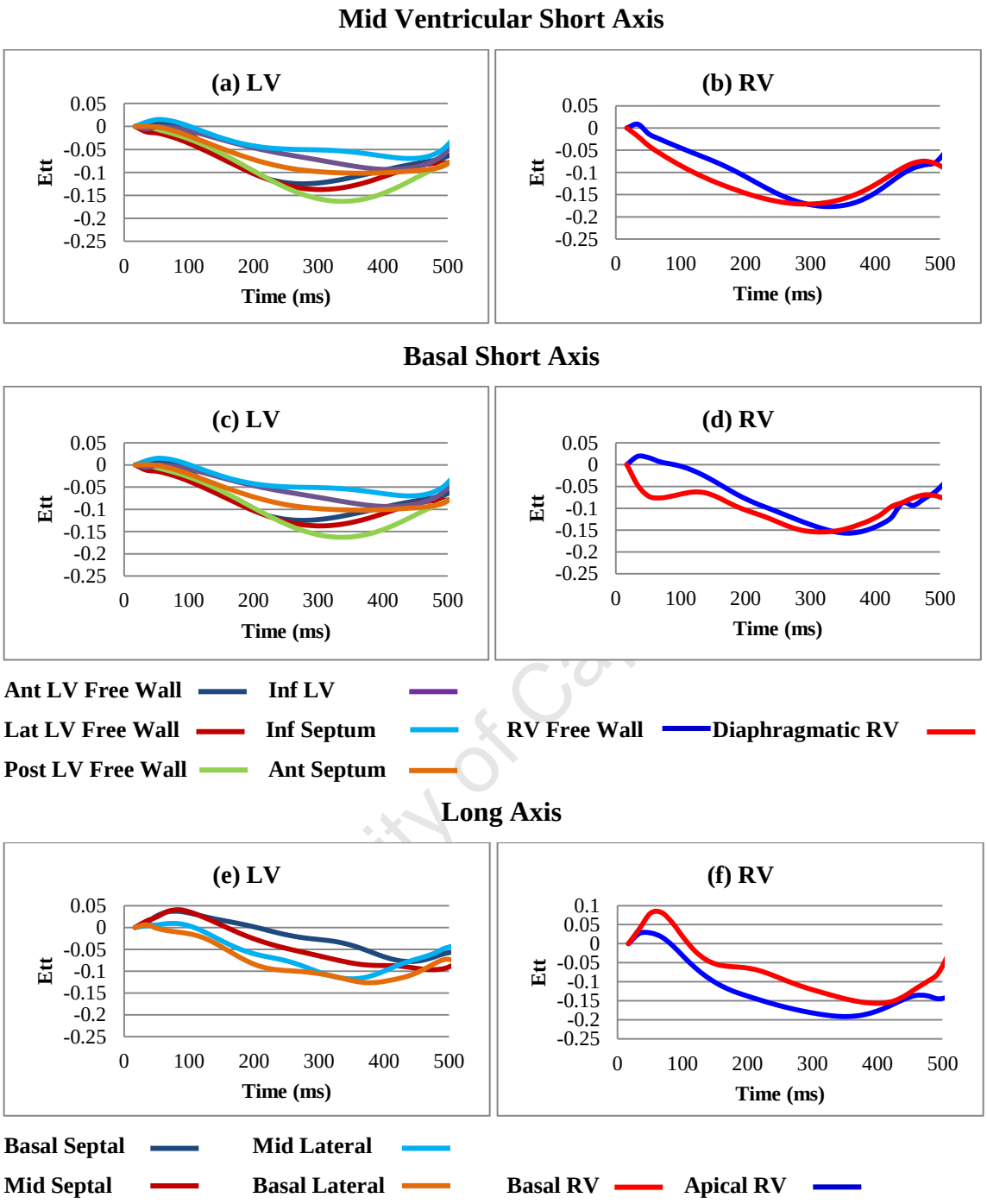

Figure 5.8: Strain time curves for a patient with RBBB for the LV and RV, respectively, for (a,b) a mid ventricular short axis slice; (c,d) a basal short axis slice; and (e,f) a long axis slice.

5.4 Discussion

This study presents methods for analyzing 2D cine DENSE data in two different imaging planes, in order to assess motion and function in the healthy and diseased heart more thoroughly, in the absence of 3D data. The cine DENSE methods and techniques described here are suitable for analyzing both the left and right ventricles.

Two dimensional tissue tracking methods were tested on a rotating phantom described in [27]. The tracking results illustrated in Figure 5.3 show a synchronous ventricular contraction and a good representation of cardiac motion in long and short axis views. No spatial smoothing was applied to the data other than a temporal polynomial fit, which was applied to the motion trajectories. This provides a more realistic trajectory behavior of cardiac motion, allowing for strain to be calculated at any temporal resolution. Normal strain calculation results for both the LV and RV compare favorably with previous 2D DENSE and myocardial tagging studies [12, 36, 38]. Only one healthy volunteer was included in this study to illustrate the expected evolution of strain in the different anatomical segments in a healthy heart, in order to demonstrate the deviation from healthy strain patterns in a diseased heart. It may be difficult to directly compare strain results presented in this study to previous studies, as strain-time curves are presented as a mean strain within each anatomical segment, and the RV segmental divisions vary between studies, causing slight variations in reported peak strain values.

Zwanenburg et al. showed how in healthy myocardium, mechanical activation follows electrical activation and how time to onset and time to peak can be used to assess dyssynchrony and select candidates for CRT treatment [85]. This work presents methods using both time to onset and time to peak to quantify and assess interventricular dyssynchrony.

The LBBB results show good correlation between SA and LA strain results. When compared to the RV and the healthy LV, each LV segment shows a delay in time to peak strain. The SA mid ventricular strain time curves show a delay in onset time and time to

peak strain in the inferior LV and the posterior LV free wall. The SA basal slice further shows delays in the LV lateral free wall and the posterior LV in both onset times and peak strain times. This is in good correlation with the LA data, where the basal, mid and apical lateral segments show delays in onset times and peak strain times. Results illustrate that in LBBB the RV has earlier time to peak strain than the LV.

The ability of DENSE to quantify myocardial dysfunction is shown well in Figure 5.6, where the tangential strain maps and displacement vector images show the region of the infarct. The strain is represented as zero during end systole by the color, and a delay in contraction of the ventricular segments is evident as the yellow displacement vectors are not fully extended towards the center of the LV during end systole. In Figure 5.7 the zero strain shown in the anterior LV free wall and anterior septum of the mid ventricular SA slice, indicate the location of the patient's infarct, while the onset delay of the diaphragmatic RV and time to peak delay of the RV free wall indicates the presence of RBBB. The basal LV SA slice shows poor contraction in the inferior and anterior septum, and, like the mid slice, shows a delay in contraction in the remaining LV segments. The LA LV strain time curves show poor contraction in the septal segments, with late peak times in the lateral LV segments. The SA and LA data of the RV also correlate well and demonstrate a delay in both times to onset and peak strain in the RV.

Both LA and SA strain time curves illustrate the asynchronous contraction with delayed onset times and delayed strain peak times in both the LV and RV strain results for the patient with a RBBB and no infarct. The anterior and inferior septal segments, and the inferior LV segment in both the LV mid and basal slices show poor contraction, delayed onset times and time to peak. This compares well with the LA results, showing late onset and contraction times in the septal regions, with the lateral region showing delayed peak strain times. In the SA results, both the basal and mid ventricular slices show delayed onset times in the RV free wall, and delayed peak strain times in the RV free wall and diaphragmatic RV. We note that during a LBBB the RV is forced into an early time to peak, while in the RBBB case, the RV peak time is delayed.

According to a study by Helm et al, circumferential shortening is the preferred measure when analyzing interventricular dyssynchrony as longitudinal analysis suffers from low dynamic range [56]. That study, however, only analyzed the LV and used a canine model of dyssynchronous heart failure, which limits the assessment of damaged/fibrotic tissue and regional contraction abnormalities, such as timing delays.

Helm et al, together with Levya et al. proposed using radial strain analysis to further facilitate quantifying dyssynchrony [56, 86]. Although radial strain analysis is a good option for LV analysis, little can be accomplished with the thin wall of the RV. Studies by [51, 87] show the predominantly longitudinal contraction and strain found in the RV. Therefore, using both LA and SA data when analyzing the RV should improve the reliability of results when analyzing interventricular dyssynchrony. Future work should include a larger study incorporating more patients before and after LV and bi-ventricular pacing in order to assess the advantages of LA data when analyzing both LV and RV dyssynchrony.

Limitations of this study include signal loss caused by intra-voxel dephasing in stimulated echo imaging during tissue deformation [88]. Because the thickness of the RV is similar to the in plane pixel size and considerably less than the slice thickness, partial volume effects further reduce the signal to noise ratio (SNR) in the RV. Errors due to through plane motion still pose challenges in routine cine DENSE analysis, particularly in the RV. The encoding frequency k_e can be reduced in order to limit intra-voxel dephasing in the RV and improve SNR but at the expense of displacement sensitivity. A measure of data confidence was developed to guide interpretation in regions of low SNR and to signal the presence of phase-unwrapping or breath-hold misalignment errors. Certain ventricular segments were therefore excluded during analysis.

In order to compensate for through plane motion in cine DENSE and track the myocardium in 3D, a DENSE slice following method is introduced [31]. This method however suffers from reduced SNR and requires multiple breath-holds for encoding a single slice in three directions, potentially leading towards registration errors. Future

work should incorporate patient 3D spiral cine DENSE data, where tissue motion and strain can be quantified for the entire LV and RV [4, 33].

5.5 Conclusion

The initial results presented here provide a good representation of ventricular function, showing the feasibility of using 2D cine DENSE data acquired in different views to quantify abnormal motion and strain in diseased tissue. Strain results in the longitudinal and circumferential directions are in good agreement and provide useful insights in regional myocardial strain analysis.

Chapter 6

Discussion

This thesis presents techniques for the analysis of intramyocardial function using cine DENSE MRI, including the first comprehensive study of RV motion and strain in three dimensions using 3D cine DENSE MRI and a semi-automated segmentation algorithm for the LV. A method is also presented to quantify LV and RV cardiac dyssynchrony by combining two orthogonal 2D cine DENSE data sets in the absence of 3D data, which is not yet clinically feasible due to long acquisition times.

Three dimensional RV strain results compare favorably to previous RV CMR studies, with the proposed RV anatomical divisions relating well to regional differences in function. As the RV myocardium varies in wall thickness between the base and apex, this is reflected in the functional parameters measured. Strain is consistently lower in the inflow region when compared to the apical and mid RV regions.

The evolution of strain in Figures 3.5 and 3.6 show a distinct pattern of regional mechanical activation. In contrast to the study by McKenna et al. of RV function [54], the present results show mechanical contraction from the base to the apex. This is in agreement with results of Buckberg et al. and Ballester-Rodes et al. who also concluded that mechanical activation of the ventricles occurs in a basal to apical direction [89, 90]. Ballester-Rodes present the heart as a single band with a double-loop helicoid configuration, while Buckberg shows that initial cardiac motion occurs at the base during isovolumetric contraction. Zwanenberg et al. present the time to peak shortening on the LV and used bull's eye illustrations to depict that the first time to peak occurs in a mid-basal region as opposed to an apical region [91]. The present results were based on 5 data sets only and should be extended to a larger sample of the population in order to address these discrepancies between different studies. Dividing each RV segment into a further

three segments, namely superior, mid and inferior regions, would allow for a more complete analysis of RV regional function.

In the absence of 3D data, 2D cine DENSE has been shown to accurately quantify myocardial strain [38, 92]. By using data from two orthogonal views in the analysis, it is possible to assess myocardial deformation and strain in the circumferential and longitudinal directions separately.

A variety of methods to detect dyssynchrony using strain measurements are summarized in Lardo et al. [83]. Such methods include temporal uniformity of strain / circumferential uniformity of strain (CURE). Here the dynamic strain values in each myocardial segment are subjected to Fourier analysis and decomposed into zero-order terms, with the results ranging from 0 to 1 (1 = synchrony, 0 = dyssynchrony). CURE and any of the other methods could be applied to cine DENSE analysis of LV dyssynchrony [92], however, they are precluded from analysis of the RV because of its lack of spatial periodicity and the low spatial resolution available. In this work, the time to peak strain and time to onset of strain were the metrics used to identify regions of mechanical dyssynchrony.

There is good agreement between the 2D mid-line strain results of the LV and RV for the basal and mid ventricular slices, and between the SA and LA data sets. The differences in strain between the healthy and diseased patients are clearly evident. Furthermore, the difference between the LBBB and the RBBB manifests clearly in the differences in time to peak strain. In LBBB, the RV is shown to have early peak times when compared to the LV, while in the RBBB results, the RV is shown to have a delayed time to peak strain. Future studies involving patients before and after CRT would allow investigation of the effects of CRT on the time to onset and the validity of using time to peak strain as a tool for identifying suitable patients for the procedure. The initial results using 2D cine DENSE in volunteers and heart failure patients suggest that the above methods can be used to assess LV and RV strain and, as such, interventricular dyssynchrony.

A limiting factor in the myocardial strain analysis for both 2D and 3D DENSE was the time required to manually segment both the LV and RV from surrounding anatomical structures. Previous segmentation methods have been presented for the LV using 2D cine DENSE [47]. This work presents a semi-automated method for segmenting the LV in 3D DENSE data.

Like previous 2D cine DENSE segmentation methods, the present algorithm also relies on accurate phase unwrapping [47]. By reducing the displacement encoding frequency k_e sufficiently, it is possible to ensure that no phase wrapping occurs. However, by lowering the value of k_e, there is a decrease in displacement sensitivity [26]. As shown in [3, 25], practical values of k_e make phase unwrapping inevitable. A robust phase unwrapping algorithm is presented in [27] without the need for pre-defined myocardial contours. However, due to intravoxel dephasing and partial volume effects, regions of myocardium of 1-2 pixels in thickness experience reduced displacement measurement accuracy and therefore phase unwrapping errors [47]. The segmentation method presented here is therefore only suitable for the LV, as the RV thin wall often does not span more than 2 pixels and suffers from low SNR in certain regions. A segmentation algorithm for the RV is outside the scope of this project as the RV requires a more robust phase unwrapping algorithm. However, the concepts and segmentation algorithm presented in this work can be expanded to the RV.

The LV segmentation results presented show an accurate and reproducible segmentation technique, as the global parameters and spatial overlap results show good agreement between model derived contours and the manually defined contours.

There are a number of advantages to this segmentation algorithm: the method is independent of the shape of the LV myocardium, only high quality data (vector spatial derivative calculations and high SNR filters) are used for LV volume propagation, and user interaction is significantly reduced. As current DENSE analysis methods depend on the manual contouring of each data set, the algorithm will produce more accurate results than a trained user due to user fatigue. A single experienced user may also struggle to

consistently identify the same region of myocardium. However, the algorithm is based on the high SNR data present, and the segmentation algorithm only includes myocardial vectors that have been incorporated in tissue tracking.

A low percentage (5.6%) of contours required readjustment after the segmentation algorithm. Currently, this is done by the user as each contour is manually adjusted according to the LV boundary. An accuracy checking algorithm could be implemented after segmentation. As only high SNR voxels are incorporated, an active contour 'checking step' can be implemented on the magnitude reconstructed images. Each contour would be adjusted automatically, thus further reducing user interaction and limiting the need for a user to make a subjective decision.

Limitations of this work include the low SNR associated with the stimulated echo in DENSE and the effects of through plane dephasing, which remain significant obstacles to routine ventricular analysis with cine DENSE. Various regions of myocardium in both the 2D and 3D data sets were excluded from analysis due to low SNR and unreliable strain measurements and the accurate propagation of guide points was influenced by noisy displacement information. The 3D cine DENSE sequence consists of a long scan time, therefore limiting the use of 3D DENSE in a clinical setting and the ability to acquire 3D patient data. Unlike slice following, 2D cine DENSE does not take into account the effects of through plane motion, which is experienced during the cardiac cycle, thus potentially lowering SNR in certain regions of the myocardium.

Future work should look to investigate whether the phase encoding frequency can in fact be reduced to limit phase wrapping and improve the SNR, particularly in the RV, without the tradeoff of losing displacement sensitivity. This could work in conjunction with implementing a more robust phase unwrapping algorithm for the RV, thus allowing for the implementation of a segmentation algorithm for both ventricles.

An increased database of both healthy and diseased data should be acquired. This will allow a more comprehensive analysis of RV strain and motion, and the analysis of patient

data using 2D bi-ventricular dyssynchrony methods and techniques. By increasing the number of patient data sets before and potentially after CRT, the use of time to onset and time to peak strain as indicators of patients suitable for CRT could be examined. As RV analyses are limited, methods like 3D DENSE could be used to investigate how diseases of the LV affect the RV and vice versa. These studies would improve diagnosis of cardiac disease and advance our understanding of cardiovascular disease and myocardial function.

Chapter 7

Conclusion

When compared to other CMR imaging techniques, cine DENSE has been shown to provide accurate and repeatable cardiac motion and deformation measurements. In this work, we have presented methods that advance the analysis of cine DENSE data and contribute towards our understanding of regional myocardial function.

The methods presented in this dissertation allow one to quantify and assess intramyocardial function, and have been shown to be accurate and produce results that compare well with previous studies. Tissue tracking, temporal fitting and strain calculation methods were shown to be reproducible and produce accurate results. The ventricular segmental divisions were defined according to anatomy, structure and orientation of the heart, which allow for the assessment of regional cardiac function. Algorithms and techniques were presented and verified using healthy human data, while showing promising results in the diagnosis of cardiac electrical conduction problems.

The analysis of the RV at multiple cardiac phases was for the first time implemented using healthy human 3D cine DENSE data at a previously unattainable temporal resolution. Compared to 2D cine DENSE of multiple slices, 3D DENSE imaging captures the true volumetric information of the LV, providing a more accurate representation of cardiac motion and function.

A major limiting factor in 3D DENSE is the time required to segment the ventricles. The 3D semi-automated segmentation algorithm for LV using 3D cine DENSE MRI data presented in this dissertation contributes towards a fully automated myocardial analysis. The segmentation algorithm presented is fast, accurate, repeatable, and reduces user interaction.

In the absence of 3D cine DENSE data, two orthogonal 2D cine DENSE views were used in order to assess cardiac function in both the LV and RV. Methods show the ability to quantify both motion and strain in the healthy and diseased heart. Strain results in the longitudinal and circumferential directions present regions of myocardium affected by left and right bundle branch conduction problems.

The combination of this work can contribute towards a faster, more accurate and reliable assessment of cardiac function using DENSE imaging data in a healthy and diseased heart through (1) segmenting the LV myocardium from surrounding structures with minimal user intervention in an acceptable time, (2) tissue tracking methods in order to quantify ventricular motion in both the LV and RV, (3) strain calculation in order to assess regional cardiac function, and finally (4) using these measurements to diagnose and manage CVD's which affect either ventricle or both.

References

[1] Roger, V. L., Go, A. S., Lloyd-Jones, D. M., Adams, R. J., Berry, J. D., Brown, T. M., *et al.*, "Heart Disease and Stroke Statistics—2011 Update," *Circulation,* vol. 123, pp. e18-e209, 2011.

[2] Aletras, A. H., Ding, S., Balaban, R. S., and Wen, H., "Dense: Displacement Encoding with Stimulated Echoes in Cardiac Functional Mri," *Journal of Magnetic Resonance Imaging,* vol. 137, pp. 247-52, Mar 1999.

[3] Kim, D., Gilson, W. D., Kramer, C. M., and Epstein, F. H., "Myocardial Tissue Tracking with Two-Dimensional Cine Displacement-Encoded MR Imaging: Development and Initial Evaluation," *Radiology,* vol. 230, pp. 862-71, Mar 2004.

[4] Zhong, X., Spottiswoode, B. S., Meyer, C. H., Kramer, C. M., and Epstein, F. H., "Imaging Three-Dimensional Myocardial Mechanics Using Navigator-Gated Volumetric Spiral Cine Dense MRI," *Magnetic Resonance in Medicine,* vol. 64, pp. 1089-97, Oct 2010.

[5] Netter, F., "Interactive Atlas of Human Anatomy," *ICON Learning Systems. Version 2.0.,* 1998.

[6] Rohmer, D., Sitek, A., and Gullberg, G. T., "Reconstruction and Visualization of Fiber and Laminar Structure in the Normal Human Heart from Ex Vivo Diffusion Tensor Magnetic Resonance Imaging (DTMRI) Data," *Investigative Radiology,* vol. 42, pp. 777-789, 2007.

[7] Young, A., LeGrice, I., Young, M., and Smaill, B., "Extended Confocal Microscopy of Myocardial Laminae and Collagen Network," *Journal of Microscopy,* vol. 192, pp. 139-150, 1998.

[8] Hansen, J. T. and Netter, F. H. (2010). *Netter's Clinical Anatomy*. Available: http://www.mdconsult.com/public/book/view?title=Hansen

[9] Moore, K. L. and Dalley, A. F., *Clinically Oriented Anatomy* Philadelphia: Lippincott Williams & Wilkins, 2006.

[10] Axel, L. and Dougherty, L., "MR Imaging of Motion with Spatial Modulation of Magnetization," *Radiology,* vol. 171, pp. 841-845, 1989.

[11] Zerhouni, E. A., Parish, D. M., Rogers, W. J., Yang, A., and Shapiro, E. P., "Human Heart: Tagging with MR Imaging - A Method for Noninvasive Assessment of Myocardial Motion," *Radiology,* vol. 169, pp. 59-63, 1988.

[12] Moore, C. C., Lugo-Olivieri, C. H., McVeigh, E. R., and Zerhouni, E. A., "Three-Dimensional Systolic Strain Patterns in the Normal Human Left Ventricle: Characterization with Tagged MR Imaging," *Radiology,* vol. 214, pp. 453-466, 2000.

[13] Osman, N. F., Kerwin, W. S., McVeigh, E. R., and Prince, J. L., "Cardiac Motion Tracking Using Cine Harmonic Phase (Harp) Magnetic Resonance Imaging," *Magnetic Resonance in Medicine,* vol. 42, p. 1048, 1999.

[14] Osman, N. F., McVeigh, E. R., and Prince, J. L., "Imaging Heart Motion Using Harmonic Phase MRI," *Medical Imaging, IEEE Transactions,* vol. 19, pp. 186-202, 2000.

[15] Park, J., Metaxas, D. N., Axel, L., Yuan, Q., and Blom, A. S., "Cascaded MRI-Spamm for LV Motion Analysis During a Whole Cardiac Cycle," *International Journal of Medical Informatics,* vol. 55, pp. 117-126, 1999.

[16] Kuijer, J., Jansen, E., Marcus, J. T., van Rossum, A. C., and Heethaar, R. M., "Improved Harmonic Phase Myocardial Strain Maps," *Magnetic Resonance in Medicine,* vol. 46, pp. 993-999, 2001.

[17] Bryant, D., Payne, J., Firmin, D., and Longmore, D., "Measurement of Flow with NMR Imaging Using a Gradient Pulse and Phase Difference Technique," *Journal of Computer Assisted Tomography,* vol. 8, p. 588, 1984.

[18] Nayler, G., Firmin, D., and Longmore, D., "Blood Flow Imaging by Cine Magnetic Resonance," *Journal of Computer Assisted Tomography,* vol. 10, p. 715, 1986.

[19] Van Dijk, P., "Direct Cardiac Nmr Imaging of Heart Wall and Blood Flow Velocity," *Journal of Computer Assisted Tomography,* vol. 8, p. 429, 1984.

[20] McVeigh, E. R., "MRI of Myocardial Function: Motion Tracking Techniques," *Magnetic Resonance Imaging,* vol. 14, pp. 137-150, 1996.

[21] Zhu, Y. and Pelc, N. J., "Three-Dimensional Motion Tracking with Volumetric Phase Contrast MR Velocity Imaging," *Journal of Magnetic Resonance Imaging,* vol. 9, pp. 111-118, 1999.

[22] Constable, R. T., Rath, K. M., Sinusas, A. J., and Gore, J. C., "Development and Evaluation of Tracking Algorithms for Cardiac Wall Motion Analysis Using Phase Velocity MR Imaging," *Magnetic Resonance in Medicine,* vol. 32, pp. 33-42, 2005.

[23] Markl, M., Draney, M. T., Hope, M. D., Levin, J. M., Chan, F. P., Alley, M. T.*, et al.*, "Time-Resolved 3-Dimensional Velocity Mapping in the Thoracic Aorta: Visualization of 3-Directional Blood Flow Patterns in Healthy Volunteers and Patients," *Journal of Computer Assisted Tomography,* vol. 28, pp. 459-468, 2004.

[24] Fischer, S. E., McKinnon, G. C., Maier, S. E., and Boesiger, P., "Improved Myocardial Tagging Contrast," *Magnetic Resonance in Medicine,* vol. 30, pp. 191-200, 1993.

[25] Aletras, A. H., Balaban, R. S., and Wen, H., "High-Resolution Strain Analysis of the Human Heart with Fast-Dense," *Journal of Magnetic Resonance,* vol. 140, pp. 41-57, 1999.

[26] Epstein, F. H. and Gilson, W. D., "Displacement-Encoded Cardiac MRI Using Cosine and Sine Modulation to Eliminate (Cansel) Artifact-Generating Echoes," *Magnetic Resonance in Medicine,* vol. 52, pp. 774-781, 2004.

[27] Spottiswoode, B. S., Zhong, X., Hess, A. T., Kramer, C. M., Meintjes, E. M., Mayosi, B. M.*, et al.*, "Tracking Myocardial Motion from Cine DENSE Images Using Spatiotemporal Phase Unwrapping and Temporal Fitting," *Medical Imaging, IEEE Transactions on,* vol. 26, pp. 15-30, 2007.

[28] Haber, I., Metaxas, D. N., Geva, T., and Axel, L., "Three-Dimensional Systolic Kinematics of the Right Ventricle," *American Journal of Physiology-Heart and Circulatory Physiology,* vol. 289, pp. H1826-H1833, 2005.

[29] Young, A. A. and Axel, L., "Three-Dimensional Motion and Deformation of the Heart Wall: Estimation with Spatial Modulation of Magnetization-A Model-Based Approach," *Radiology,* vol. 185, pp. 241-247, 1992.

[30] Young, A. A., Fayad, Z. A., and Axel, L., "Right Ventricular Midwall Surface Motion and Deformation Using Magnetic Resonance Tagging," *American Journal of Physiology-Heart and Circulatory Physiology,* vol. 271, pp. H2677-H2688, 1996.

[31] Spottiswoode, B. S., Zhong, X., Lorenz, C. H., Mayosi, B. M., Meintjes, E. M., and Epstein, F. H., "3D Myocardial Tissue Tracking with Slice Followed Cine DENSE MRI," *Journal of Magnetic Resonance Imaging,* vol. 27, pp. 1019-1027, 2008.

[32] Glass, L., Hunter, P., McCulloch, A., and Science, I. f. N., *Theory of Heart: Biomechanics, Biophysics, and Nonlinear Dynamics of Cardiac Function*: Springer-Verlag, 1991.

[33] Auger, D. A., Zhong, X., Epstein, F. H., and Spottiswoode, B. S., "Mapping Right Ventricular Myocardial Mechanics Using 3d Cine DENSE Cardiovascular Magnetic Resonance," *Journal of Cardiovascular Magnetic Resonance,* vol. 14, p. 4, 2012.

[34] Cerqueira, M. D., Weissman, N. J., Dilsizian, V., Jacobs, A. K., Kaul, S., Laskey, W. K.*, et al.*, "Standardized Myocardial Segmentation and Nomenclature for Tomographic Imaging of the Heart " *Circulation,* vol. 105, pp. 539-542, 2002.

[35] Haber, I., Metaxas, D. N., and Axel, L., "Three-Dimensional Motion Reconstruction and Analysis of the Right Ventricle Using Tagged MRI," *Medical Image Analysis,* vol. 4, pp. 335-355, 2000.

[36] Fayad, Z. A., Ferrari, V. A., Kraitchman, D. L., Young, A. A., Palevsky, H. I., Bloomgarden, D. C.*, et al.*, "Right Ventricular Regional Function Using Mr Tagging: Normals Versus Chronic Pulmonary Hypertension," *Magnetic Resonance in Medicine,* vol. 39, pp. 116-123, 2005.

[37] Kayser, M., Hein, W., van der Geest Msc, R. J., van der Wall, M., Ernst, E., Duchateau Msc, C.*, et al.*, "Right Ventricular Function in Patients after Acute Myocardial Infarction Assessed with Phase Contrast MR Velocity Mapping Encoded in Three Directions," *Journal of Magnetic Resonance Imaging,* vol. 11, pp. 471-475, 2000.

[38] Wen, H., Marsolo, K. A., Bennett, E. E., Kutten, K. S., Lewis, R. P., Lipps, D. B.*, et al.*, "Adaptive Postprocessing Techniques for Myocardial Tissue Tracking with Displacement-Encoded MR Imaging," *Radiology,* vol. 246, pp. 229-240, 2008.

[39] Spottiswoode, B. S., Zhong, X., Patel, R. A., Helm, P. A., Mayosi, B. M., Kramer, C. M.*, et al.*, "Measuring LV-RV Interventricular Dyssynchrony Using Cine DENSE MRI," in *ISMRM 14th Scientific Meeting & Exhibition* Seattle, Washington, USA, 2006.

[40] Cho, J. and Benkeser, P. J., "Cardiac Segmentation by a Velocity-Aided Active Contour Model," *Computerized Medical Imaging and Graphics,* vol. 30, pp. 31-42, 2006.

[41] Kass, M., Witkin, A., and Terzopoulos, D., "Snakes: Active Contour Models," *International Journal of Computer Vision,* vol. 1, pp. 321-331, 1988.

[42] Histace, A., Matuszewski, B., and Zhang, Y., "Segmentation of Myocardial Boundaries in Tagged Cardiac MRI Using Active Contours: A Gradient-Based Approach Integrating Texture Analysis," *Journal of Biomedical Imaging,* vol. 2009, p. 4, 2009.

[43] Milles, J., van Susteren, A., Arts, T., Clarysse, P., Croisille, P., and Magnin, I. E., "Automatic 2D Segmentation of the Left Ventricle in Tagged Cardiac MRI Using Motion Information," in *Biomedical Imaging: Nano to Macro, 2004. IEEE International Symposium on*, 2004, pp. 153-156.

[44] Rueckert, D. and Burger, P., "Geometrically Deformable Templates for Shape-Based Segmentation and Tracking in Cardiac MR Images," in *Energy Minimization Methods in Computer Vision and Pattern Recognition*, 1997, pp. 83-98.

[45] Montillo, A., Metaxas, D., and Axel, L., "Automated Segmentation of the Left and Right Ventricles in 4D Cardiac Spamm Images," *Medical Image Computing and Computer-Assisted Intervention—MICCAI 2002,* pp. 620-633, 2002.

[46] Young, A. A., Cowan, B. R., Thrupp, S. F., Hedley, W. J., and Dell'Italia, L. J., "Left Ventricular Mass and Volume: Fast Calculation with Guide-Point Modeling on MR Images," *Radiology,* vol. 216, pp. 597-602, 2000.

[47] Spottiswoode, B. S., Zhong, X., Lorenz, C. H., Mayosi, B. M., Meintjes, E. M., and Epstein, F. H., "Motion-Guided Segmentation for Cine DENSE MRI," *Medical Image Analysis,* vol. 13, p. 105, 2009.

[48] Chen, T., Babb, J., Kellman, P., Axel, L., and Kim, D., "Semiautomated Segmentation of Myocardial Contours for Fast Strain Analysis in Cine Displacement-Encoded MRI," *Medical Imaging, IEEE Transactions on,* vol. 27, pp. 1084-1094, 2008.

[49] Pluempitiwiriyawej, C., Moura, J. M. F., Wu, Y. J. L., and Ho, C., "Stacs: New Active Contour Scheme for Cardiac MR Image Segmentation," *Medical Imaging, IEEE Transactions on,* vol. 24, pp. 593-603, 2005.

[50] Oldershaw, P., "Assessment of Right Ventricular Function and Its Role in Clinical Practice," *British Heart Journal,* vol. 68, p. 12, 1992.

[51] Haddad, F., Hunt, S. A., Rosenthal, D. N., and Murphy, D. J., "Right Ventricular Function in Cardiovascular Disease, Part I Anatomy, Physiology, Aging, and Functional Assessment of the Right Ventricle," *Circulation,* vol. 117, pp. 1436-1448, 2008.

[52] McKenna, W. J., Thiene, G., Nava, A., Fontaliran, F., Blomstrom-Lundqvist, C., Fontaine, G.*, et al.*, "Diagnosis of Arrhythmogenic Right Ventricular Dysplasia/Cardiomyopathy. ," *British Heart Journal,* vol. 71, p. 215, 1994.

[53] Alfakih, K., Plein, S., Thiele, H., Jones, T., Ridgway, J. P., and Sivananthan, M. U., "Normal Human Left and Right Ventricular Dimensions for MRI as Assessed by Turbo Gradient Echo and Steady-State Free Precession Imaging Sequences," *Journal of Magnetic Resonance Imaging,* vol. 17, pp. 323-329, 2003.

[54] Hamdan, A., Thouet, T., Sebastian, K., Paetsch, I., Gebker, R., Wellnhofer, E.*, et al.*, "Regional Right Ventricular Function and Timing of Contraction in Healthy Volunteers Evaluated by Strain-Encoded MRI," *Journal of Magnetic Resonance Imaging,* vol. 28, pp. 1379-1385, 2008.

[55] Tecelão, S. R. R., Zwanenburg, J. J. M., Kuijer, J., de Cock, C. C., Germans, T., van Rossum, A. C.*, et al.*, "Quantitative Comparison of 2D and 3D Circumferential Strain Using MRI Tagging in Normal and LBBB Hearts," *Magnetic Resonance in Medicine,* vol. 57, pp. 485-493, 2007.

[56] Helm, R. H., Leclercq, C., Faris, O. P., Ozturk, C., McVeigh, E., Lardo, A. C.*, et al.*, "Cardiac Dyssynchrony Analysis Using Circumferential Versus Longitudinal Strain," *Circulation,* vol. 111, pp. 2760-2767, 2005.

[57] Klein, S. S., Graham, T. P., and Lorenz, C. H., "Noninvasive Delineation of Normal Right Ventricular Contractile Motion with Magnetic Resonance Imaging Myocardial Tagging," *Annals of Biomedical Engineering,* vol. 26, pp. 756-763, 1998.

[58] Oppelt, A., "Fisp-A New Fast Mri Sequence," *Electromedica,* vol. 54, pp. 15-18, 1986.

[59] Scheffler, K. and Lehnhardt, S., "Principles and Applications of Balanced Ssfp Techniques," *European Radiology,* vol. 13, pp. 2409-2418, 2003.

[60] Axel, L., Montillo, A., and Kim, D., "Tagged Magnetic Resonance Imaging of the Heart: A Survey," *Medical Image Analysis,* vol. 9, pp. 376-393, 2005.

[61] Markl, M., Chan, F. P., Alley, M. T., Wedding, K. L., Draney, M. T., Elkins, C. J.*, et al.*, "Time Resolved Three Dimensional Phase Contrast MRI," *Journal of Magnetic Resonance Imaging,* vol. 17, pp. 499-506, 2003.

[62] Guttman, M. A., Prince, J. L., and McVeigh, E. R., "Tag and Contour Detection in Tagged MR Images of the Left Ventricle," *Medical Imaging, IEEE Transactions on,* vol. 13, pp. 74-88, 1994.

[63] Alattar, M. A., Osman, N. F., and Fahmy, A. S., "Segmentation of Left Ventricle in Cardiac MRI Images Using Adaptive Multi-Seeded Region Growing," in *Biomedical Engineering Conference (CIBEC), 5th Cairo International*, 2010, pp. 25-28.

[64] Montillo, A., Metaxas, D., and Axel, L., "Automated Model-Based Segmentation of the Left and Right Ventricles in Tagged Cardiac MRI," *Medical Image Computing and Computer-Assisted Intervention-MICCAI 2003,* pp. 507-515, 2003.

[65] Kainmuller, D., Unterhinninghofen, R., Ley, S., and Dillmann, R., "Level Set Segmentation of the Heart from 4D Phase Contrast MRI," in *Medical Imaging*, 2008, pp. 691414-691414-8.

[66] Huang, S., Liu, J., Lee, L. C., Venkatesh, S. K., Teo, L. L. S., Au, C.*, et al.*, "An Image-Based Comprehensive Approach for Automatic Segmentation of Left Ventricle from Cardiac Short Axis Cine Mr Images," *Journal of Digital Imaging,* vol. 24, pp. 598-608, 2011.

[67] Cocosco, C. A., Niessen, W. J., Netsch, T., Vonken, E., Lund, G., Stork, A.*, et al.*, "Automatic Image-Driven Segmentation of the Ventricles in Cardiac Cine MRI," *Journal of Magnetic Resonance Imaging,* vol. 28, pp. 366-374, 2008.

[68] Pednekar, A. S., Muthupillai, R., Cheong, B., and Flamm, S. D., "Automatic Computation of Left Ventricular Ejection Fraction from Spatiotemporal Information in Cine-Ssfp Cardiac MR Images," *Journal of Magnetic Resonance Imaging,* vol. 28, pp. 39-50, 2008.

[69] Herz, S. L., Ingrassia, C. M., Homma, S., Costa, K. D., and Holmes, J. W., "Parameterization of Left Ventricular Wall Motion for Detection of Regional Ischemia," *Annals of Biomedical Engineering,* vol. 33, pp. 912-9, Jul 2005.

[70] Hashima, A. R., Young, A. A., McCulloch, A. D., and Waldman, L. K., "Nonhomogeneous Analysis of Epicardial Strain Distributions During Acute Myocardial Ischemia in the Dog," *Journal of Biomechanics,* vol. 26, pp. 19-35, Jan 1993.

[71] Fisher, E. A., DuBrow, I. W., and Hastreiter, A. R., "Right Ventricular Volume in Congenital Heart Disease," *The American Journal of Cardiology,* vol. 36, pp. 67-75, 1975.

[72] Zou, K. H., Warfield, S. K., Bharatha, A., Tempany, C. M., Kaus, M. R., Haker, S. J.*, et al.*, "Statistical Validation of Image Segmentation Quality Based on a Spatial Overlap Index," *Academic Radiololgy,* vol. 11, pp. 178-89, Feb 2004.

[73] Kaus, M. R., Berg, J., Weese, J., Niessen, W., and Pekar, V., "Automated Segmentation of the Left Ventricle in Cardiac MRI," *Medical Image Analysis,* vol. 8, pp. 245-254, 2004.

[74] Li, J. and Denney Jr, T. S., "Left Ventricular Motion Reconstruction with a Prolate Spheroidal B-Spline Model," *Physics in Medicine and Biology,* vol. 51, p. 517, 2006.

[75] Liu, Y., Wen, H., Gorman, R. C., Pilla, J. J., Gorman, J. H., Buckberg, G., *et al.*, "Reconstruction of Myocardial Tissue Motion and Strain Fields from Displacement-Encoded MR Imaging," *American Journal of Physiology-Heart and Circulatory Physiology,* vol. 297, pp. H1151-H1162, 2009.

[76] Alfakih, K., Plein, S., Thiele, H., Jones, T., Ridgway, J. P., and Sivananthan, M. U., "Normal Human Left and Right Ventricular Dimensions for MRI as Assessed by Turbo Gradient Echo and Steady-State Free Precession Imaging Sequences," *Journal of Magnetic Resonance Imaging,* vol. 17, pp. 323-9, Mar 2003.

[77] Cain, P. A., Ahl, R., Hedstrom, E., Ugander, M., Allansdotter-Johnsson, A., Friberg, P.*, et al.*, "Age and Gender Specific Normal Values of Left Ventricular Mass, Volume and Function for Gradient Echo Magnetic Resonance Imaging: A Cross Sectional Study," *BMC Medical Imaging,* vol. 9, p. 2, 2009.

[78] Hudsmith, L. E., Petersen, S. E., Francis, J. M., Robson, M. D., and Neubauer, S., "Normal Human Left and Right Ventricular and Left Atrial Dimensions Using Steady State Free Precession Magnetic Resonance Imaging," *Journal of Cardiovascular Magnetic Resonance,* vol. 7, pp. 775-82, 2005.

[79] Maceira, A. M., Prasad, S. K., Khan, M., and Pennell, D. J., "Normalized Left Ventricular Systolic and Diastolic Function by Steady State Free Precession Cardiovascular Magnetic Resonance," *Journal of Cardiovascular Magnetic Resonance,* vol. 8, pp. 417-26, 2006.

[80] Abraham, T., Kass, D., Tonti, G., Tomassoni, G. F., Abraham, W. T., Bax, J. J.*, et al.*, "Imaging Cardiac Resynchronization Therapy," *Journal of the American College of Cardiology: Cardiovascular Imaging,* vol. 2, pp. 486-497, 2009.

[81] Yu, C. M., Bax, J., Monaghan, M., and Nihoyannopoulos, P., "Echocardiographic Evaluation of Cardiac Dyssynchrony for Predicting a Favourable Response to Cardiac Resynchronisation Therapy," *Heart,* vol. 90, pp. vi17-vi22, 2004.

[82] Bilchick, K. C., Dimaano, V., Wu, K. C., Helm, R. H., Weiss, R. G., Lima, J. A.*, et al.*, "Cardiac Magnetic Resonance Assessment of Dyssynchrony and Myocardial Scar Predicts Function Class Improvement Following Cardiac Resynchronization Therapy," *Journal of the American College of Cardiology: Cardiovascular Imaging,* vol. 1, pp. 561-568, 2008.

[83] Lardo, A. C., Abraham, T. P., and Kass, D. A., "Magnetic Resonance Imaging Assessment of Ventricular Dyssynchrony: Current and Emerging Concepts," *Journal of the American College of Cardiology,* vol. 46, pp. 2223-2228, 2005.

[84] Leclercq, C., Faris, O., Tunin, R., Johnson, J., Kato, R., Evans, F.*, et al.*, "Systolic Improvement and Mechanical Resynchronization Does Not Require Electrical Synchrony in the Dilated Failing Heart with Left Bundle-Branch Block," *Circulation,* vol. 106, pp. 1760-1763, 2002.

[85] Zwanenburg, J. J. M., Götte, M. J. W., Marcus, J. T., Kuijer, J. P. A., Knaapen, P., Heethaar, R. M.*, et al.*, "Propagation of Onset and Peaktime of Myocardial Shortening in Time of Myocardial Shortening in Ischemic Versus Nonischemic Cardiomyopathy: Assessment by Magnetic Resonance Imaging Myocardial Tagging," *Journal of the American College of Cardiology,* vol. 46, pp. 2215-2222, 2005.

[86] Leyva, F., "Cardiac Resynchronization Therapy Guided by Cardiovascular Magnetic Resonance," *Journal of Cardiovascular Magnetic Resonance,* vol. 12, p. 64, 2010.

[87] Jamal, F., Bergerot, C., Argaud, L., Loufouat, J., and Ovize, M., "Longitudinal Strain Quantitates Regional Right Ventricular Contractile Function," *American Journal of Physiology-Heart and Circulatory Physiology,* vol. 285, pp. H2842-H2847, 2003.

[88] Fischer, S. E., Stuber, M., Scheidegger, M. B., and Boesiger, P., "Limitations of Stimulated Echo Acquisition Mode (Steam) Techniques in Cardiac Applications," *Magnetic Resonance in Medicine,* vol. 34, pp. 80-91, 1995.

[89] Ballester-Rodés, M., Flotats, A., Torrent-Guasp, F., Carrió-Gasset, I., Ballester-Alomar, M., Carreras, F.*, et al.*, "The Sequence of Regional Ventricular Motion," *European Journal of Cardio-Thoracic Surgery,* vol. 29, pp. S139-S144, 2006.

[90] Buckberg, G., Hoffman, J. I. E., Mahajan, A., Saleh, S., and Coghlan, C., "Cardiac Mechanics Revisited," *Circulation,* vol. 118, pp. 2571-2587, 2008.

[91] Zwanenburg, J., Götte, M., Kuijer, J., Heethaar, R., Van Rossum, A., and Marcus, J., "Timing of Cardiac Contraction in Humans Mapped by High-Temporal-Resolution MRI Tagging: Early Onset and Late Peak of Shortening in Lateral Wall," *American Journal of Physiology-Heart and Circulatory Physiology,* vol. 286, pp. H1872-H1880, 2004.

[92] Auger, D., Spottiswoode, B., Budge, L., Zhong, X., Epstein, F., and Bilchick, K., "The Effect of Left Bundle Branch Block and Heart Failure on Circumferential Right Ventricular Dyssynchrony and Function: Assessment with MR Cine DENSE," presented at the International Society for Magnetic Resonance in Medicine 20th Annual Meeting, Melbourne, Australia, 2012.